Experiments for
Gas-Liquid Flow in a Vertical Annulus

P.J. Muis

Experiments for
Gas-Liquid Flow in a Vertical Annulus

by

Pjotr Jacob Muis

in fulfillment of the requirements for the degree of

Master of Science
in Mechanical Engineering

at the Delft University of Technology, to be defended publicly on Friday October 25, 2019 at 10:30.

Student number:	4233654	
Supervisors:	Prof. dr. ir. R. A. W. M. Henkes,	TU Delft
	Ir. A. J. Greidanus,	TU Delft
Thesis Committee:	Prof. dr. ir. R. A. W. M. Henkes,	TU Delft
	Ir. A. J. Greidanus,	TU Delft
	Dr. ir. B. W. van Oudheusden,	TU Delft
	Dr. ir. M. J. Tummers,	TU Delft
	Dr. ir. J. M. C. van 't Westende,	TNO/TU Delft
Report number:	2994	

TUDelft

Abstract

Shifting from coal and oil towards sustainable energy sources is currently an urgent and global challenge. Compared to coal and oil, natural gas is a cleaner fossil fuel and may serve as a transition fuel. To meet future demands for gas there is a desire to optimize the production from existing reservoirs with their production facilities. In case of wet natural gas wells this gas production can be hampered by the presence of liquids, namely water and condensate, thus creating a multiphase flow in the production tubing. The maximum gas well capacity is limited by the ever reducing upward gas flow velocity due to the subsurface reservoir pressure that is reducing over time. The reduced gas velocity results in the inability to transport the liquid upward from the downhole location to the surface. The accumulated liquids will then block the well bore (so-called liquification), making further gas production impossible. One solution it to decrease the cross sectional flow area by inserting an inner pipe in the existing tubing, thus creating an annulus. This results in a higher gas velocity. The multiphase flow characteristics in the annulus tubing are not yet fully understood, such as the pressure drop, the liquid hold-up and the different flow regimes. Therefore in the present study lab experiments were carried out to further investigate those characteristics to enable optimisation of predictive flow modeling. The main focus is on the behaviour of the liquid film along both pipe walls.

In this study a 12 m mid-scale vertical annulus with a 124 mm diameter outer pipe and a 100 mm diameter inner pipe was designed and constructed. The experiments were conducted at atmospheric conditions using an air-water mixture as the working fluids. Multiple combinations of gas and liquid throughputs were studied. The liquid at the inlet could either be injected on the inner pipe, the outer pipe or equally divided on both pipes. The position of the inner pipe with respect to the outer pipe was adjustable to create different eccentricities. To measure the local film heights flush mounted conductance sensors were designed, built and installed in the half circumference of both pipes. The efficacy of the sensors was thoroughly studied and the sensors were subjected to multiple test cases.

The concentric annulus experiments showed that the pressure drop does not depend on the method of liquid injection. However, the liquid hold-up fraction at lower liquid throughputs was observed to be lower for the single wall liquid injection as compared to injection on both pipes. The redistribution of the liquid film for the single liquid injection depends on the liquid throughput. Larger liquid throughputs gave thicker liquid films containing a wavier gas-liquid interface from which droplets are atomized and subsequently migrated to the other pipe wall. Furthermore, it was found that the critical superficial gas velocity at which liquid loading occurs is 14 m/s, which is neither dependent on the method of liquid injection nor on the liquid throughput. The designed sensors were able to provide a good indication of the film heights.

Single phase experiments, using air as the working fluid, showed that the pressure drop is reduced by 30% in the fully eccentric case in comparison to the concentric case. The eccentric annulus configuration with air-water flow showed that the liquid films along both pipe walls may merge. This so-called liquid bridging mainly occurs at higher eccentricities and causes flow reversal in the narrow gap. This results in a much higher liquid hold-up and pressure drop. Eccentricity induces redistribution of the liquid film from the inner pipe to the outer pipe at higher superficial gas velocities. It was found that eccentricity promotes an unequal film height along the circumference of each pipe: the film height decreases when going from the narrow gap towards the wide gap.

Acknowledgement

during rainy days.

Furthermore, I would like to thank my parents and my brothers, Emiel, Mathijs and Jesse, for their continuous loving and unconditional support. Mum and Martin, thank you for always being there for me and dad, thank you for your countless advises, even for those I never solicited for throughout my whole life and education.

Last but not least, I thank my amazing girlfriend Dionne. Dionne you supported me during this thesis in every possible manner. You made sure that I would not lose myself on the way. I cannot wait to spend the upcoming adventures together.

'Panta Rhei', today I know in which direction... Thank you all!

Pjotr J. Muis
Delft, October 2019

Contents

List of Symbols

Physical Constants

g	Gravitational acceleration - 9.81	$[\mathrm{m\,s^{-2}}]$

Greek Symbols

α	Hold-up	$[\text{-}]$
γ	Conductivity	$[\mathrm{S\,m^{-1}}]$
δ	Film height	$[\mathrm{m}]$
δ_w	Disturbance wave thickness	$[\mathrm{m}]$
λ	Taylor length scale	$[\mathrm{m}]$
μ	Dynamic viscosity	$[\mathrm{Pa\,s}]$
ρ	Density	$[\mathrm{kg\,m^{-3}}]$
σ	Surface tension	$[\mathrm{N\,m^{-1}}]$
τ	Shear stress	$[\mathrm{Pa}]$
θ	Tangential position	$[°]$

Roman Symbols

A	Area	$[\mathrm{m^2}]$
C	Capacitance	$[\mathrm{F}]$
D	Diameter	$[\mathrm{m}]$
$\tilde{D}$	Characteristic length scale	$[\mathrm{m}]$
D_p	Droplet diameter	$[\mathrm{m}]$
d_p	Distance between two probes	$[\mathrm{m}]$
d_w	Width or diameter of a probe	$[\mathrm{m}]$
e	Eccentricity parameter	$[\text{-}]$
Fr	Densimetric Froude number	$[\text{-}]$
f	Frequency	$[\mathrm{Hz}]$
f	Friction factor	$[\text{-}]$
f_{in}	Ratio of liquid injected on the inner pipe	$[\mathrm{m}]$
G	Conductance between the probes	$[\mathrm{S}]$

G^*	Conductance factor	[-]
H	Amplification factor	[-]
K	Diameter distribution as D_i/D_o	[-]
k_s	Sand-grain roughness	[m]
Ku	Kutateladze number	[-]
l	Length of the rectangular probe	[m]
$\mathscr{P}$	Perimeter	[m]
P	Pressure	[Pa]
R	Resistance	[Ω]
r	Radial position	[m]
Re_f	Reynolds number of the fluid film	[-]
S_{xx}	Energy spectrum	[$\mathrm{m^2\,Hz^{-1}}$]
T	Temperature	[K]
T	Film thickness ratio as δ_i/δ_o	[-]
u	Velocity	[$\mathrm{m\,s^{-1}}$]
u_{sg}	Superficial gas velocity	[$\mathrm{m\,s^{-1}}$]
u_{sl}	Superficial liquid velocity	[$\mathrm{m\,s^{-1}}$]
$\dot{V}$	Volumetric throughput	[$\mathrm{m^3\,s^{-1}}$]
V	Voltage	[V]
V_{amp}	Amplified signal	[V]
V_{out}	Analog output signal	[V]
V_{pp}	Peak-to-Peak signal	[V]
We	Weber number	[-]
$\overline{W_i}$	Planar view of the entrained droplets towards the inner pipe	[-]
z	Axial position	[m]

Subscripts

c	Cross-section or cut-off
cr	Critical
del	Development
g	Gas

gc   Gas core

gl   Global

h   Hydraulic

i   Inner pipe or Interface

l   Liquid

lo   Local

n   Inner or outer pipe

o   Outer pipe

r   Radial

t   Turbulence

w   Wall or wave

z   Electrical component in feedback loop

Abbreviations

AOF   Absolute Open Flow

CPDF   Cumulative Probability Density Function

GWP   Global Warming-Potential

IPR   Inflow Performance Relation

LNG   Liquified Natural Gas

PDF   Probability Density Function

PMMA   Polymethyl Methacrylate

RP   Reservoir Pressure

SONN   Self Organizing Neutral Network

TPC   Tubing Performance Curve

List of Figures

List of Tables

1

Introduction

The energy transition is one of the biggest challenges that human kind is facing. Shifting from the polluting fossil fuels, such as coal and oil, to green energy sources, such as wind and solar, is the main focus. However, the availability of these new energy sources is often dependent on local weather conditions or they are still in a preliminary development stage.

Therefore, in order to be able to satisfy the increasing energy needs and to ensure that the energy transition runs smoothly, a concession needs to be made. Natural gas can play a large role in this matter. This hydrocarbon gas mixture, mainly consisting of methane (larger than 85 Vol.% [41]), is much lighter than the heavy fossil fuels. Therefore, natural gas emits for example up to 45% less CO_2 and produces a fifth of the NO_x amounts compared to coal [31]. Furthermore, the flexibility of this fuel type is a great advantage. When there is a peak demand of energy, gas generators and power plants can scale up their energy production quickly. This makes natural gas an attractive stand-in when the sun does not shine or when the wind does not blow. The gas can be compressed to Liquified Natural Gas (LNG), which tremendously simplifies the transportation.
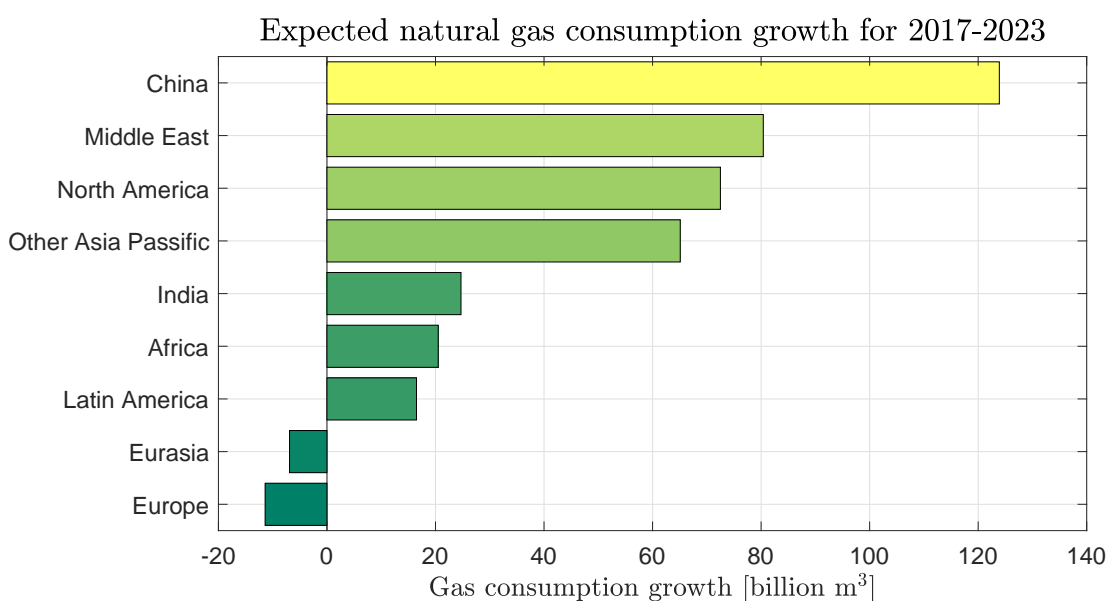
Figure 1.1: Expected natural gas consumption for the period of 2017 until 2023 [1].

1

Power generation is not the only reason why natural gas is gaining more popularity. Natural gas also serves as an important feedstock for chemicals in the in the industry. Hydrogen production, is one of these examples, which can be used for gray hydrogen power generation [41]. For these reasons the demand for natural gas will grow worldwide. Figure 1.1 shows the expected growth in natural gas consumption of the continents and the largest energy consuming countries, India and China. The average global annual growth is expected to be 1.6%. As can be seen, China will be expected to increase their consumption to 124 billion cubic meters per annum, resulting in a growth by 60% between 2017 until 2023. This is mainly due to the focus on decreasing the air pollution by switching from coal to gas [1]. Therefore, the production of natural gas needs to be increased in order to meet the demands. However, this is accompanied with some challenges. One of the biggest environmental challenges is to reduce the gas leakages during production to an absolute minimum, since methane is a greenhouse gas with a Global Warming Potential (GWP) of 25. Other complications can be the contamination of ground water, disposal of drilling fluids and local earthquakes [41].

Usually, a gas reservoir does not completely consist of dry natural gas, but also contains condensate and water. This gives a multiphase flow in the production tubing that transports the gas from the reservoir to the surface. These liquids can form a film layer along the tubing walls, flowing in co-current direction with the gas. This film layer has a negative influence on the possible production life time of a gas well. This is because the gas may have insufficient pressure (or momentum) to lift the liquids to the surface. The challenge is to develop a technical solution to increase the lifespan of the gas well. However, to do so, it is a necessity to dive into the characteristics of a 'wet' natural gas well.

1.1. The wet natural gas well
A wet natural gas well consists of three important parts, see figure 1.2 on the left. First of all, the gas reservoir is located several kilometers below the surface. In the reservoir the gas is trapped in a network of pores, with on top an impermeable layer of rock, preventing the gas from flowing to the surface [41]. The structure and density of the pores have a great influence on the flow characteristics through the tubing when a reservoir is drilled. The second part is the well bore, which is the connection between the reservoir and the surface. The vertical tubing, which is the third part, is in fact the production pipe inside the well bore. Through the tubing the gas and side products are carried to the surface.

In the initial state where there is no gas production, the pressure at the bottom hole location of the well bore is equal to the reservoir pressure (RP). Now the well head choke is fully closed. In the other extreme case, the pressure difference between the surface and the tubing head location of the well bore becomes zero. Here the well head choke is fully open. There now is a maximum pressure difference between the reservoir and the bottom hole location of the well bore. This is called Absolute Open Flow (AOF) and the gas flow is at its maximum [29]. These two nodes (no inflow and maximum inflow) are part of the Inflow Performance Relation (IPR), see figure 1.2. The IPR is unique for every gas well. The flow in the tubing creates a back pressure at the bottom hole location of the well bore. This pressure is the sum of the pressure at the tubing head location and the pressure drop over the length of the production tubing. The pressure drop is the sum of the hydrostatic pressure drop inside the tubing and the frictional pressure losses. The hydrostatic pressure is mainly determined by the liquid fraction in the cross sectional area of the tubing, which is called the liquid hold-up. The Tubing Performance Curve (TPC) describes the relation between the back pressure at the bottom hole location and the gas flow rate in the tubing, see figure 1.2.

(a) Gas reservoir

(b) Well inflow and tubing characteristics
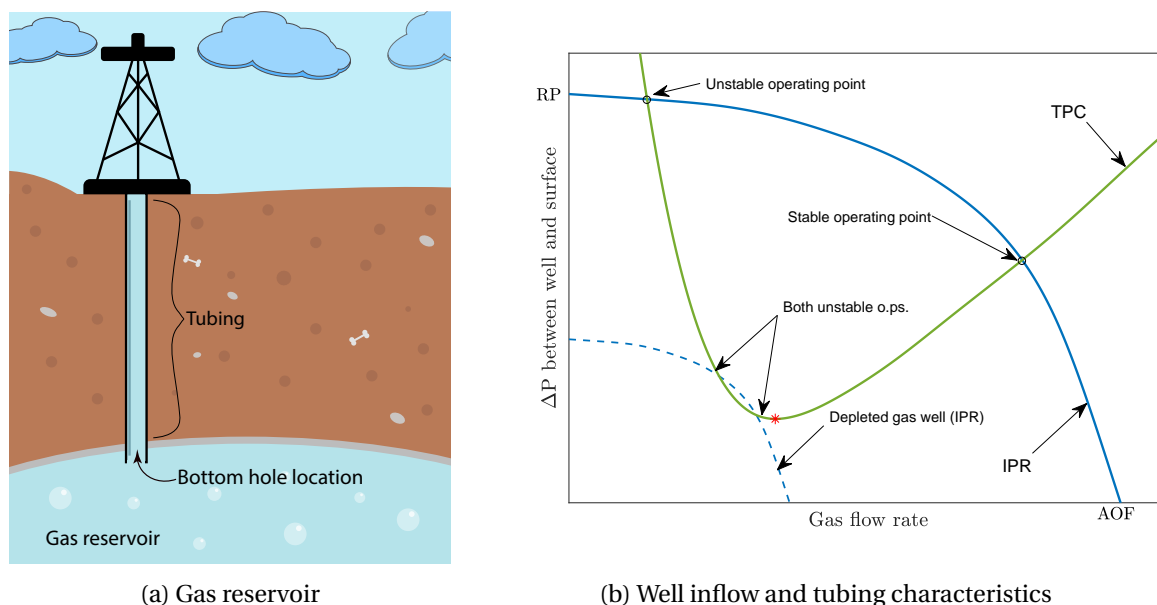
Figure 1.2: Left, the lay-out of an operating gas well. Right, the Inflow Performance Relation (IPR) and the Tubing Performance Curve (TPC), both in stable and unstable operation.

For high gas rates, the liquid hold-up is relatively small. In this case, the frictional pressure drop is dominant (in comparison to the gravitational pressure drop. When the gas rate is decreasing, the friction between the liquid and gas also decreases and as a result of this, the liquid hold-up will increase. In other words, due to gravity the gas has more difficulties to transport the liquid upward towards the surface. In this case the hydrostatic pressure drop becomes dominant. In between there is a stability point where the hydrostatic pressure drop and the frictional pressure drop are about equal. This point is marked in figure 1.2 with a red asterisk (*).

As can be seen in figure 1.2, that the TPC intersects the IPR curve at two points. The intersection at the higher gas flow, right from the stability point, is self stabilizing. This means that when the gas flow increases at the bottom hole location of the well bore, the frictional pressure drop in the tubing increases, creating a higher back pressure and bringing back the operating point to its origin. The intersection at the lower gas rate, left from the stability point, is not self stabilizing. When the gas flow at the bottom hole location decreases, the hydrostatic pressure drop increases in the tubing, causing a higher back pressure in the gas well. Eventually, this back pressure can be so high that no gas flow is possible. Therefore, stable operation is only possible at the right side of the stability point.

At the start of the production, the reservoir pressure is high enough to guarantee a stable operating point. However, as time evolves, the well depletes and the reservoir pressure will decrease. The characteristics of the IPR change. Eventually, a point is reached where two stable operating points are not possible anymore, see the blue dashed line in figure 1.2. At this point liquid loading starts to take place. Liquid loading is the point where the gas well is no longer able to transport the liquid towards the surface. Liquid loading starts with a reduced production due to the accumulation of liquids, but has as ultimate result that the tubing fills up with liquid and is not operable anymore.

1.2. Problem statement

As mentioned earlier, the global demand for natural gas increases. For this reason it is important that the life time of every gas well can be extended to its maximum. Liquid loading has a major limiting effect on this life time due to the hydrostatic pressure drop of the accumulated liquid in the

well bore. It is known that this process is closely related to the stability point on the TPC. In order to postpone liquid loading, several techniques have been proposed in order to shift the TPC and to deliquify the gas well. A few of these techniques are listed below:

- *Gas lift*. By injecting small air bubbles into the well bore, the cumulative hydrostatic pressure drop is decreased.

- *Surfactants*. Adding surfactants to the flow causes the liquids to foam. The foam has a lower density than the liquid, which reduces the hydrostatic pressure drop.

- *Velocity string*. The cross sectional area of the production tubing is reduced by inserting an inner pipe. The created annulus induces a higher gas velocity, which increases the friction between the gas phase and the liquid phase and therefore prevents liquid loading.

This report will focus on the use of a velocity string. The change in location of the stability points on the TPC, due to the creation of an annulus, is not yet known. Furthermore, a little is known about the flow characteristics in an annulus and the impact of the eccentricity of the inner pipe.

This study tries to answer these questions. Air-water experiments are conducted in a mid-scale annulus set-up. With the retrieved data, correlations can be formulated for the flow stability, pressure drop and liquid hold-up. Eventually, these correlations can be implemented in models which will be able to predict the real technical and economical gains in the industry.

1.3. Report outline
This report starts with Chapter 2, which contains a literature review on the important topics concerning upward two-phase flow. In that review different flow regimes are discussed as preparation of the 1-D modelling of the flow in a pipe and in an annulus. The prediction of liquid loading is discussed into further detail together with disturbance waves, which is another important multiphase flow phenomenon. Furthermore, a review is given on the studies conducted on eccentricity in the annulus configuration. In the last section the project objectives together with the research questions are being formulated.

In Chapter 3 the experimental set-up is introduced. Because the set-up had to be designed and built, the development of the most important parts is briefly described. Then the flow loop is discussed with respect to the applied instrumentation.

Chapter 4 describes the development of the film sensor to measure the liquid hold-up and liquid film distribution in an annulus. First, an overview is given on film measurement techniques and the use of conductance probes. Then the electrical circuit and signal analysis are being discussed. The chapter closes with the final design and implementation for the annulus set-up. The development stages in order to find the proper sensor design are given in Appendix A.

In Chapter 5 and 6 the results of respectively a concentric and eccentric annulus are presented and discussed. The main conclusion of this Master Thesis is given in the last chapter, Chapter 7. The chapter ends with some recommendations for further research.

2

Literature review

Before an experimental study can be conducted on the gas-liquid behaviour in a vertical annulus, it is important to know which parameters impact the flow. This chapter will give a review on the most relevant topics for multiphase flow in an annulus. Also the most relevant studies that have been performed will be mentioned. In the first section the distinction is made between the different flow regimes when considering a gas-liquid flow. The second section will cover the 1D-modeling of the flow. In that section the flow problem is simplified in order to predict one of the most important variables: the pressure drop along the tubing. Liquid loading and prediction models will be discussed in more depth in the third section. The friction between the gas phase and the liquid phase is to a large extent determined by large liquid waves, which are called disturbance waves. The characteristics of these waves will be covered in the fourth section. The last subject will be the effect of the eccentricity of the inner pipe with respect to the outer pipe on the annulus flow. After the review of these subjects, a project objective will be formulated for the experimental study.

2.1. Gas-liquid flow regimes in an annulus

The gas and liquid in a two-phase pipe flow can organize themselves in different flow patterns. Every flow pattern defines a flow regime. Multiple factors can influence the arrangement and thus the regime of the gas and liquid flow: pressure, temperature, tubing diameter and wall roughness, and also the inclination of the tubing, *i.e.* horizontally or vertically (upward or downward). Note that the pressure and temperature determine the split between the liquid and gas, and the thermodynamic properties (density, viscosity, interfacial tension). The most important factor, which impacts the arrangement of the liquid and gas, is the size of the liquid and gas flow rates. These quantities can be expressed as the superficial gas and liquid velocities given by

$$u_{sl} = \frac{\dot{V}_l}{A_c} \qquad (2.1a) \qquad\qquad u_{sg} = \frac{\dot{V}_g}{A_c} \qquad (2.1b)$$

where $\dot{V}_l$ and $\dot{V}_g$ are the volumetric throughput of the liquid and gas, respectively, and A_c is the cross-sectional area of the pipe or annulus. The superficial velocity represents the average velocity that would be found when the total cross section is occupied by a single fluid. Usually, studies on flow patterns are carried out by varying the combination of the two superficial velocities.

It is important to make a distinction between the different flow regimes, because all transport phenomena are intrinsically related to the local flow regime. In history, flow regimes were often classified by means of visual interpretation.

5

Therefore, a subjective factor is present in such a classification which led to different nomenclature and definitions for the flow regimes. Later, the regimes became more standardized and the number of different classifications was reduced. Caetano et al. [10] formulated comprehensive prerequisites to define the flow regimes in vertical annuli. These definitions are listed below in the order of increased superficial gas velocity and correspond to figure 2.1:

- *Bubble* and *Dispersed bubble flow*. In these flow regimes, the liquid fraction in the total volumetric flow, is high as compared to the gas fraction. This results in small spherical gas bubbles that are dispersed in a continuous liquid phase. When the liquid fraction is decreased, bubbles start to mitigate into cap bubbles with a higher upward velocity.

- *Slug flow*. This flow regime is characterized by large Taylor bubbles occupying nearly the complete cross sectional area altered with liquid slugs. A small liquid bridge is formed which prevents the Taylor bubble to mitigate. Through this bridge the liquid is flowing downward.

- *Churn flow*. Churn flow is a chaotic form of slug flow. The higher gas flow constantly destroys the large Taylor bubble. When this happens, the liquid slugs above the bubble flow downward and the liquid accumulates. Successively, the gas pushes the accumulated liquid slug upward again. This process repeats itself continuously.

- *Annular flow*. The gas flows as a continuous phase in the core between the outer pipe and the inner pipe. A thin upward flowing wavy liquid film is present on the pipe walls. In the gas core a fraction of the liquid is entrained and is moving along with the gas in the form of tiny spherical droplets.
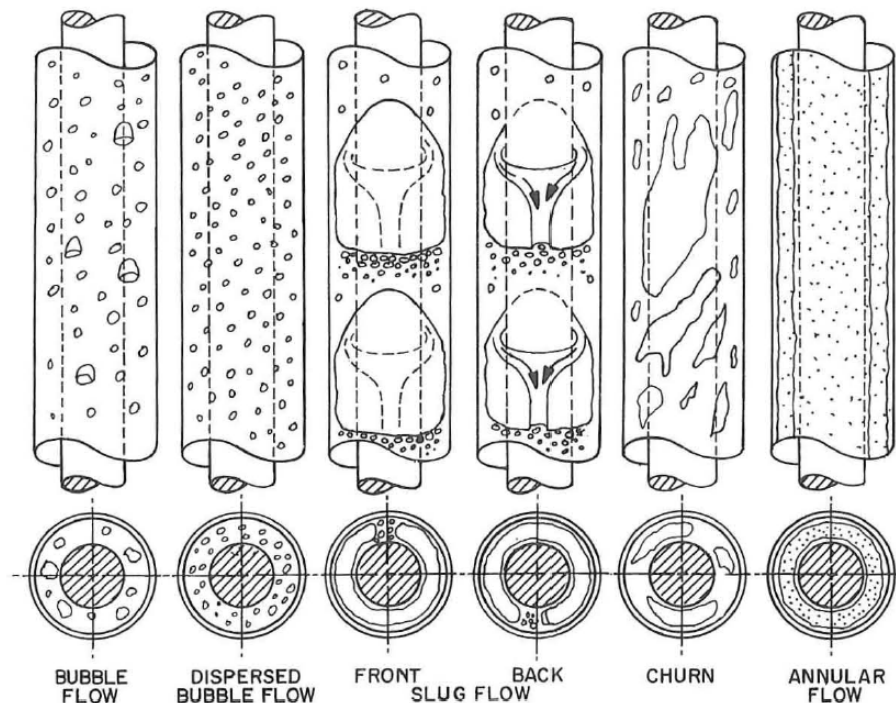
Figure 2.1: Different flow regimes in a concentric annulus. Image taken from Caetano et al. [10].

Studies on flow patterns in annuli

Over the past decades, numerous studies on flow regimes in two-phase pipe flows have been performed and these studies are summarized in a review paper by Cheng et al. [12]. In that paper, it becomes clear that defining a flow regime is not straightforward. As said, one method is to base the classification on visual observations. This method is usually accompanied with subjectivity and leads to inconsistencies in flow pattern data from different researchers using the same test conditions. Cheng et al. [12] concluded that most of the researchers still use this method to find the flow patterns in pipes.

With respect to annuli, significantly fewer studies have been performed on the flow regimes. Table 2.1 summarizes the most important studies on flow regimes which are useful for the study performed in this thesis. All these experiments were conducted with atmospheric conditions at the outlet. Also listed in this table are the different geometric and flow conditions used to conduct the studies. In this table, the dimensionless length is determined by dividing the length z by the hydraulic diameter D_h. The hydraulic diameter is given by

$$D_h = D_o - D_i \tag{2.2}$$

where D_o is the inner diameter of the outer pipe and D_i is the outer diameter of the inner pipe. The hydraulic diameter represents the same diameter as when a single pipe is used, but also accounts for the extra friction caused by the presence of the annulus configuration. It is an important parameter when the development of the flow is investigated.

Caetano et al. [10] conducted a visualization study for air-water flow in a 16 meter concentric and fully eccentric ($e = 1$) annulus for a wide range of superficial gas and liquid velocities. Caetano et al. formulated the conditions corresponding to figure 2.1, which the flow had to fulfill in order to classify the flow regime. These conditions are considered to be sufficiently comprehensive. They investigated the effect of pressure and used besides water, also kerosene as liquid.

To reduce the subjectivity in the flow regime determination, other techniques have been used in order to define a flow regime. A widely used technique, besides visual determination, is making use of conductance probes. The signal from these probes corresponds to the void fraction in the flow. Based on the probability density function (PDF) of the signal, a distinction can be made between the flow regimes.

Kelessidis and Dukler [26] were the first to use this technique in a vertical annulus. The authors defined criteria for the PDF to classify a flow regime, based on the signal of two conductivity probes. In their investigation 85 flow conditions were studied, covering all four flow regimes. Das et al. [16] carried out a similar study, investigating 150 flow conditions in three different geometrical configurations. As can be seen in table 2.1, Das et al. [16] used a small interval for the superficial gas velocity, studying the bubble, slug and churn flow regimes. By varying the configuration of the annulus they tried to establish a relation between the gap size of the annulus and the dimensions of the Taylor bubble.

A more recent study was performed by Julia et al. [25]. Their study also made use of conductance probes, but classified the flow regimes in a unique manner. While the above mentioned studies have based the classification on self made rules, Julia et al. [25] used a self-organizing neutral network (SONN).

Table 2.1: Performed flow regime studies on vertical annuli.

Work	Fluids	Configuration	Diameters [mm]		Length [-]	Velocity range [m/s]		Identification	
			D_o	D_i	z/D_h	u_{sg}	u_{sl}	Technique	Classifier
Kelessidis and Dukler [26]	Air-Water	Concentric Eccentric $e = 0.5$	76.2	50.8	~270	0.02 - 22	0.01 - 2	Conductivity	Author's rules
Caetano et al. [10]	Air-Water Air-Kerosene	Concentric Eccentric $e = 1$	76.2	42.2	~470	0.01 - 22	0.002 - 3	Visual	Author's rules
Das et al. [16]	Air-Water	Concentric	50.8 38.1 25.4	25.4 12.7 12.7	N/A	0.04 - 9.0	0.08 - 2.8	Conductivity	Author's rules
Julia et al. [25]	Air-Water	Concentric	38.1	19.1	~230	0.01 - 30	0.2 - 3.5	Conductivity	SONN

This network is comparable with a machine learning approach in order to make the classification more objective. SONN bases the classification on the cumulative probability density function (CPDF) of the conductivity signal. They investigated 76 flow conditions at three axial locations along the pipe. Using the results at the three locations they investigated the axial development of the change in flow regime.

Flow pattern map

Each classification corresponding to a combination of superficial gas and liquid velocities can be summarized in a flow pattern map. In figure 2.2 we have collected the results from four different experimental studies for the flow regime for a water-air mixture in an annulus at atmospheric pressure. It can be seen that the overall results for the different studies are in good agreement. However, no hard transition lines can be drawn due to the different classification definitions. For example, in the slug-churn transition (S-C), Das et al. [16] have some results classified as slug, which are classified by the other studies considers the flow already to be churn.

In figure 2.2 the transition between churn flow and annular flow can be considered as a straight line up to a certain superficial liquid velocity where the line starts to deviate. However, the corresponding superficial gas velocity is different, *e.g.* Caetano et al. [10] consider the transition to be at a superficial gas velocity of approximately 9 m/s, Julia et al. [25] at 11 m/s and Kelessidis and Dukler [26] at 15 m/s. This transition line is important for the moment of the onset of liquid loading and therefore for the topic of this thesis.

Flow regimes in gas well tubing

In case of a gas well tubing usually all these flow regimes are more or less present during the lifetime of a gas well [29]. However, the most dominant regime in the tubing is annular flow due to the high gas volume fraction compared to the condensate or water side products. The gas-liquid volume rate fractions can be different for each gas well, but can assumed to be in the order of 10 to 100 ppm [34]. The annular flow regime corresponds to the stable part of the TPC, see figure 1.2. The unstable part of the TPC, which is dominated by the hydrostatic pressure drop, is affiliated with the churn flow regime. Since the point of interest is the lifetime increase of a gas well, the transition of the stable annular flow to the unstable chaotic churn flow must be studied in more detail.

The red dotted rectangle in figure 2.1 highlights the area of interest for the experiments in the present project. Although these superficial liquid velocities are higher than the superficial liquid velocities found in the industrial applications, the annular-churn transition can still be investigated. This is due to the weak dependence of the superficial liquid velocity on the flow regime transition.
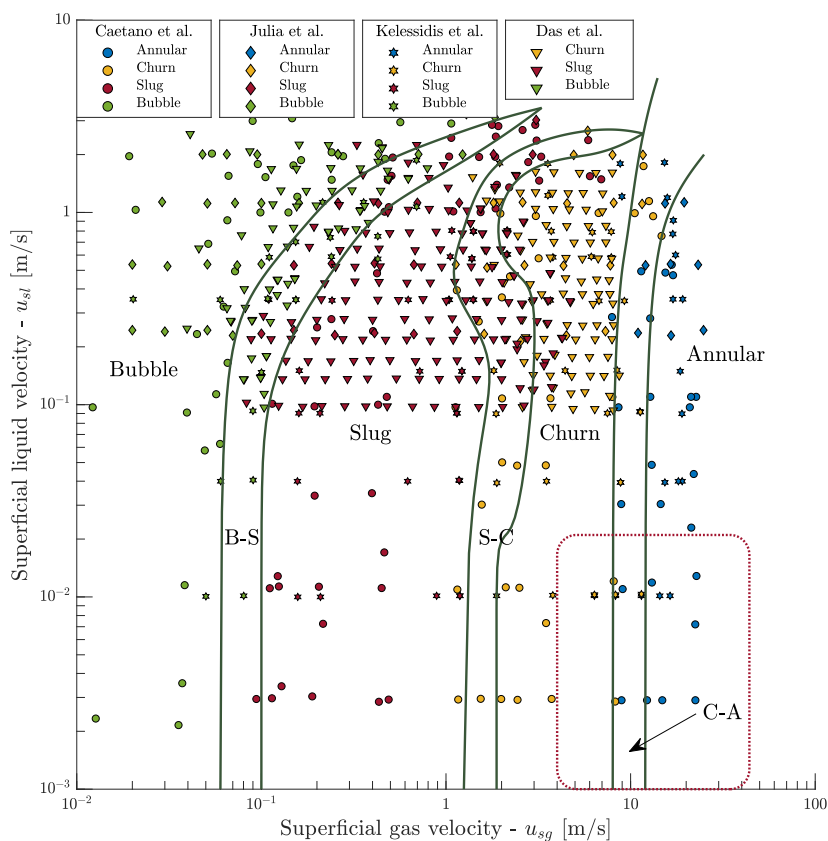
Figure 2.2: Flow pattern map for an air-water flow in a vertical concentric annulus at atmospheric pressure. The red dotted rectangle is the area of interest for the experimental study in this thesis.

A key parameter in the transition from annular flow to churn flow and the start of liquid loading is the point of onset of flow reversal. This is where the gas is firstly no longer able to drag the liquid upward, and instead the liquid flows partly downward. In section 2.3, the different approaches for the determination of flow reversal and the onset of liquid loading are discussed. However, to be able to fully understand the described transition models, the upward annular flow in an annulus will be described by a 1D model.

2.2. 1D analytical model for annular flow in an annulus

In the Introduction it is described that there still is a need for a model which can predict the pressure losses in an annulus. In this section a start will be made with the modeling of annular two-phase flow in an annulus, as well as with the discussion of closure problems in order to make this model work. To enable this, the annular flow problem in an annulus can be simplified into a one dimensional problem, which treats the gas and liquid flows separately. Over the past this separated flow approach has been frequently used. Hewitt and Hall-Taylor [20] and Fu and Klausner [19] used the approach for a single pipe flow. Van Nimwegen el. [47] used this approach to model the pressure drop in a single vertical pipe operating with surfactants (foam). Kurian [28], Yin et al. [51] and Kelessidis and Dukler [26] modeled the annular flow in an annulus. Su et al. [42] also used this approach for an annulus and included heat transfer.

Figure 2.3 is a schematic representation of the annular flow in a concentric annulus. Two film layers can be seen on the inner and outer walls. All the parameters concerning the film on the inner and outer pipe have the subscript i or o, respectively. In this analysis it is assumed that the different film layers have a constant thickness, the annulus is perfectly vertical, the flow is adiabatic and the film and gas flow are not accelerating (i.e. fully developed flow).
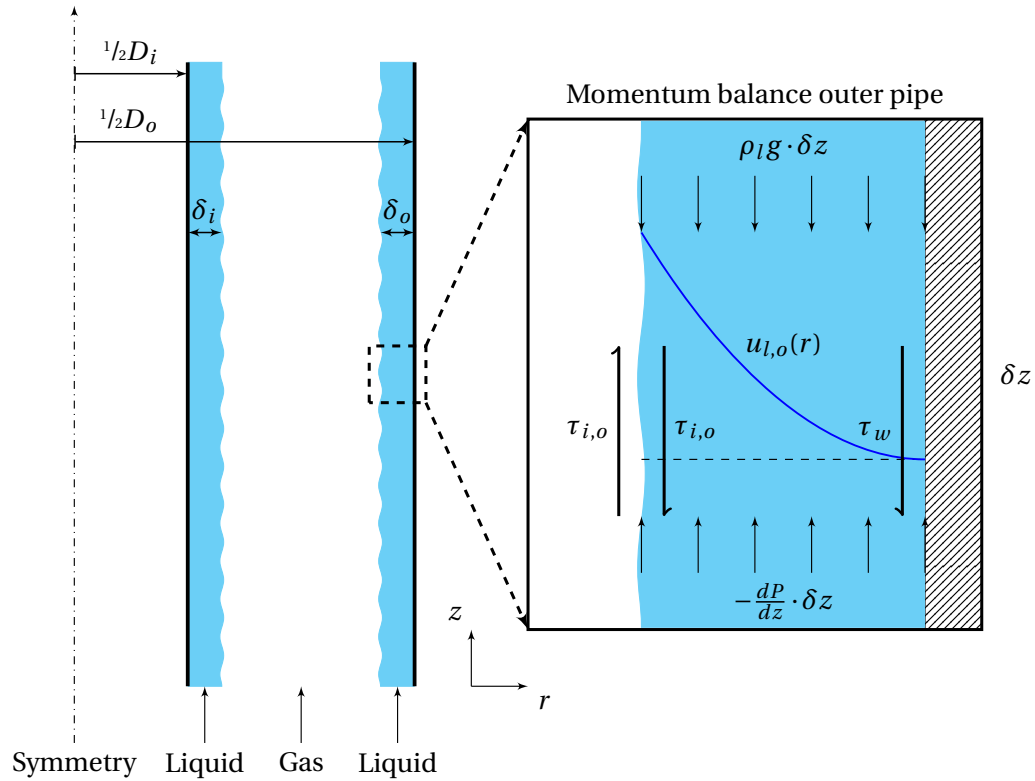
Figure 2.3: Right part of a vertical annulus. The dotted line represents the symmetry line. The zoomed in view shows the momentum balance for the liquid phase in a concentric annulus. When the momentum balance at the inner pipe is considered, the subscript o is changed into subscript i.

Momentum balance

The general way to approach the modelling of the pressure losses in an annulus is to set up a momentum balance for the different phases. The zoomed view in figure 2.3 shows the forces on the outer film layer. To make the momentum balance more accessible, the cross-sectional area of the liquid film at the inner and outer pipe are determined:

$$A_{l,i} = \frac{\pi}{4} \cdot \left((D_i + 2\delta_i)^2 - D_i^2 \right) \quad \text{(2.3a)} \qquad A_{l,o} = \frac{\pi}{4} \cdot \left(D_o^2 - (D_o - 2\delta_o)^2 \right) \quad \text{(2.3b)}$$

in which the δ_i and δ_o are the inner and outer film thickness, respectively. The gas core cross sectional area, A_g, is the cross sectional area of the annulus, $A_c = {}^\pi/_4 \cdot (D_o^2 - D_i^2)$, minus the areas calculated in equations 2.3a and 2.3b. The same is done for the circumferences at which the shear stresses are working. The wall shear stress, τ_w, works on circumferences $\mathcal{P}_{w,i} = \pi D_i$ and $\mathcal{P}_{w,o} = \pi D_o$ for the inner and outer wall, respectively. For the interfacial stresses, $\tau_{i,i}$ and $\tau_{i,o}$, the corresponding circumferences are $\mathcal{P}_{i,i} = \pi(D_i + 2\delta_i)$ and $\mathcal{P}_{i,o} = \pi(D_o - 2\delta_o)$.

The momentum balance for the phases in terms of these geometrical simplifications can now be constructed for an infinitely small δz. The momentum balance for the liquid film is

$$\underbrace{-\frac{dP}{dz} \cdot A_{l,n}}_{\text{Pressure gradient}} + \underbrace{\tau_{i,n} \cdot \mathscr{P}_{i,n}}_{\text{Interfacial friction}} = \underbrace{\rho_l g \cdot A_{l,n}}_{\text{Gravitation}} + \underbrace{\tau_w \cdot \mathscr{P}_{w,n}}_{\text{Wall friction}} \tag{2.4}$$

where n is either the inner or outer subscript. For the gas phase, the interfacial friction works in the opposite direction and the balance becomes

$$\underbrace{-\frac{dP}{dz} \cdot A_g}_{\text{Pressure gradient}} = \underbrace{\tau_{i,i} \cdot \mathscr{P}_{i,i}}_{\text{Interfacial friction inner}} + \underbrace{\tau_{i,o} \cdot \mathscr{P}_{i,o}}_{\text{Interfacial friction outer}} + \underbrace{\rho_g g \cdot A_g}_{\text{Gravitation}} \tag{2.5}$$

In these equations a relation for the shear stresses, τ_w, $\tau_{i,o}$ and $\tau_{i,o}$, can be modeled with a suitable friction factor, *i.e.* $\tau = \frac{1}{2} \cdot \rho \, f u^2$. The wall friction factor, f, can be considered as friction factor used for single phase pipe flow. Multiple relations exist, which incorporate the effects of wall roughness and turbulence. However, for the gas-liquid interfaces, this is not straightforward.

For two-phase flows in a single pipe, the interfacial friction has been thoroughly studied. Most of the interfacial friction factors are based on relation constructed by Wallis [49]

$$f_i = 0.005 \cdot \left(1 + 300 \frac{\delta}{D}\right) \tag{2.6}$$

where f_i is the interfacial friction factor, δ is the mean film thickness and D the diameter of the single pipe. The problem is that the estimation of the film thickness comes with great uncertainty. Ju et al. [23] reviewed most of the existing friction factor relations for single pipes and moreover constructed a relation which is independent of the film thickness. Instead, the relation uses the Weber number of the liquid phase and the modified Weber number of the gas phase. The results have a mean absolute percentage error of 15% for available empirical data, which is much lower than found with the other available friction relations.

When the annulus is considered, more parameters come into play. The question is whether the friction factor of the inner and outer film layer have to be treated independently or a general friction factor is sufficient. Moreover, the relations reviewed by Ju et al. [23] are all at least dependent on the pipe diameter, which is well defined for single pipes. However, for the annulus the characteristic length scale is less well known. Usually, the hydraulic diameter (equation 2.2) of the annulus is used instead. However, it is not yet known whether the hydraulic diameter works well for every case.

Entrainment

In the momentum equations, the momentum transfer through atomization and deposition of droplets in the gas core is not included. However, Fore and Dukler [17] concluded that in single vertical pipe flow, liquid entrainment contributes for 20% to the pressure drop along the tubing.

There are several entrainment models available, *e.g* the model proposed by Cioncolini and Thome [13], where the gas density, ρ_g in equation 2.5, is replaced by the effective gas core density ρ_{gc} containing small liquid droplets. In this model the gas core density is related to the core Weber number. Although the model performs well for single pipe flows, it might have to be adapted for the annulus geometry.

However, for the purpose of this study, it will be expected that entrainment will not play a dominant role in the momentum balance. Because of the low superficial liquid velocity in this study droplet entrainment is not dominantly present [40].

Mass balance
The momentum balances are constructed, but the model is not yet functional, because the thickness of the film layer is not yet known. To finalize the model, the actual liquid velocity profile in both the film layers needs to be calculated. This can be done by relating the shear stress in the film layer, τ_l (equation 2.4), to the radial position, r

$$\tau_l(r) = \left(\frac{\left(-\frac{dp}{dz} - \rho_l g \right) \cdot A_{r,n} + \tau_{i,n} \cdot \mathscr{P}_{i,n}}{\mathscr{P}_{r,n}} \right) \tag{2.7}$$

where, $A_{r,n}$ and $\mathscr{P}_{r,n}$ are similar to the equations defined in the momentum balance and are functions of the radial position r. When considering a Newtonian fluid, this relation can be integrated to find the velocity profile in the liquid layer:

$$u_{l,n}(r) = \frac{1}{\mu_l + \mu_t} \int_{wall}^{interface} \tau_l(r) dr \tag{2.8}$$

where, n is again either the inner or outer film layer, μ_l the viscosity of the liquid and μ_t is the added viscosity when considering turbulence. The latter is usually approached using the eddy viscosity [19, 28, 42]. To find the overall liquid throughput, equation 2.8 is integrated over the total liquid cross sectional area

$$\dot{V}_l = u_{sl} \cdot A_l = 2\pi \left(\int_{\frac{D_i}{2}}^{\frac{D_i}{2}+\delta_i} u_{l,i} \cdot r \, dr + \int_{\frac{D_o}{2}-\delta_o}^{\frac{D_o}{2}} u_{l,o} \cdot r \, dr \right) \tag{2.9}$$

With the use of equation 2.9, the mass is conserved and the film thickness can be solved iteratively.

Film thickness ratio
The above will serve as the basis for the model, however, not every parameter in the mass balance, equation 2.9, is available. As already discussed, the frictional factors and entrainment can be calculated by using correlations. In this section another important variable needs to be approached, namely the film thickness ratio, $\frac{\delta_i}{\delta_o}$. Equations 2.8 and 2.9 are depending on the film thickness at the inner and outer pipe. In the literature, a film ratio of one is assumed [26, 28, 38]. However, Andersen and Würtz [3] already concluded that the film flow on the outer pipe rate per unit perimeter can be two to five times larger than on the inner pipe. This is more or less experimentally confirmed by Arai et al. [5] for lower gas velocities, who used conductivity probes on the inner and outer pipes to measure locally the film thickness. However, Arai et al. [5] found that the ratio changes with an increased gas velocity towards the inner pipe.

Caetano et al. [11] developed a relation for this difference-based tendency of the entrained liquid droplets to deposit on the outer pipe as the projected view of these droplets is larger towards the outer pipe

$$T = \frac{\delta_i}{\delta_o} = \frac{W_i^{'}}{(2\pi - W_i^{'}) \cdot K} \tag{2.10}$$

where T is the film thickness ratio and $W_i^{'}$ is the planar view towards the inner pipe and K is the diameter ratio, *i.e.* $K = {}^{D_i}/_{D_o}$.

Because the planar view towards the inner pipe is a function of the droplet position, the planar view is averaged over the cross sectional area

$$\overline{W_i'} = \frac{16}{1 - K^2} \left(2 \cdot \sin^{-1}(K) + 2K \cdot \sqrt{1 - K^2} - \pi \cdot K^2 \right) \tag{2.11}$$

which can be used in equation 2.10. Caetano et al. [11] reported a fair usability for their total model, but they were not able to fully validate the ratio relation.

Modelling results reported in the literature
Yin et al. [51] and Kurian [28] both used a sophisticated version of the separated flow approach explained in this section. They used this model to predict the liquid hold-up and pressure drop.
Yin et al. [51] were able to predict the pressure drop and liquid hold-up with an error under 25%. They used an interfacial friction model developed by Ambrosini et al. [2] for single pipes. For the characteristic length scale, the hydraulic diameter is used and the film ratio is based on the results provided by Caetano et al. [11]. Kurian [28] predicted the pressure drop within 10% as compared to experimental data for higher superficial liquid flows. He assumed an equal film ratio between the inner and outer pipe and used the Wallis approach, equation 2.6, for the friction factor.

2.3. Onset of liquid loading
As discussed in section 2.1, the start of liquid loading in co-current upward flow is the occurrence of flow reversal, which corresponds with the transition from annular flow to churn flow. As can be expected from figure 2.2 the transition takes place at a certain superficial gas velocity and seems to be independent of the superficial liquid velocity. The approaches to find this 'critical' gas velocity for annuli will be discussed in this chapter.

Turner criterion
The first important criterion is due to Turner [46]. This criterion is based on the critical velocity for which the gas is no longer able to transport the largest entrained droplets upward in the flow. It starts with a force balance between the gravitational force and the frictional force on the largest liquid droplet present in the core. However, it is difficult to estimate the size of the largest droplet. In order to solve this problem, the diameter is related to a critical Weber number for which the droplet stays in tact. The Weber number relates the inertial force on the droplet and the surface tension of the droplet

$$We_{cr} = \frac{\rho_g D_p u_g^2}{\sigma_l} \sim 30 \tag{2.12}$$

in which, D_p is the droplet diameter, ρ_g the density of the gas and σ_l the surface tension of the liquid. For a co-current vertical annular flow, the critical Weber number corresponds with a value of 30. With the use of the largest drop diameter definition and the force balance, the critical gas velocity can be found:

$$u_g = 5.46 \left(\frac{\sigma_l \left(\rho_l - \rho_g \right)}{\rho_g^2} \right)^{1/4} \tag{2.13}$$

where u_g is the gas velocity and ρ_l the liquid velocity. In this equation a drag coefficient of 0.44 is assumed. When equation 2.13 is used for atmospheric conditions and $20°C$, the transition will take place at 14.5 m/s for an air-water mixture. Although this is a fair estimate which is widely used in industry, a few limitations have been formulated. For example, van 't Westende et al. [48] observed in a single pipe that the droplets are much smaller then calculated with the critical Weber number

and, even at liquid loading, are still moving upward. This makes the physical background of the Turner criterion for liquid loading implausible.

Froude number criterion and zero penetration
When looking at the equilibrium between the force of the gas phase to transfer the liquid upward and the gravitation force, the densimetric Froude number is considered, given by

$$Fr_{cr} = u_{sg} \left(\frac{\rho_g}{g\tilde{D}(\rho_l - \rho_g)} \right)^{1/2} \sim 1 \tag{2.14}$$

where g is the gravitational force and $\tilde{D}$ is the corresponding length scale of the considered geometry. Wallis [49] stated that flow reversal will start when the Froude number falls below one.

The other correlation is the zero penetration correlation, which was formulated by Pushkina and Sorokin [37]. They stated that the onset of flow reversal occurs when the gas core is able to penetrate through the liquid film. The relation is similar to equation 2.14, but instead of using the diameter as characteristic length scale, they used the characteristic wave length. This wave length can be related to the Taylor instability:

$$\lambda = \left(\frac{\sigma_l}{g(\rho_l - \rho_g)} \right)^{1/2} \tag{2.15}$$

This length scale is substituted in equation 2.14, which results in the Kutateladze number:

$$Ku = u_{sg} \left(\frac{\rho_g^2}{g\sigma_l(\rho_l - \rho_g)} \right)^{1/4} \sim 3.2 \tag{2.16}$$

Pushkina and Sorokin [37] found that a Kutateladze number lower than 3.2 corresponds with the penetration of the liquid film. So for atmospheric conditions mentioned above, the critical superficial gas velocity according to the zero penetration criterion for water will be 11.4 m/s.

Richter [38] tried to solve the contradiction between the Froude number criterion, which is dependent on a length scale, and the zero penetration criterion, which is not dependent on a length scale. Richter [38] states that both the critical Froude number and the zero penetration relation are valid for single pipes and annuli, but only when used in a specific diameter range. Richter [38] constructed a relation that unifies the complete geometry range for annuli into one formula. This relation has two extremes. For lower gap sizes $(D_o - D_i)$ the relation behaves as the critical Froude number and tends to go to 0.17. For the $\tilde{D}$, in equation 2.14, the mean circumference is used: $^1/_2\pi(D_o + D_i)$. For larger gap sizes the relation behaves as the Kutateladze number and tends to go to a value of 3.3. However, it should be noted that in this relation a uniform film ratio along the conduit is assumed which can be questioned as discussed in the previous section. Furthermore, the effect of entrainment is neglected.

Annular to churn transition models
For annuli a few models have been developed to find the flow regime transition. The two most convenient studies for two-phase flow will be discussed.

Kelessidis and Dukler [26] state that the flow will undergo regime transition when the void fraction for annular flow is equal to the liquid hold-up for churn flow. The hold-up for annular flow is determined in a similar way as described in section 2.2. In this analysis the Wallis friction factor is used (equation 2.6) for the interfacial friction, an equal film thickness for the inner and outer pipe

is assumed and the velocity profile in the film layer is derived using a power law. The hold-up for the churn flow is based on the ratio between the superficial gas velocity and the rise velocity of the Taylor bubbles.

Julia and Hibiki [24] proposed a transition model that is based on the model developed by Hibiki and Mishima [21] for rectangular ducts. They state that the two main mechanisms that induce the flow transition are (1) flow reversal of the liquid film and (2) the onset of droplet entrainment. The first criterion is met when the liquid flow has a wall shear stress of zero. Again using the momentum balance, given in section 2.2, it follows that the transition superficial gas velocity can be found by

$$u_{sg} = \sqrt{\frac{g \cdot \alpha_g^3 \left(\rho_l - \rho_g\right) \alpha_l \cdot D_h}{f_i \rho_g}} \tag{2.17}$$

where α_l is the liquid either found by measuring or modelling and f_i is the interface friction factor using Wallis relation (equation 2.6).

The second criterion can be found using the force balance on the liquid wave crest between the gas flow dragging the film up and the surface tension of the liquid film

$$u_{sg} \geq \left(\frac{\sigma_l g \left(\rho_l - \rho_g\right)}{\rho_g^2}\right)^{\frac{1}{4}} \cdot N_{\mu f}^{-0.2} \qquad\qquad N_{\mu f} = \frac{\mu_l}{\left(\rho_l \sigma_l \sqrt{\frac{\sigma_l}{g(\rho_l - \rho_g)}}\right)^{1/2}} \tag{2.18}$$

The latter criterion is only applicable for certain hydraulic diameters. For air-water two phase flow at ambient conditions, the hydraulic diameter must be larger than 26 mm. This model predicts the critical superficial gas velocity reasonably well with a small overprediction.

2.4. Disturbance waves

Until now, the interface between the liquid film and the gas core was assumed to be fully smooth. However, in reality this interface has a wavy appearance, which has an influence on the friction between the the gas core and the liquid film.

Taylor et al. [43] distinguished two types of waves, see figure 2.4, and stated that the appearance of these waves cover the complete annular flow regime. The first classification of waves is called the ripple wave, which has a relatively small amplitude, period and velocity with a non-coherent structure. The second and most interesting wave form is the disturbance wave. The disturbance waves are large kinematic waves travelling upward with a much higher velocity compared to the film velocity. These waves have the characteristic property that they appear in a circular shape along the circumference of the pipe and have a longer life time than ripple waves. Due to their size and chaotic behaviour, the disturbance waves have a great impact on the frictional pressure drop in annular flow[39]. Furthermore, [22] concluded that the disturbance waves are the main source of droplet entrainment in the gas core, causing momentum transfer between the gas core and the liquid film. Because of these reasons, the characteristics and influence of disturbance waves on the frictional pressure drop, will be the main subject of this section.

The characteristics of disturbance waves

Berna et al. [9] conducted a thorough literature review on the characteristics of disturbance waves. Some interesting studies will be discussed in this section.
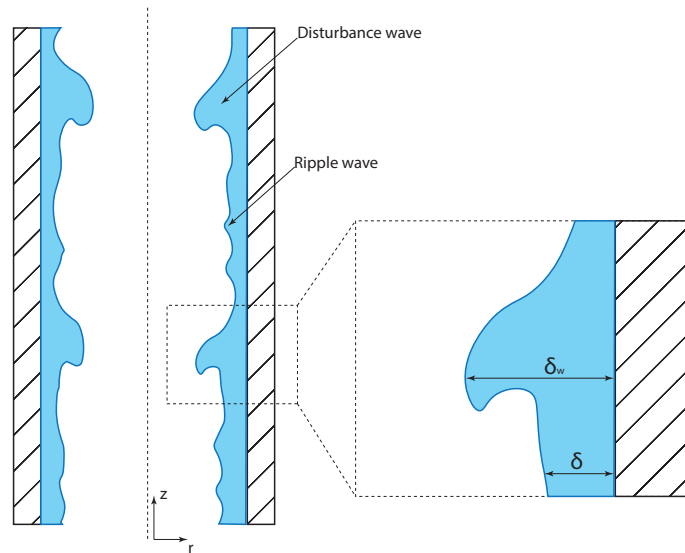
Figure 2.4: Cross-sectional side view of a single pipe with disturbance and ripple waves in a upward flow.

Taylor et al. [43] did a detailed study on the characteristics of disturbance waves in a single vertical pipe. They used conductance probes, together with an optical film technique and concluded that the wave frequency and velocity are increasing, with an increase of u_{sg} or u_{sl}. In another paper Taylor and Nedderman [44] concluded that the frequency at which the disturbance waves passes is decreasing in downstream direction, due to the coalescence of waves.

Martin [32] conducted a study on the relation of the pipe dimensions on the frequency of disturbance waves and concluded that there exists an inverse relationship between the pipe diameter and the frequency. Furthermore, it was concluded that the pipe diameter does not affect the wave speed.

Sawant et al. [39] also included the height of the disturbance waves in their study. The film heights, frequency and velocity were measured for a wide range of u_{sg}, u_{sl} and different pressures using conductivity probes. It was concluded that an increasing gas velocity has a inverse relation with the disturbance wave height. Furthermore, their data revealed a proportional relation between the liquid rate and the disturbance wave height. Sawant et al. [39] formulated an empirical correlation based on their data to find the frequency of the disturbance waves in single pipes

$$f_w = 0.086 \cdot Re_f^{0.27} \cdot \left(\frac{\rho_l}{\rho_g}\right)^{-0.64} \cdot \left(\frac{u_{sg}}{D}\right) \qquad\qquad Re_f = \frac{\rho_l u_{sl} D}{\mu_l} \qquad (2.19)$$

where f_w is the wave frequency, Re_f the film Reynolds number and μ_l is the viscosity of the liquid. Sawant et al. [39] obtained this empirical relation using a regression analysis and validated the results by using available data in the literature. The correlation was able to predict the frequency within 25% deviation.

Empirical data on disturbance waves for an annulus configuration are lacking. Arai et al. [5] were one of the few to investigate the characteristics of disturbance waves on the inner and outer pipe walls of an annulus. They compared their own data to the data provided by Sawant et al. [39] and concluded that the disturbance wave velocity on the inner pipe behaves in a similar fashion for an increased gas Weber number. The disturbance wave velocity at the outer pipe behaves differently when the gas Weber number exceeds 1000. Arai et al. [5] concluded that for these Weber numbers, the large disturbance waves transited to slower ripple waves.

The effect on the interfacial friction

Due to the large amplitude (δ_w - δ) of the disturbance wave, the large difference between the gas and wave velocities, and the large density ratio between the gas and liquid, the wavy interface of the liquid can be seen as an extra apparent "wall" roughness for the gas flow. This roughness is often linked to sand-grain roughness, k_s, for single phase flow. Many of the interfacial friction factors discussed in section 2.2, are more or less based on the analogy with this sand-grain roughness, k_s. The famous and widely used relation formulated by Wallis [49], see equation 2.6, was based on this assumption. He fitted four sets of annular flow data as function of the ration between the mean film height and the diameter of the pipe, δ/D and concluded that the disturbance wave amplitude (δ_w - δ) is equivalent to four times the sand-grain roughness, k_s. This only holds for the fully rough regime.

Later, various modifications were formulated in the literature. Fore et al. [18] tried to solve the interfacial friction for the transition roughness and therefore also added the Reynolds number of the gas phase. However, no physical background was provided.

Belt et al. [8] disputed the Wallis approach and concluded that there exists indeed a proportional relation in the fully rough regime, but this proportionality depends on the solidity, which is equal to the frontal roughness area perpendicular to the flow. The solidity is a function of the wave velocity, height and frequency. They formulated a new empirical relation for interfacial friction factor in the fully rough regime.

Wang et al. [50] conducted a study on the relation between the interfacial friction and disturbance waves, in which the wave shape was taken into account. They found that the interfacial friction factor is less dependent on the wave height than what is used in the single phase roughness analogy and concluded that this is probably due to the wave shape.

Pan et al. [35] built an empirical model to predict the interfacial friction. However, this approach was based on a momentum analysis of the wave, in which the wave shape, wave spacing, mobility of the interface, entrainment, and gas eddy effects, were taken into account. They concluded that approximately 26% of the pressure drop is due to the contraction of the cross-section and the mobility of the interface for a single pipe.

With respect to an annulus, less research has been conducted to establish the impact of turbulence waves on the interfacial friction. This is certainly the case for eccentric annuli.

2.5. Eccentricity

The tubing, used in the oil and gas industry, are up to a few kilometers long. When an inner pipe is inserted to create the annulus, it is difficult to keep the inner pipe concentric over the whole length of the pipe. This causes that some parts of the annulus will slightly move making it eccentric.

The degree of eccentricity is defined with the eccentricity parameter e, see equation 2.20. In this equation E is defined as the centre displacement of the inner pipe, see figure 2.5. When the eccentricity equals 1, the annulus is called fully eccentric, when the inner and outer pipe are in contact with each other. Eccentricity carries some extra challenges, *i.e.* the geometry is not axialsymmetric anymore and the film thickness in circumferential direction for annular flow is not equally distributed, which can induce different flow regimes at different tangential positions. These are all factors that makes the modeling complex. In this section the few existing studies on annular flow in an eccentric annulus will be discussed.

$$e = \frac{2 \cdot E}{D_o - D_i} \qquad (2.20)$$
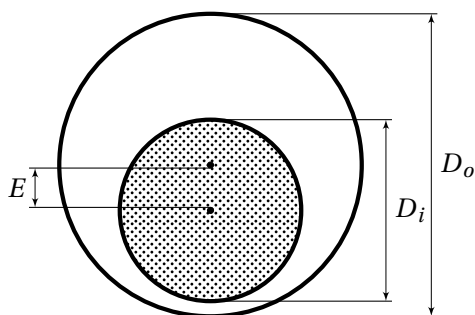
Figure 2.5: Eccentricity parameter.

Flow pattern map

In table 2.1 two studies on eccentric annuli are also listed. The results of the studies conducted by Caetano et al. [10] and Kelessidis and Dukler [26] are summarized in figure 2.7. When these results for different eccentricities and the results for concentric annulus from figure 2.2 are compared, it suggest that an eccentric inner pipe induces the flow transition to occur at slightly lower superficial gas velocities than the concentric configuration. However, this hypothesis is weak as the two different studies are difficult to compare because of the subjectivity factor in the flow regime determination and the differences in velocities are rather low.

Modeling of an eccentric annulus

The above mentioned challenges also impact the modeling. Caetano et al. [11] were among the first to develop a relation for the liquid hold-up in an eccentric annulus. The results showed on average an overprediction by 15% of the hold-up and an underprediction by 14% for the pressure drop in the tubing. These experiments were all conducted using a fully eccentric annulus. They devoted the lack of accuracy of the model to the strong dependence on the entrained liquid fraction and on the film thickness ratio.
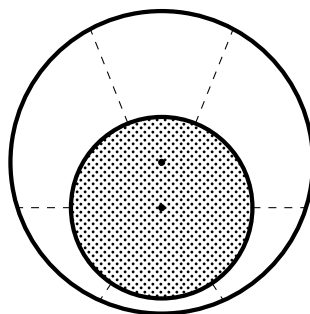
Figure 2.6: Cross sectional view of an eccentric annulus divided in control volumes. Modeling strategy used by Kurian [28].

Kurian [28] conducted a thorough study on the modeling of an eccentric annulus, with the approach discussed in section 2.2 as foundation. Instead of considering the complete geometry as Caetano et al. [11] did, he divided the flow area in segments as can be seen in figure 2.6. For each control volume he solved the momentum and mass conservation equations. The power of this approach is that for every segment a different characterization can be used. This approach gave results with a 6% accuracy for the pressure drop, which is a great improvement compared to the results of Caetano et al. [11]. However, to close this model, a new unknown parameter appears, namely the film
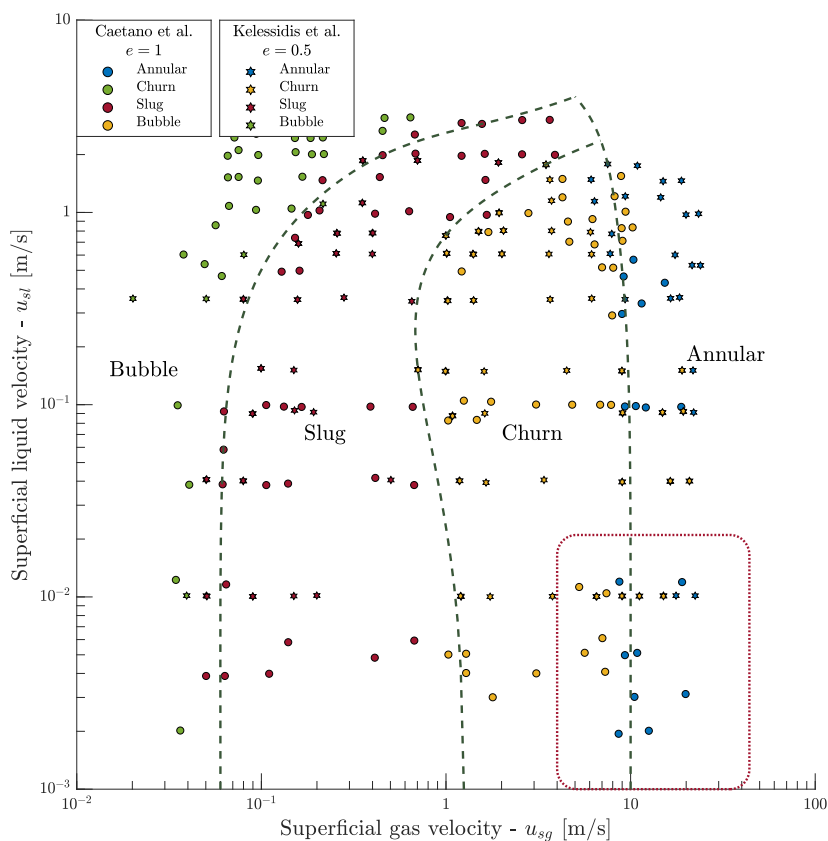
Figure 2.7: Flow pattern map for an air-water flow in a vertical eccentric annulus. The red dotted rectangle is the area of interest for the experimental study in this thesis.

thickness distribution along the circumference of the inner pipe. Kurian [28] needed to assume this distribution. In the literature, this distribution has not yet been studied. An experimental study is needed to improve the model, which is an important objective of the present study.

2.6. Project objective

In this literature review the different experimental studies on flow regimes and modeling of annular flow in concentric and eccentric annuli were discussed. It became clear that to be able to create a effective predictive model there is still a lack of empirical information. Specifically, the closure between the film ratio on the inner and outer pipe walls is not fully understood yet, as well as the circumferential film distribution on the inner and outer pipe walls, when concerning an eccentric annulus.

The main objective of this thesis is to find the lacking information to make the existing models more accurate. Firstly, a representative scaled annulus set-up needs to be developed and built. In this set-up the pressure drop is measured for the combination of superficial liquid and gas velocities which are representative for the industrial applications. These data will be used to compare the model results provided by Kurian [28] and to find the onset of liquid loading.

Secondly, as was discussed in the previous section, a suitable method needs to be developed to find the film fraction for concentric annuli and the film thickness distribution in circumferential direction for eccentric annuli. Furthermore, the characteristics of disturbance waves needs to be studied for the concentric and eccentric cases, since there is no empirical data on this topic.

Lastly, more insight in the development length of the flow is needed. The option to inject the liquid flow on either the outer or inner pipe in combination with the pressure measurements close to the inlet will be crusial to answer this question. Although, the development length is slightly geometry dependent, it enhances the other two objectives.

Research questions

For this project, the following research questions have been formulated:

- What are the best measurement techniques to acquire the flow parameters in a vertical concentric and eccentric annulus?

- How does the film ratio depend on the concentric annulus configuration and on the flow velocities?

- What is the impact of eccentricity on the pressure drop, onset of liquid loading, characteristics of disturbance waves and film distribution and can this effect be converted into a relation?

3

Experimental setup

In order to meet the previously discussed objectives a new experimental set-up had to be designed and constructed. This set-up will initially operate with an air-water mixture. The most important design requirements are the length and diameters of the tubing. A short list of the set-up requirements has been defined to meet the objectives:

- **The geometry sizes**. The tubing will have a length of 12 meter, consisting of an outer pipe with an internal diameter of 124 mm. This size is representative for the tubing used in the industry. For the purpose of this thesis, only one internal pipe with an outer diameter, D_i, of 100 mm will be studied. In the near future, experiments will be conducted using an inner pipe with a diameter of 80 mm as well. This second inner pipe needs to be taken into account during the design process.

- **Eccentricity**. It must be possible to adjust the inner pipe position in order to make the set-up eccentric. An eccentricity factor (*e*) of 0, 0.5, 0.75, 0.9 and 1 will be studied.

- **Liquid injection**. It must be possible to inject the liquid flow separately on the inner and outer pipes. This option is needed in order to find the development length of the system and to study the redistribution of the liquid films on both pipes.

- **Separated outflow**. The liquid film on the inner and outer pipe must be separated at the outlet to determine the global film ratio between the two pipes.

- **Pressure measurement**. The set-up needs to be equipped with pressure sensors at different axial positions. This will provide the development length and most importantly, the pressure drop along the annulus.

- **Temperature measurement**. Two temperature sensors will be mounted to find the temperature drop of the flow between the inlet and outlet.

- **Hold-up and film thickness measurements**. The liquid fraction in the tubing must be measured in respectively a local and global manner. The local measurement will measure the local film thickness on the inner and outer pipes and this will give the film ratio. In the case of eccentricity, the local measurement can be used to find the circumferential distribution. The global hold-up measurement will be done by draining the total liquid amount in the set-up.

- **Liquid loading measurement**. A capacitance sensor needs to be installed below the liquid injection point, which triggers a signal when water is flowing downward. With this technique the first signs of liquid loading can be measured.

21

This chapter will cover the development of the set-up design, the discussion of the flow loop and the implementation of the required sensors. The development of the local film sensor will be covered in Chapter 4. A picture of the final set-up can be found in Appendix D.

3.1. Development

This section will discuss the relevant design considerations during the development of the annulus set-up.

Pipe segments

It was decided to produce the full tubing of the set-up using transparent polymethyl methacrylate (PMMA) in order to enable flow visualisation. To facilitate the installation easier, both the inner and outer pipes are split in interchangeable segments of either 0.99, 0.70 or 0.3 meter.
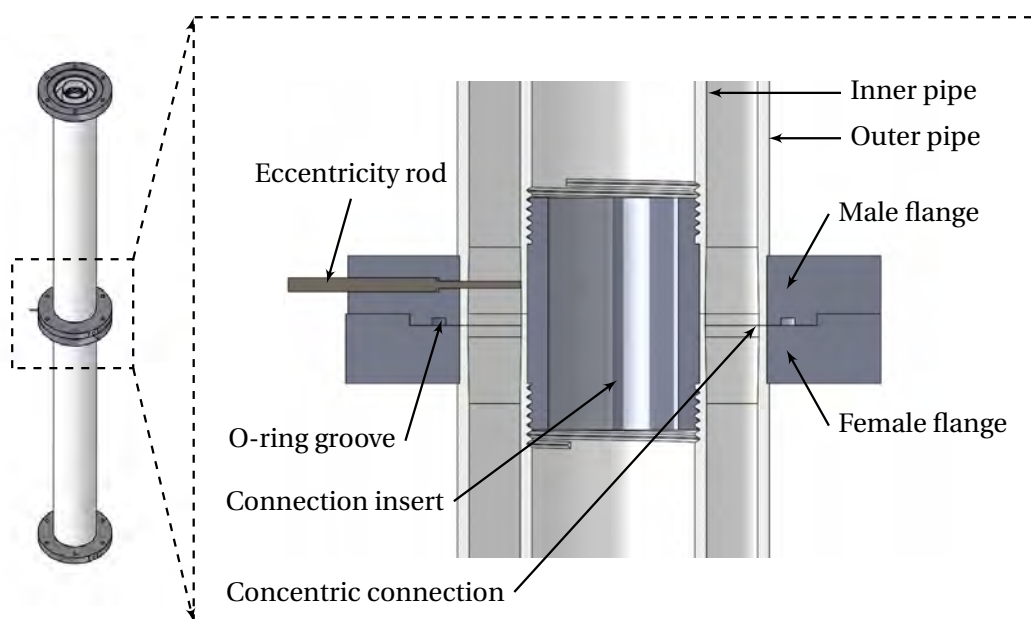
Figure 3.1: Pipe segments. Left, exploded view of two connected pipes. Right, a cross-sectional side view of the inner and outer pipe connection with the important parts. In this figure, the 80 millimeter inner pipe is displayed.

In figure 3.1 the connection of the pipe segments are shown. The outer pipes are connected by flanges with in between an O-ring to ensure a leak tight connection. Each pipe is glued to a male and female flange. The male flange is equipped with the ability for the eccentricity support of the inner pipe, using three eccentricity rods. The inner pipes are connected via a connection insert. These inserts are furnished with threads to tighten the inner pipes onto each other and having a fit to ensure full concentricity.

Casted PMMA pipes are used to reduce the tension in the material after gluing the parts together. However, PMMA in combination with casting is not geometrically stable and diameters can vary by 1%. In other words, if no measures are taken, the connection between the segments are not fully smooth, which may disturb the flow. Therefore, the ends of the pipes are made fully concentric. This is achieved by enlarging the diameter by 1 millimeter and gradually turn the diameter to their original diameter in a one degree angle using a lathe.

Inlet design

In the inlet, gas and liquid are injected in the system. Figure 3.2 shows the most relevant parts of the inlet. The inlet is constructed out of two covers with in between a large pipe in which the gas is injected. The gas is injected at five points in the air chamber and flows against a 'turbulence inducer' in order to homogeneously mix the air before it enters the system.

One of the requirements is the ability to separately apply the liquid onto the inner and outer pipe. In figure 3.2 it can be seen that the liquid inlet for the inner pipe flows through the foot which fixates the inner pipe at its origin. The foot can be moved by inserting different eccentricity plates in the lower cover. The liquid injection in the outer pipe is realized through a mantle around the pipe in which a liquid column is built up.
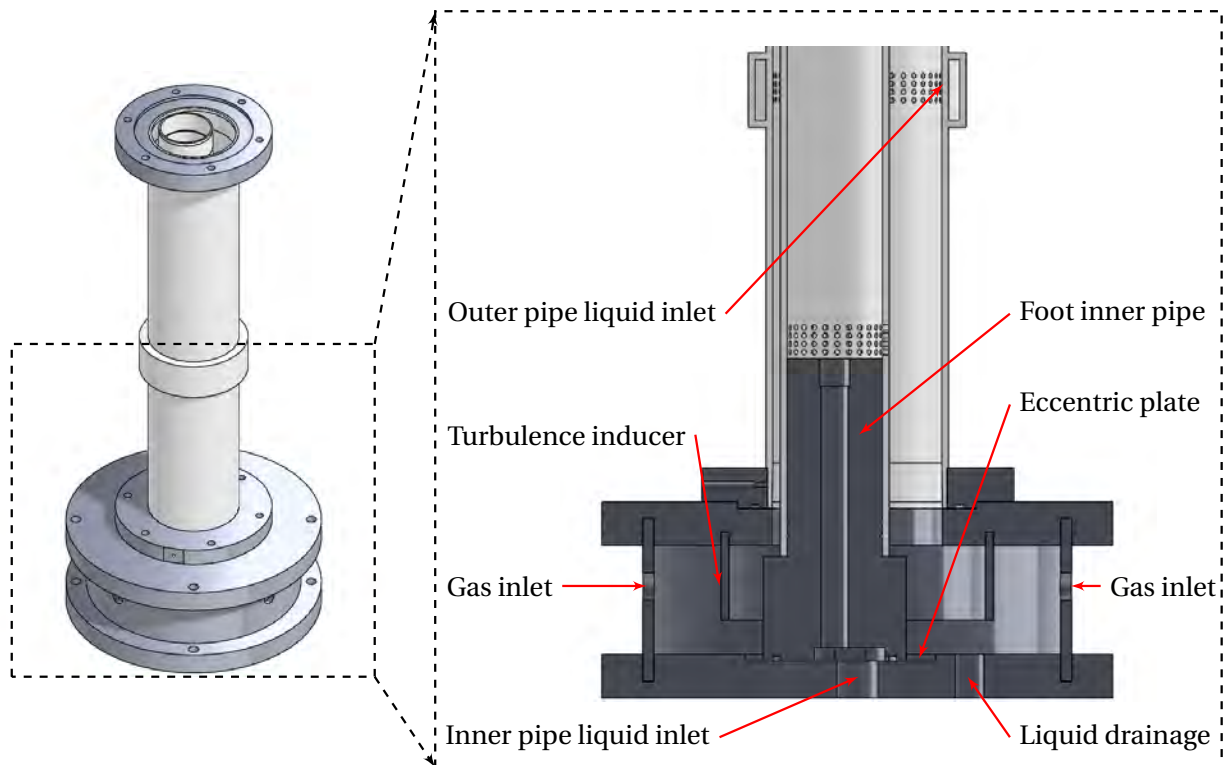
Figure 3.2: Inlet design at an eccentricity of 0.9. Left, exploded view of the inlet section. Right, the cross-sectional side view of the inlet.

The number of holes and its diameter through which the liquid is injected in the system need to be selected with care. Larger holes will induce a pulsating flow causing a longer developing length. Smaller and less holes can induce a liquid jet, causing the liquid to reach the other pipe to early. After some preliminary tests it was chosen to equip both injection systems with four rings of 30 holes, all having a diameter of 2.5 mm.

At the lower cover, three drainage holes are located. Through these holes, the system can be drained after having performed a test to measure the global liquid hold-up in the system.

Outlet design

The outlet has to split and collect the inner and outer film flows of the two pipes, in order to get a global film ratio. In figure 3.3 the design is shown how this is realized. The two collector chambers are similar to the design of the inlet. The flow splitter and flow adapter are changing the direction

of the flow, causing the liquids to flow in the collectors. Due to the high gas velocity the mixture will flow through the outlets to the measurement section. These outlets need to be sufficiently large to slow down the flow. The upper film collector is connected to the inner pipe and thus needs to be able to move over the lower film collector. The seals prevent the liquid to leak between the collectors.
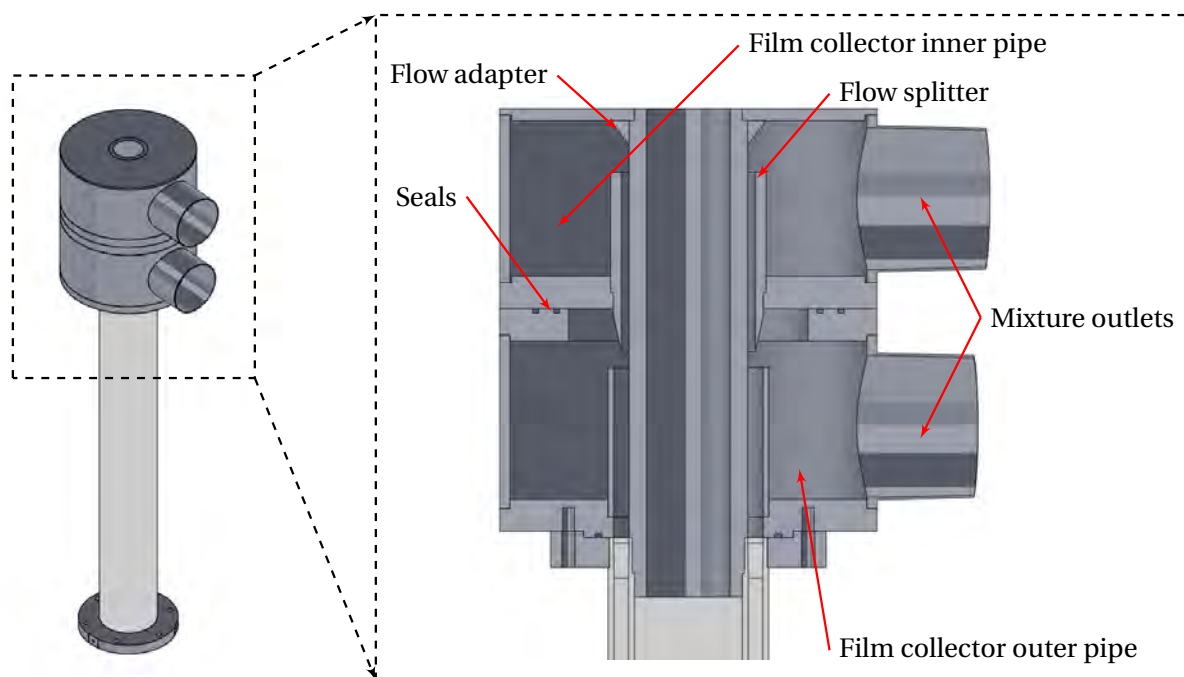
Figure 3.3: Outlet design. Left, exploded view. Right, the cross-sectional side view of the outlet with the two flow collectors.

3.2. Flow loop

In the previous section the development of the set-up was discussed. This section will cover the peripheral equipment, such as sensors and flow controllers. Figure 3.4 shows a schematic image of the complete flow loop with the concerning sensors. In table 3.1 the specifications of the discussed sensors can be found.

The gas circuit

The gas is supplied at 8 bar from the in-house compressed air grid and is reduced to 5.5 bar required for the gas flow meters. Because the system uses more air than the grid can deliver, an auxiliary compressed buffer tank of 10 m^3 is installed for the higher gas flows. Three gas flow meters control the flow speed. The highest throughput of air which can be delivered to the system is approximately 11,000 liters per minute. This amount corresponds to a superficial gas velocity of 43 m/s for the 100 mm inner pipe and 26 m/s for the 80 mm pipe. At the outlet the gas is separated from the liquid and released at atmospheric pressure.

The liquid circuit

The system will run on normal tap water, which is delivered to the system from a water reservoir. Two calibrated liquid flow meters in combination with a membrane valve will control the liquid inflow for respectively the inner pipe and the outer pipe. The flow controllers are calibrated by measuring the output flow per minute using a scale for different flow throughputs. The desired superficial liquid velocity will vary from 5 to 20 mm/s.

At the outlet the two liquid films are separated, collected and continuously weighted using two scales in order to find the global film ratio on inner and outer pipe. Each of these scales consists of three calibrated load cells with a total maximum load of 50 kg. After each run, the gas flow is immediately stopped using an electronic valve. At the inlet, the electronic valve for the drainage is opened in order to transport the collected liquid in the tubing through the drainage holes to an industrial scale with a maximum capacity of 50 kg.

Measurement equipment

The pressure is measured using six pressure sensors, which are respectively positioned at 3.2, 4.2, 5.2, 6.2, 8.2 and 11.2 meter in axial direction. The maximum load of the sensors is estimated by the results provided by Kurian [28]. The pressure gradient is measured downstream of the tubing. All pressure sensors are manually calibrated by applying five different loads to the sensors, from which a calibration curve could be extracted.

The temperature sensors are located 11.4 meter apart. The temperature sensors are firstly used as an extra check whether the system has reached a steady state. Secondly, the temperature gradient can be measured along the tubing. Furthermore, the temperature is an input for the calibration curves of the the film sensors. The temperature sensors are calibrated at different temperatures from which a calibration curve could be derived. This is done using a calibrated PT-100 as the reference.

A capacitance sensor is installed below the liquid injection of the outer pipe. In normal operation, when all liquid is flowing upward, the output signal is approximately 5.8 V. However, when water is flowing downward, which occurs during the onset of liquid loading, the capacitance of the sensor changes. This induces a amplified output signal of approximately 8 V.

Two 16 bit CMOS cameras are positioned at 8.2 meter in axial direction. One camera, with a frame rate of 100 Hz, is placed perpendicular to the eccentricity direction. The other camera, with a frame rate of 50 Hz, captures the top view, which is mounted parallel to the eccentricity direction. Two led panels are used to increase the contrast and create a homogeneous backlight.

Table 3.1: Specification of the sensors implemented in the annulus set-up.

Measuring point	Sensor		Range	Accuracy
	Type	Amount and name		
Gas flow meters	Thermal mass flow controller	1 - D-6383-DR/BJ2.8	25 - 2500 l/min and closed	±1% R.D. plus ±0.5% F.S.
		2 - D-6383-DR/BJ4.4	50 - 5000 l/min and closed	
Liquid flow meters	Magnetic inductive flow sensor	1 - MVM-020-PA	1.0 - 20 l/min and closed	±2% R.D.
		1 - Sika VMI-07	0.5 - 30 l/min and closed	±1.5% R.D. plus ±0.3% F.S.
Scales	Load cells	6 - Celtron STC-50kg	0 - 50 kg	±0.25% F.S.
	Industrial scale	1 - Kern CFS 50K-3	0 - 50 kg	Linearity: 2 g
Pressure sensors (bottom to top)	Analog pressure transmitters	3 - ATM 250 mbar	0 - 250 mbar	±0.1% F.S.
		2 - GE UNIK 5000	0 - 150 mbar	±0.2% F.S.
		1 - GE UNIK 5000	0 - 70 mbar	±0.2% F.S.
Temperature sensors	Thermocouple	2 - RMA 421 (controller)	0 - 25 °C	±0.05% F.S.
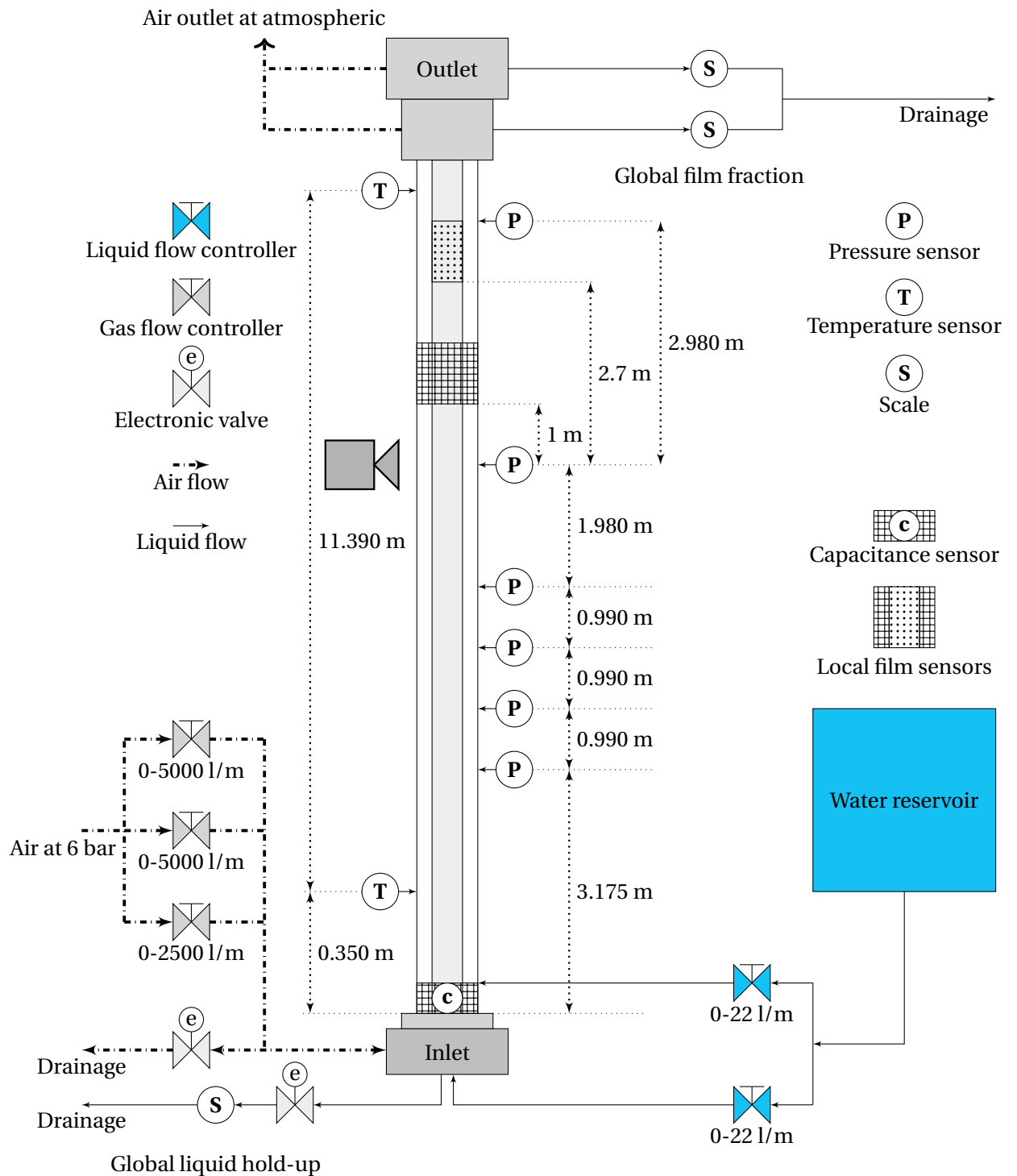
Figure 3.4: Flow loop of the annulus set-up with the used flow controllers, valves and sensors.

4

Local film sensor development

The thickness and dynamics of the liquid film in annular flow will contain a large amount of information on the stability of the flow. This can be linked to the interfacial friction between the liquid film and the gas core, which is an important parameter in the pressure drop calculations. It is often mentioned that the currently available empirical data lack this information for the annulus configuration, especially when eccentricity comes into play.

Many methods to measure the thickness of a liquid film have been described, *e.g.* acoustic, optical and electrical measurement techniques. These techniques can be distinguished into local and global measurements, intrusive and non intrusive measurements and dynamic and static measurements. Tibiriçá et al. [45] reviewed fourteen techniques and their measurement ranges. Furthermore, they subdivided the techniques into the above mentioned classes. Based upon this review paper, the available literature and the complexity of the annulus set-up, it has been chosen to use flush mounted conductance probes to locally measure the film thickness. With this technique it is also possible to install multiple local measurement points, in order to obtain the circumferential film height distribution.

In this chapter the development of the local film sensor, *i.e.* the conductivity probes, will be discussed. The first section will give a brief background on the usage of this technique and the progress it has made over the years. The subsequent section will cover the signal response and the required electrical circuit to be able to measure a liquid film. Then the probe dimensions will be analyzed with respect to the available measurement range and signal strength. In the last section the calibration and the final implementation of the sensors are discussed.

The development of these sensors was a large part of the present study and many steps and pre-studies were conducted. These steps and pre-studies are described in Appendix A, which shows an extensive road to reliable film thickness sensors.

4.1. Background
The idea behind conductance probes is straight forward. Two closely placed 'probes' are in contact with the conducting film flow and together form a conductivity probe pair, see figure 4.1. One probe induces an electrical current by means of an electrical potential difference. This probe is therefore called the transmitter. The other probe called the receiver, receives the current. The liquid film acts like a resistor and capacitor in parallel, for which the electrical behaviour depends on the height of the liquid film, δ, and on the conductivity of the liquid, γ. A thicker liquid film has a lower resistance
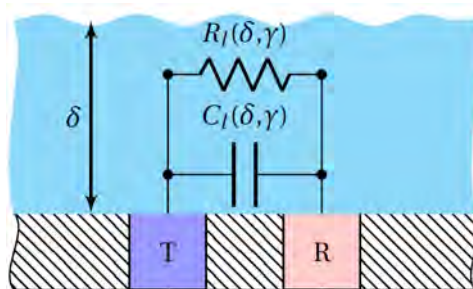
Figure 4.1: The concept of the conductivity probe pair, *i.e.* film height sensor. The transmitter (T) and the receiver (R) are in contact with a conductive film layer.

and thus gives a stronger signal. In this way the receiver and transmitter form together a local film height sensor. This technique has been used frequently in the past to find liquid hold-ups and film thicknesses in multiphase systems.

There are different ways to implement the probes in the tubing. Each of these arrangements has its strengths and weaknesses. In figure 4.2, the most widely used arrangements are shown. The authors mentioned in section 2.1, summarized in table 2.1, made use of wire probes (see the left side image in figure 4.2) to distinguish the flow patterns [16, 25, 26]. These wire probes have a higher measurement range, which make them suitable for thicker films and wave measurements. Koskie et al. [27] theoretically derived the characteristics of these probes and used them to study wavy fronts in falling films in single pipes. Andreussi et al. [4] used simulation software instead of a theoretical approach, to optimize their wire probes. Multiple sensors were implemented in a nearly horizontal pipe in order to find the film height distribution. A high conductance tracer was added to the flow to find the film velocity. Although a very local measurement is possible, the probes are intrusive and therefore disturb the film flow. This is also what Andreussi et al. [4] found in their study. For relatively smaller films (<2 mm) this disturbance, together with surface tension effects, can bias the measurements.

Therefore, flushed mounted probes are used for very thin films. One example is the ring electrodes (middle of figure 4.2). This arrangement averages the liquid film height over the circumference, which makes it very suitable for general hold-up and height fluctuation measurements. This technique was used by Sawant et al. [39] to measure the dynamics of an upward vertical film flow in a single pipe. Since one of the goals of this study is the circumferential distribution of the film thickness, it is required to locally measure the small film thickness. This must be done at multiple positions along the circumference of the inner and outer pipes. Therefore, the ring electrode can be replaced by multiple flush mounted probe pairs (see the right side arrangement in figure 4.2). This solution is still capable to measure the film thickness at a high resolution without disturbing the flow.

Belt [7] was one of the first to use this technique. He used a ring electrode as transmitter and single probes as receivers. Belt [7] connected the transmitters and receivers in such a way, that the amount of cabling and the required data acquisition are strongly reduced. This technique is called a sensor mesh measuring technique and was developed by Prasser et al. [36]. With this technique Belt [7] was able to measure the film thickness at 320 locations nearly simultaneously in a single pipe. This made it possible to measure the wave velocities and the film distribution. The sensor mesh technique was further developed by Damsohn and Prasser [15].
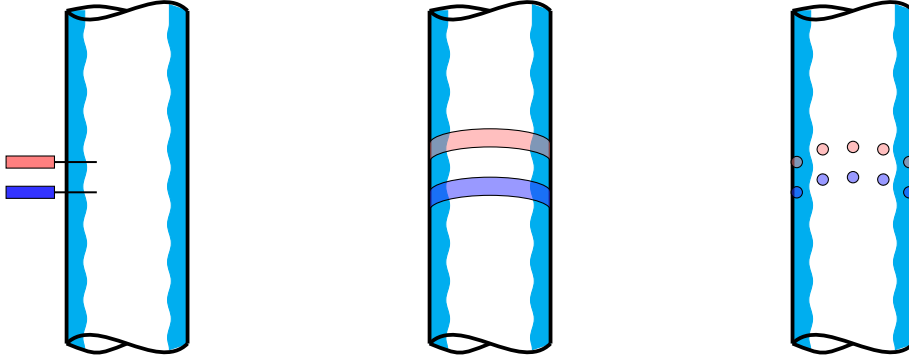
Figure 4.2: Possible transmitter (blue) and receiver (red) probe arrangements in a single pipe. Left, intrusive needle probes. Middle, two flush mounted ring electrodes, which cover the complete circumference. Right, multiple flush mounted probe pairs.

They fully studied and optimised the shape of the probes. The optimised shape and wiring was printed on a *Printed Circuit Board* (PCB) with high accuracy. With this technique they were able to measure thin films at 1024 locations on a flat plate. The latest development is to use flexible PCBs in combination with the sensor mesh technique for usage at complex geometries. Arai et al. [5] used this latter technique in an annulus configuration.

4.2. Theory

The next sections and appendix A will discuss all the considerations made in the development of the film sensors. Therefore, a small theoretical background is given here.

Probe characteristics

Coney [14] provided an extensive theoretical background based on potential field theory for the characteristics of flush mounted probes. In figure 4.1, it was shown that the liquid film can be considered as a resistance and capacitance in parallel. In specific cases, which will be discussed later in section 4.3, the impedance of the film is dominated by the resistor. For that case it is assumed that the conductance between the probes, G (in Siemens), has a linear relation with the conductivity of the liquid, γ (in Siemens per meter), and the length of the probe, l

$$G = G^* \cdot \gamma \cdot l \tag{4.1}$$

where G^* is the dimensionless conductance factor, which depends on the (2D) geometry of the flush mounted probe and the film height δ. This G^* can be found using

$$G^* = \frac{K(m)}{K(1-m)} \qquad\qquad m = \frac{\sinh^2\left(\frac{\pi d_w}{2\delta^*}\right)}{\sinh^2\left(\frac{\pi(d_w + d_p)}{2\delta^*}\right)} \tag{4.2}$$

where K is the complete elliptic integral of its first kind as function of m, the geometrical information of the system. d_w is the width of the probe and d_p the distance between the probes. Coney [14] considered rectangular shaped probes on a flat surface, in equation 4.2. For circular shapes such as pipes, δ^*, needs to be compensated and becomes

$$\delta^* = -\frac{1}{2}D \cdot \ln\left(1 - \frac{2\delta}{D}\right) \tag{4.3}$$

where D is the considered diameter of the pipe. For a fixed pipe geometry (D = 100 mm) the results of equations 4.2, as function of the probe width (right) and distance (left), are shown in figure 4.3.
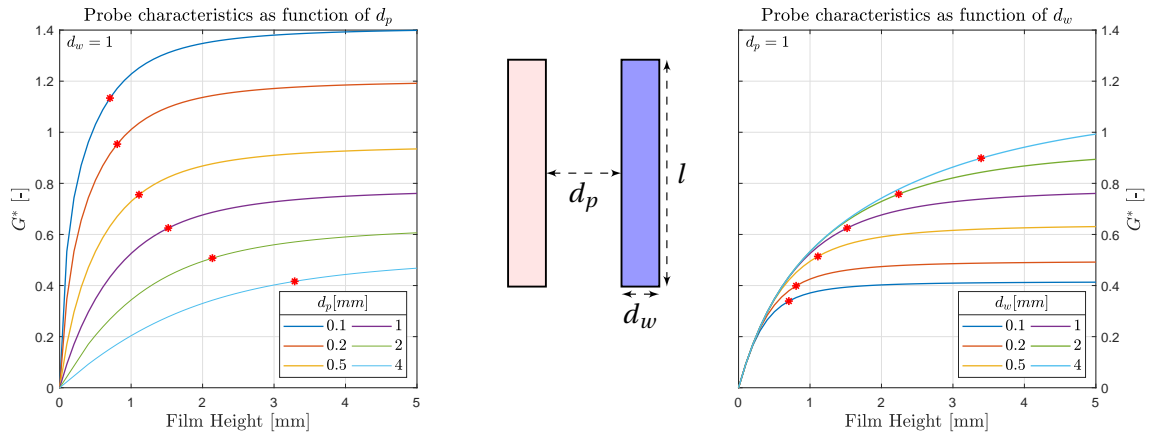
Figure 4.3: Probe conductivity characteristics as a function of the distance between the probes (left) and probe width (right). The red dots $*$ are the points at which the signal is at 80% of the saturation signal. In the centre, the frontal view of the considered transmitter and receiver probes is presented.

As can be seen in figure 4.3, each combination of probe width and distance has a film height at which the signal is saturated. The red dots show the height at which the signal is at 80% of the saturation signal. This can be seen as the maximum height that the sensor is able to measure, *i.e.* the measurement range of the sensor. The conductance factor, G^*, on the vertical axis, represents the strength of the retrieved signal. From figure 4.3 it can be seen that a larger probe distance, d_p, enlarges the measurement range, but weakens the signal. The width of the probes, d_w, shows a different behaviour. A larger probe width strengthens the returned signal, enlarges the measurement range and therefore makes the sensor more sensitive to height fluctuations.

Spacial resolution

The above mentioned dimensions of the probes have a large effect on the special resolution of the sensor. This has to do with the conductance lines which pass from the transmitter, through the liquid, to the receiver. Figure 4.4 shows two sensors with different probe widths and distances. The parabolic-shaped dotted lines represent the conductance lines. Sensor 1 has a smaller probe distance and is therefore able to measure the crest of the wave, because the conductance lines are not hindered. However, due to the close distance between the probes, the sensor has a limited measurement range. Sensor 2 is not able to measure the wave crest since the conductance lines cannot propagate through the liquid interface. When the period of the waves is relatively small compared to the distance between the probes, the average film thickness will be underpredicted. This is the case for sensor 2. So, a trade-off always exists between special resolution and the measurement range.

Besides the wavy air-water interface, there is another phenomenon that impacting the special resolution. In the flow transition from annular to churn flow, small gas bubbles will be enclosed in the liquid. These bubbles will cause a smaller effective area through which the conductance lines can propagate and this results in an underestimation of the liquid film height.
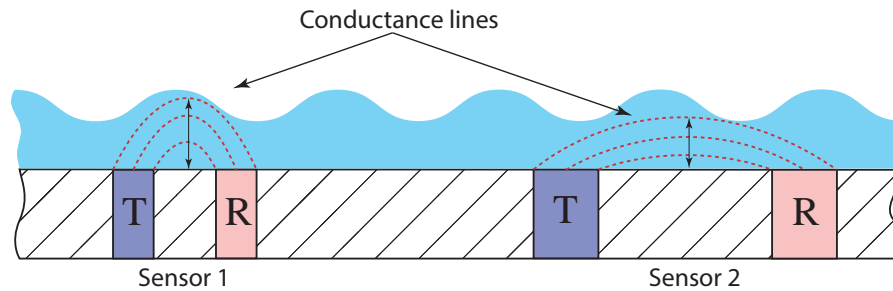
Figure 4.4: The conductance lines for two different sensors, together with the measured height.

Electrolytes and flow velocity

The set-up runs on an air-water mixture. In the used tap water, electrolytes are present, which can affect the characteristics of the sensor. Coney [14] investigated the effects of these electrolytes. Ions in the liquid tend to be deposited onto the probe, charged with the opposite charge, creating a double layer. The double layer is not beneficial for the measurement as it creates an extra unsteady resistance, which is comparable with a capacitor and resistance in series. Coney [14] suggests that an excitation frequency of the transmitter of at least 100 kHz is sufficiently high to be able to neglect the effects of double layers and electrolysis. The effect of rapidly moving films on the sensor was also studied. Coney [14] measured no velocity effects at a velocity of 3 m/s, being the fastest obtainable velocity with the used instrumentation. However, Coney [14] stated that the electrical system should be able to generate reproducible results for liquid velocities of up to 25 m/s.

4.3. The electrical circuit

Figure 4.5 shows the designed electrical circuit. An AC-signal source with a specific peak-to-peak voltage V_{pp} is exciting the transmitter. As mentioned in the previous section, it is important to excite the transmitter with at least 100 kHz in order to overrule the double layer effects. With the rotary switch the desired probe sensor pair can be turned on. The signal retrieved at the receiver probe is weakened by the large resistance of the water. This resistance for flush mounted probes and regular tap water is typically around 100 kΩ for small films (<0.2 mm). The weakened signal undergoes two major steps: the amplifier and the rectifier.
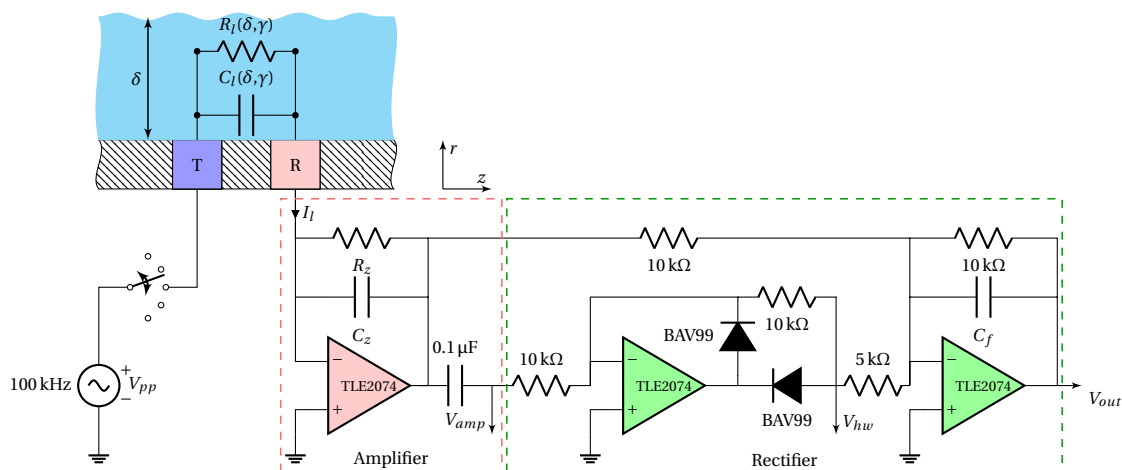
Figure 4.5: The electrical circuit used to find the liquid film height. The red dashed rectangle highlights the amplifier and the green dashed rectangle highlights the rectifier.

The amplifier

As outlined above, the liquid can be seen as a resistor, $R_l(\delta, \gamma)$ and a capacitor $C_l(\delta, \gamma)$ in parallel. The values are a function of the film height and conductivity of the used liquid. This imposed voltage difference induces a certain current, I_l through the liquid, which forms the input signal for the amplifier. An amplifier amplifies, filters and converts this current into a usable high frequency voltage, V_{amp}. This is done by introducing a feedback loop, containing a resistance, R_z for the amplification and C_z for the filtering of high frequency noise, see figure 4.5. Due to the high excitation frequency and the available capacitance of the liquid (C_l), the output of the amplifier has a frequency response with the following transfer function for the system:

$$H(f) = \frac{R_l(\delta, \gamma)}{R_z} \cdot \left(\frac{2\pi f \cdot C_z R_z \cdot j + 1}{2\pi f \cdot C_l(\delta, \gamma) R_l(\delta, \gamma) \cdot j + 1} \right) \tag{4.4}$$

where $H(f)$ is the amplification factor, j is the imaginary number and f the frequency in Hz of the signal. It is desired that the amplification factor H is purely driven by conductance at the given exciting frequency of 100 kHz. This is accomplished when the term, $\frac{R_l(\delta, \gamma)}{R_z}$, dominates and therefore the term between the parentheses in equation 4.4 needs to be equal to 1. This is done by finding a proper combination of R_z and C_z so that

$$f_c = \frac{1}{2\pi \cdot C_z R_z} \gg 100 \, \text{kHz} \tag{4.5}$$

This is called the cut-off frequency, f_c. Beyond that frequency the higher frequency noise on the signal is damped.

A dual powered opamp (TLE2074) is used, which has a bandwidth of 10 MHz and a slew rate of 45 V/μs. This bandwidth and slew rate are sufficiently high to rebuild the signal at these frequencies. The 0.1 μF capacitor works as high pass filter to remove any DC bias induced by the input offset of the opamp.

The rectifier

In order to rebuild the 100 kHz signal, a much higher sampling frequency is necessary. This frequency might be too high for this purpose. Therefore, the high frequency amplified voltage, V_{amp}, is rectified to be able to sample at a lower frequency. In figure 4.6 stage 1, the excitation signal and the output of the amplifier can be seen.

In the rectifier, the first opamp-stage together with two fast switching diodes, is a half-way rectifier. A half-way rectifier only inverts the positive part of V_{amp}, which creates an output signal V_{hw} between the two rectifying opamps, see figure 4.5 and its response is stage 2, see figure 4.6.
The second opamp-stage is an inverting and summing stage (stage 3). When V_{amp} was negative in stage 1, the output is inverted with unity gain, creating a positive output. When V_{amp} was positive in stage 1, the output will be the result of the inverted an unity gain (negative) added to the inverted amplified output of the half-way rectifier ($-2 \cdot V_{hw}$). When the value of the resistors, connected to the second opamp, is a factor two, the output results in a full-wave positive signal, V_{fw}. This output is represented in the orange line in stage 3 of figure 4.6.

A capacitor C_f is introduced, which filters the full-wave signal, V_{fw}, creating a full DC-output, V_{out}. V_{out} can now be sampled with a much lower sample frequency. To be able to choose C_f properly, the frequency of the film dynamics needs to be known, to prevent the filtering of usable film height information. Sawant et al. [39] conducted a thorough study on the behaviour of the liquid film in annular flow for comparable research conditions.
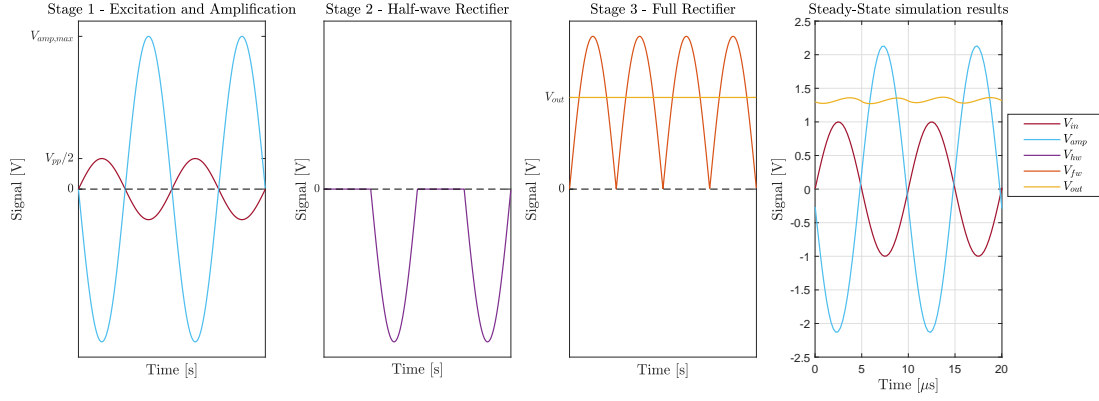
Figure 4.6: Response stages of the rectifier. Left, the input excitation signal and the amplified signal. Centre left, the output of the half-wave rectifier. Centre right, the output of the rectifier in case of a full-wave rectifier (C_f not present) and the result of a full AC/DC converter (C_f present). Right, TINA-TI simulation results for an input of 100kHz and an assumed resistance fraction, $\frac{R_l(\delta,\gamma)}{R_z}$, of 2 and a capacitance fraction $\frac{C_l(\delta,\gamma)}{C_z}$ of $\frac{1}{3}$.

They concluded that a film movement for high gas velocities does not exceed frequencies of 300-500 Hz. In other words, the cut-off frequency of the last filter stage (stage 3) must not be smaller than 500 Hz

$$f_c = \frac{1}{2\pi \cdot 10\,\mathrm{k\Omega} \cdot C_f} \gg 500\,\mathrm{Hz} \tag{4.6}$$

Therefore, the value of C_f is chosen to be 1.8 nF, creating a cut-off frequency of ~ 9 kHz. The response of the considered electrical circuit is simulated in TINA-TI. In this program, the characteristics of the crucial electrical components, such as the opamps and the diodes, are implemented. The electrical impedance of the film is assumed to be 80 kΩ for R_l and 10 pF for C_l and subsequently for the feedback loop 160 kΩ for R_z and 3.3 pF for C_z. The characteristics of the film represent a small film (± 200μm) and are based on experience, see Appendix A.

The simulation results show a complete inverted amplified output V_{amp} with no phase shift compared to V_{in}. This means that the higher capacitance of the liquid does not affect the output. Furthermore, V_{out} is a factor 2 larger than the input voltage. Therefore, the output is dominated by conductance. The rectifier output V_{out} has a value of 1.5 V, which is around the root mean square value of V_{amp}. This is an expected value for an AC-DC conversion. Furthermore, V_{out} shows a small wiggle. Due to the small value of C_f, the low-pass filter is not capable of fully filtering the complete sinusoidal signal. C_f can be chosen larger, but this will reduce the response time. The period of the wiggle is so small as compared to the maximum frequency of the film height dynamics and will therefore be accepted.

The data acquisition unit
The output of the rectifier is sent to a data acquisition unit. A National Instruments USB 6211 is used, which has eight differential 0-10 volt analog input channels and a total maximum sample frequency of 250 kHz for all inputs. Differential measurement is used to generate a more stable and noise-free measurement.

The circuit board
Because high frequencies are used, a printed circuit board is designed using only surface mounted components. This reduce the effect of unwanted inductance and capacitance coupling of the signal.

Furthermore, this makes the signal processing less vulnerable to noise. In figure 4.7 the design is represented and on the right in final result is displayed. The circuit board is capable of the signal processing for four sensors. For the cabling, RG174u coaxial cables are used which resist well against the interference of noise.

(a) PCB receiver design

(b) PCB receiver result
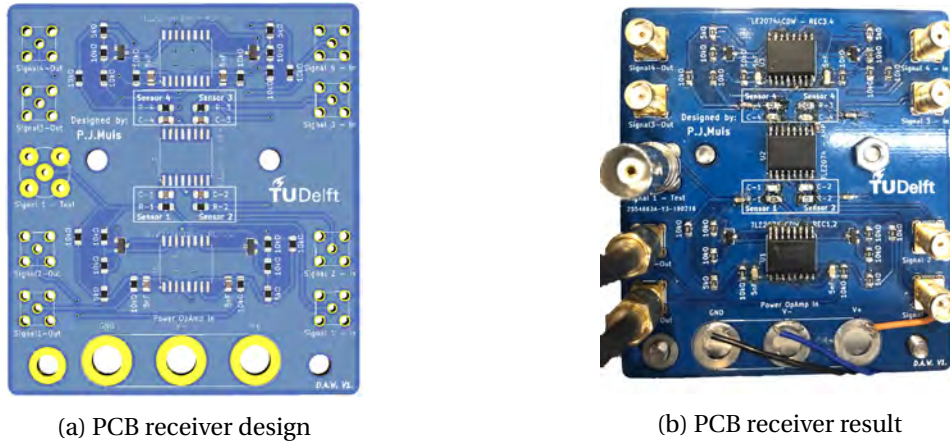
Figure 4.7: The PCB design and the final result.

4.4. Probe dimensions and implementation

The dimensions of the used probes depend on the desired measurement range. For the cause of this study, the film thickness is comparable with the results from Kurian [28]. This means that the expected average film thickness for annular flow in an annulus is in the range of 0 - 1 mm. However, large kinematic disturbance waves are present on top of these films. For low superficial gas velocities, these amplitudes can be twice to tree times the size of the average flow [5, 39]. Therefore, a measurement range of 0 - 2.5 mm is desired.

Sawant et al. [39] used for comparable research conditions ring electrodes with a thickness of 2.54 mm and a probe distance, d_p of 3 mm. These dimensions, together with the proof of concept results in Appendix A, are considered to be suitable for the purpose of this project. However, it is desired to measure the film thickness distribution along the circumference of the inner and outer pipe of the annulus. Therefore, the ring electrodes used by Sawant et al. [39] are replaced with cylindrical flush mounted probe pairs in streamwise direction. In figure 4.8 the frontal view of the probe pair is shown. The probes have a diameter, d_w, of 2.5 mm and are placed 3 mm apart. It is assumed that the film distribution has a symmetry line in the direction of the eccentricity. Therefore, five probe pairs are implemented in half the circumference of both pipes. The right drawing in figure 4.8 shows the cross-sectional view of the tubing with the eccentricity direction, e, *i.e.* the symmetry line.

Simulation

Before the probes are installed, the desired measurement range of 2.5 mm must be verified. This is done using COMSOL. In figure 4.9 the different domains are represented for the different pipes. Each domain has different mesh sizes and material properties, which can be found in table 4.1. In the simulations, the transmitter and receiver boundary surface have an imposed potential of 1 V and 0 V, respectively. The other boundaries have an insulating boundary condition. The signal is calculated by a surface integral of the normal current density on the receiver surface, which returns the current through the receiver. These settings together with the numerical mesh are assumed to be accurate enough to give an impression of the electrical field of the studied geometry. A sensitivity study can be found in Appendix B.
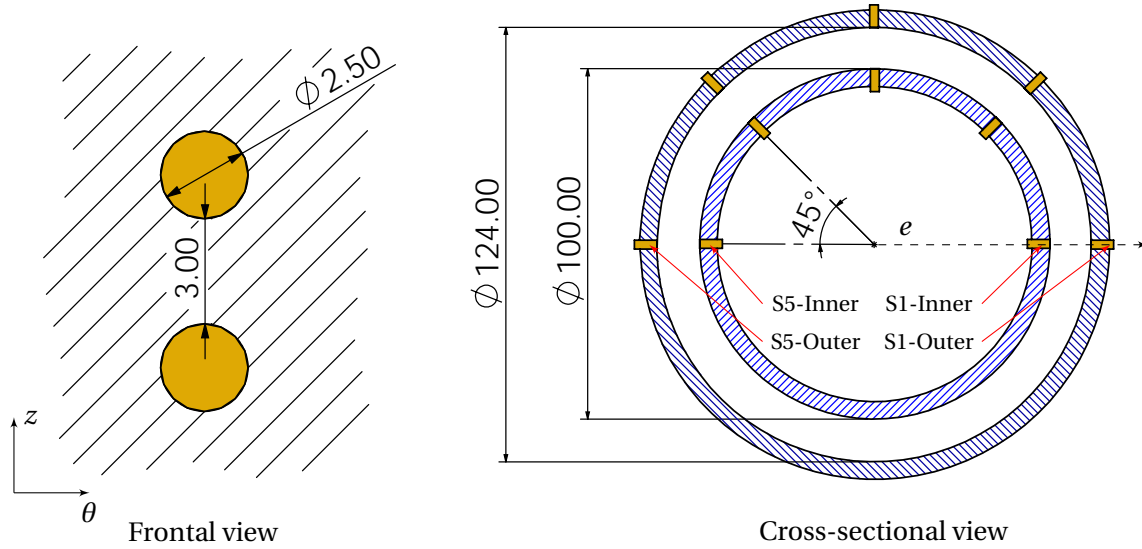
Figure 4.8: Probe orientation in the tubing. Left, the frontal view of a transmitter and receiver pair with the dimensions in the PMMA tubing represented by the hatched area. Right, the cross-sectional view of the five sensors in the 100 mm inner pipe and the five sensors in the outer pipe. The name of the sensor at the top side (side moving towards outer pipe) is called sensor 1 (S1) and increases by one when moving away from the top side. The dimensions are in mm.

Table 4.1: Material and mesh properties used in the COMSOL simulations for the inner and outer pipes.

Domain	Material properties			Inner pipe				Outer pipe			
	Material	γ [μS/m]	ϵ [-]	Mesh size [mm] [Min Max]	Total domain			Mesh size [mm] [Min Max]	Total domain		
					Azimut [°]	Height [-]	No elements [-]		Height [-]	Azimut	No elements [-]
Probe	Brass	Comsol based	1	[0.0375 0.2]				[0.0375 0.2]			
Tube	PMMA	10^{-19}	2.6	[1.34 6.35]	$40°$	$10 \cdot d_p$	$1.86 \cdot 10^5$	[2.05 9.74]	$16\frac{2}{3} \cdot d_p$	$45°$	$1.84 \cdot 10^5$
Liquid	Water	500	80	Swept - $\frac{\delta}{30}$				Swept - $\frac{\delta}{30}$			

Figure 4.10 presents the dimensionless signals of the Coney relation (equation 4.2) and the COMSOL simulations for the considered geometry (figure 4.8) in the inner and outer pipe. The dimensionless signal is the signal divided by the saturation signal; this is a powerful way to compare probe the characteristics. As can be seen, the dimensionless responses for the inner and outer pipe completely overlap, from which it can be assumed that the characteristics are independent of the curvature of the pipe they are mounted on. Furthermore, the Coney and COMSOL results predict a different probe response. This is probably the result of the 2D simplification in Coney's approach. In that approach the probes are modeled as two rectangular strips and thus there is a larger area to receive the signal with. In the simulated geometry the two cylindrical probes have the largest width at the core-to-core distance of the probes when considered in 2D. This is smaller than the constant width in Coney's approach. Therefore, the simulation results and the cylindrical probes have a smaller measurement range.

From the simulations the resistance of the liquid film, R_l, is also extracted, see figure 4.10. Again, for both tubes the resistance is expected to be the same. For a film thickness of 100 μm a resistance of 90 kΩ can be expected and it has an asymptotic behaviour towards 8 kΩ for thicker films.
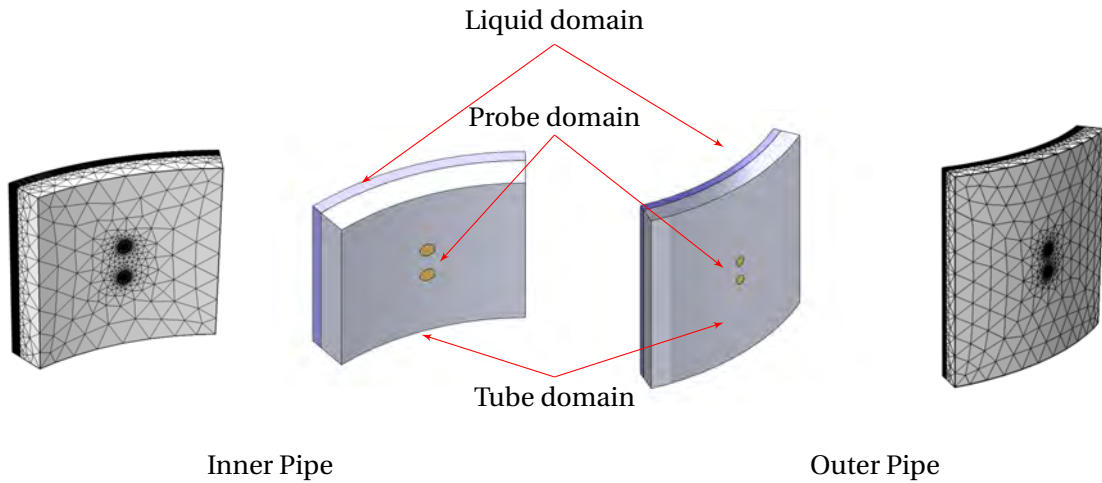
Figure 4.9: Simulation domains and meshes for the inner (left) and outer pipe (right).
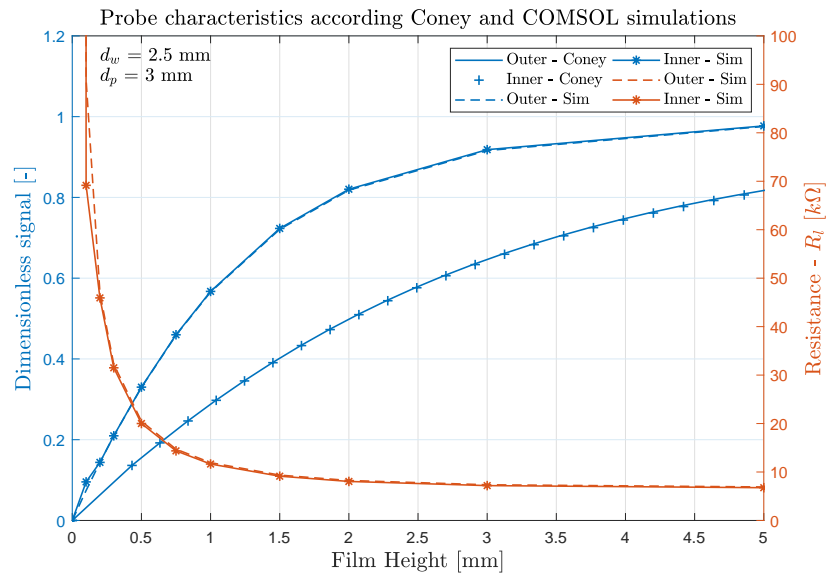
Figure 4.10: Results of Coney's relation, equation 4.2 and the COMSOL simulations for the inner and outer pipes. Both approaches show other responses. With the different approaches, however, the results for the inner and outer pipe entirely overlap. From the simulation the resistance of the liquid film could also be extracted.

Implementation

The probes are implemented in the middle of the 0.3 m section of the inner and outer pipe, respectively, see figure 4.12. The diameter of the probes are manufactured with an accuracy of 2.5%. The mounting holes are made by using a milling machine and its location can deviate by approximately 1°. Every probe is soldered to a laser-cut connection point and is glued into the mounting holes using epoxy glue. The probes are connected with the RG174U coaxial cables. The connection cables of the inner pipe are approximately 9 m and are considerably longer than the 2 m wires for the outer pipe.

In the electrical circuit, a feedback resistance, R_z, of 160 kΩ is chosen, which results in an expected gain of 20 times for the thicker films. The feedback capacitance, C_z, is chosen to be 3.3 pF in order to get a sufficiently high cut-off frequency. These values are chosen, based on the simulation results.
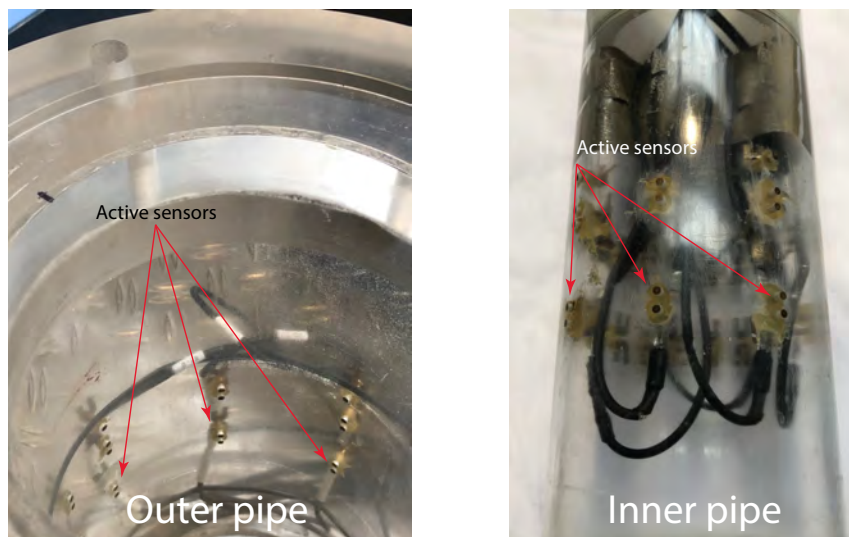
Figure 4.11: Implementation of the sensors in the outer pipe (left) and in the inner pipe (right). The annotated sensors are the visible connected sensors used in the experiments.

4.5. Calibration

The calibration is conducted using seven in-house made calibration cylinders for respectively the inner and the outer pipe, see figure 4.12. Each cylinder is made of PVC and has an accurate diameter imposing a certain film thickness. The dimensions of the cylinders are based on the simulation results shown in figure 4.10. The calibration cylinders for the inner pipe impose a film height of 0.1 mm, 0.4 mm, 0.9 mm, 1.25 mm, constructing the linear part of the curve and 1.65 mm, 2.4 mm 3.9 mm constructing the deflection towards the saturation signal. The calibration cylinders for the outer pipe impose a film height of 0.4 mm, 0.6 mm, 0.8 mm, 1.17 mm for the linear part and again 1.65 mm, 2.4 mm 3.9 mm to find the deflection. These calibration cylinders are manufactured with an accuracy of 5 μm

Due to the geometrical instability of PMMA, each sensor position has a different distance to the calibration cylinder. Therefore, the diameter at each sensor position is accurately measured by using a dial bore gauge.

A 100 kHz AC-signal with a peak-to-peak voltage of 1.5 V is used as the excitation signal for the calibration. The output signal is measured with a sample frequency of 5 kHz for a duration of 10 s. The used liquid during the calibration is tap water at 21.4 °C with a conductance of 500 μS cm^{-1}.

Frequency response

First the frequency response of the system is determined to ensure the signal is dominated by conductance. The amplified signal, V_{amp}, is measured with an oscilloscope. The gain is measured and compared to the simulation results from figure 4.10 using equation 4.4.

Figure 4.13a shows that the measured frequencies reveal a different behaviour than the simulated results. The behaviour for frequencies below 100 kHz is probably induced by the long wires needed to connect the probes in the inner pipe to the electrical circuit. Long cables have a large inductive coupling with the electronic circuit. To prove this hypothesis, a test is conducted with shorter cables for the inner pipe. Figure 4.13a shows that these results correspond much better with the simulated

(a) Inner pipe
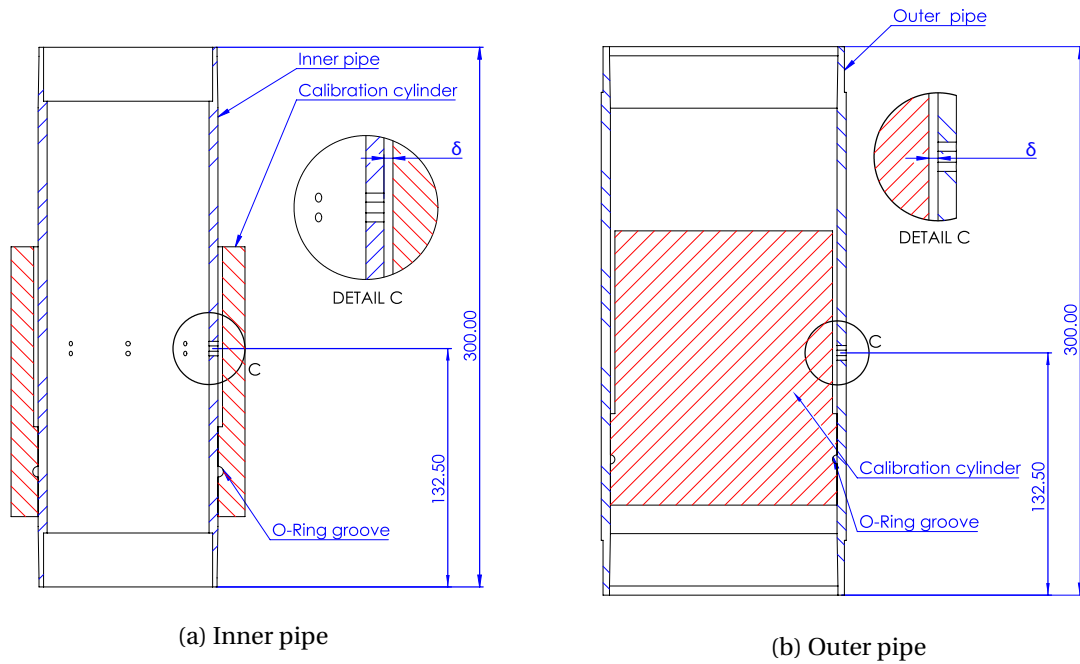
(b) Outer pipe

Figure 4.12: Cross-sectional view of the section in the inner and outer pipe (without flanges) in which the sensors are implemented, together with the calibration cylinders. All dimensions are in mm.

results, which confirms the influence of the long cables on the signal. Although the long cable results for lower frequencies (<50 kHz) deviate much from the simulation results and from the shorter cable results, the amplification factor is relatively comparable for the required frequency of 100 kHz. It is therefore assumed that conductance is dominant at this frequency, implying that the inductive influence of the longer cables can be neglected.

Figure 4.13b shows that the amplification for the outer pipe is stable for frequencies below 100 kHz. The amplification is decreasing for frequencies above 100 kHz. Therefore, when measuring at the required 100 kHz, the signal is still dominated by conductance. However, the amplification factor is less than expected. This means that the resistance of the liquid as predicted by the simulations is lower than the actual value. For example, for a film thickness of 0.8 mm at the outer pipe, the simulated resistance is 14.7 kΩ compared to the actual resistance of 18.5 kΩ.

Film height response
The most important calibration curve is the film height response for the ten sensors. The sensors in the inner pipe and outer pipe are calibrated 4 times and 6 times, respectively, in order to get a reliable curve. Figure 4.14 shows the dimensionless calibration curves for sensor 1 and 2 in both pipes, together with the spline fit and the simulation result. As shown, the standard deviation between the different calibration runs is generally larger in the smaller film height regions (<1 mm) compared to the larger films. In the smaller film height regions, the sensors are more sensitive to the position of the calibration cylinders. When these are not placed fully parallel to the pipe, a slight off-set can cause a large deviation in the signal. The characteristics of the sensor 1 and 2 for both pipes are very similar, which is expected because of the same geometrical dimensions. This is also the case for the other sensors.

(a) Frequency response - Inner Pipe   (b) Frequency response - Outer pipe
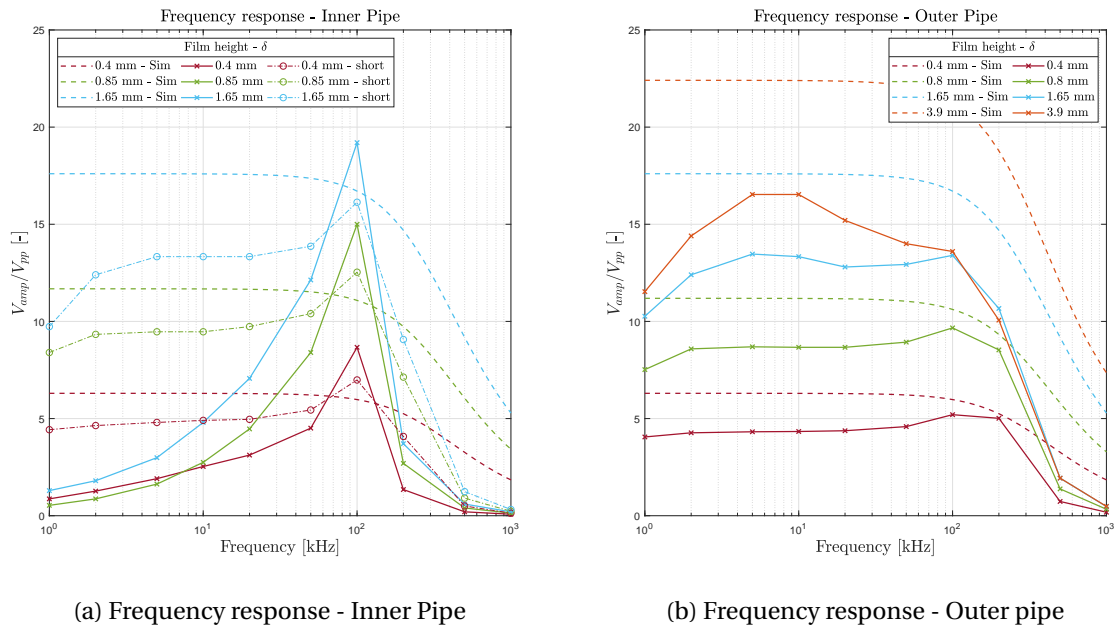
Figure 4.13: Bode plots for the inner and outer pipe. The sensor 1 (S1) results for both pipes are presented. The dashed lines are the results from the simulation for comparable film heights. In figure 4.13a also a result with shorter connection cables is displayed.

When the calibration curves are compared to the simulation results, one can conclude that the deviation is relatively large. Probably the long cables transmitter and receiver cables influence the signal. This might also be the reason why the measurement range for the inner pipe differs from the results for the outer pipe. Proof of this hypothesis cannot be given.

Temperature response
As discussed, the resistance of the liquid also depends on the conductivity, γ. The conductivity itself depends on the concentration of dissolved ions and the temperature. In Appendix A, it was concluded that the temperature has a more dominant effect than the concentration effects due to evaporation.

The previous calibrations were conducted using normal tap water having a temperature of 21.4 °C. However, in the flow loop experiments, the high gas velocity causes a slight cool-down of the liquid film. The signals are measured at very thick liquid films of approximately 50 mm to ensure that the signal is fully saturated at multiple temperatures, giving a temperature response. This temperature response shows the dimensionless signal as function of the temperature, see figure 4.15. The value 1 corresponds to the calibration temperature of 21.4 °C.

As can be seen in figure 4.15, a linear relation exists, especially for the temperature for the outer pipe. For the inner pipe a small scatter can be seen. However, from experience (see Appendix A) it is known that there exists a linear relation.Therefore, a linear fitting routine in Matlab is used to find the sensitivity of each sensor on the temperature difference with respect to the reference value of 21.4 °C. This makes it more convenient to later find the correct film height as function of the signal and temperature.
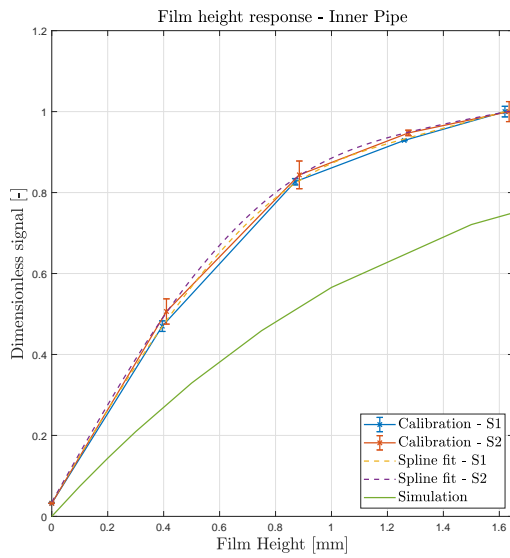
(a) Film height response - Inner pipe
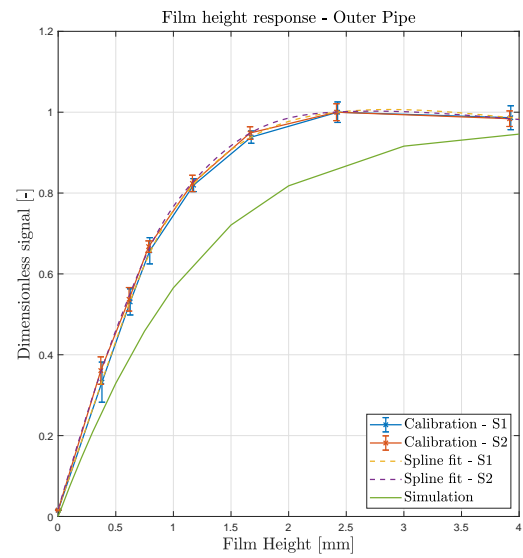
(b) Film height response - Outer pipe

Figure 4.14: The film height calibration with the standard deviation, the spline fit and the simulation result. For a better overview, only the results for sensor 1 and 2 (S1-S2) at both pipes are shown.
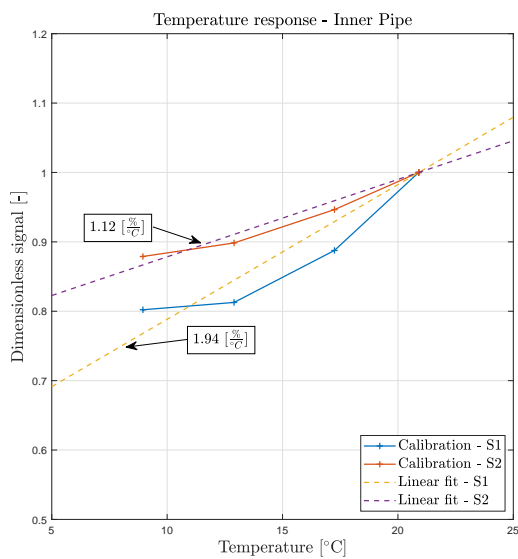
(a) Temperature response - Inner pipe
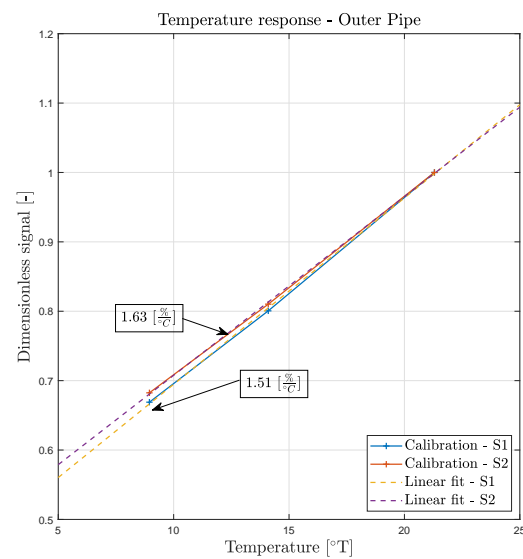
(b) Temperature response - Outer pipe

Figure 4.15: The dimensionless signal of sensor 1 and 2 for a film height of 2.4 mm against the temperature of the water together with its sensitivity. The signal is made dimensionless with the signal at 21.4 °C.

5

Concentric annulus

This Chapter describes the results of the concentric annulus experiments. The main objective of these experiments is to determine the flow characteristics for a concentric annulus configuration, which includes the pressure gradient in axial flow direction, variation in the amount of the applied liquid (u_{sl}) and dependency on liquid distribution, as a function of the superficial gas velocity (u_{sg}). Three TPCs are obtained for a u_{sl} of respectively 20 mm/s, 10 mm/s and 5 mm/s, where the liquid is equally divided between the inner and the outer pipes ($f_{in} - 0.5$). In the other TPCs, the liquid is either fully injected on the outer pipe, ($f_{in} = 0$) or on the inner pipe ($f_{in} = 1$) for u_{sl} values of respectively 20 mm/s, 10 mm/s, 5 mm/s and 3 mm/s. This is done to study possible redistribution effects. The results for equal and single wall liquid injection will be subdivided into the following discussion subjects:

1. The pressure drop along the tubing together with the liquid hold-up.

2. The film distribution on the inner and outer pipe.

3. The onset of liquid loading .

4. The characteristics of the disturbance waves.

All measurements are considered to be the initial results from a newly designed and constructed annulus facility. Therefore, most of the subjects will first cover a validation of the used sensors and measurement techniques. The general conclusion of the film height sensors will be discussed in the last paragraph of this Chapter.

5.1. Pressure drop and liquid hold-up
This section will discuss the pressure drop and liquid hold-up, α_l, for equal and single wall liquid injection in a concentric annulus. First, the applied film sensors and measurements techniques will be discussed, in order to validate the data with respect to the general obtained results.

Set-up validation
The pressure drop has been determined by using six pressure sensors, positioned at six different locations in axial flow direction. The pressure at each sensor is measured for 30 s. The time-averaged values of the pressure signal are determined, and these values are collected in a graph, showing the pressure versus the location. A linear curve is fitted to these 6 data points. The slope of the fitted line is considered to correspond with the mean pressure drop.

This can only be done when the flow between the pressure sensors is fully developed. This means that the six measured pressures need to have a linear relation and more importantly, the fluctuation of each of the six signals need to be of the same order of magnitude. In figure 5.1a the relative pressure is shown at the different axial locations for different combinations of u_{sg} and u_{sl} values. The standard deviation at lower gas velocities is higher due to the slug behaviour, which causes large pressure fluctuations. Furthermore, the pressure does not fully reach atmospheric conditions at the outlet. For larger gas velocities, a slightly higher pressure is building-up at the outlet, compared to the low gas velocities. However, because for every liquid gas and liquid throughput a clear linear relation can be observed and the pressure fluctuations of the different sensors, are all of the same order of magnitude for identical gas and liquid velocity, the flow can be considered fully developed. Therefore, the applied approach is considered to be sufficient in order to determine the relevant pressure characteristics.
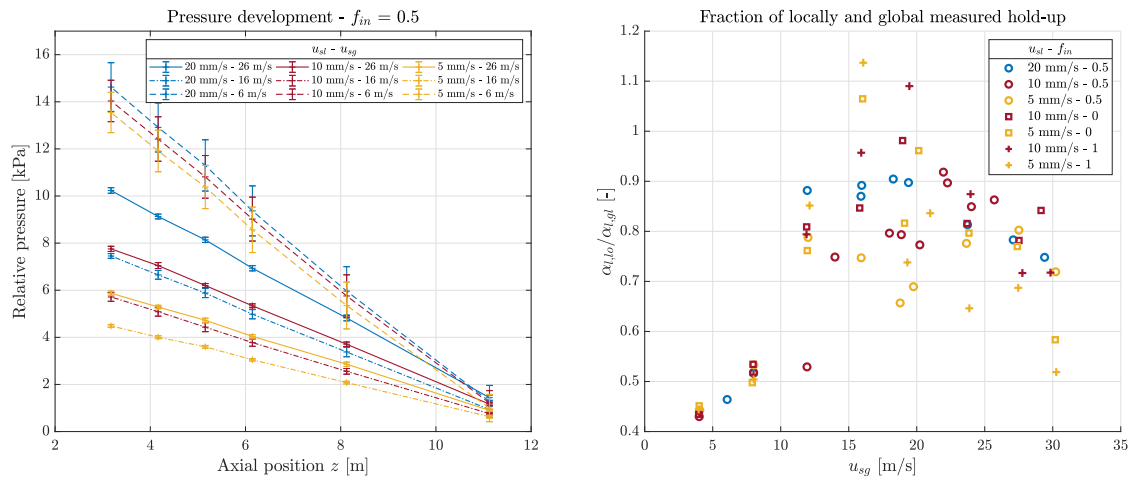
(a) Relative pressure at the six pressure sensors, together with the standard deviation for different u_{sg} and u_{sl}. The presented results are for equal liquid injection, f_{in} = 0.5.

(b) Ratio of local liquid hold-up fraction and the global liquid hold-up fraction for different u_{sg} for all concentric measurements.

Figure 5.1: Set-up validation for the pressure development and liquid hold-up.

Chapter 3 already discussed the global liquid hold-up $\alpha_{l,gl}$, which can be measured by weighting the liquid amount in the set-up after the experiment. The global hold-up is measured five minutes after the experiment has been completed, which is assumed to be enough time to drain all the liquid from the 12 m set-up. This technique is reliable since all liquid in the system is measured and averaged over the complete volume of the pipe.

The alternative method is to measure the liquid hold-up using the film height sensors. Every sensor is independently excited for ten seconds and the output signal is sampled with a frequency of 5 kHz. The local hold-up, $\alpha_{l,lo}$, is found by averaging the film height retrieved from the 5 sensors at each pipe. This technique is much more sensitive to *e.g.* the spectral resolution, the location of the sensors, and the local wetting properties of the pipe.

Figure 5.1b shows the difference between the local liquid hold-up with respect to the global liquid hold-up. It can be seen that the measured local liquid hold-up is 10-25% lower for higher gas-velocities (u_{sg} >14). This deviation can be explained by the following factors:

- In the global hold-up measurements, the development of the liquid film is also included. The liquid is injected through holes with a diameter of 2 mm, perpendicular to the gas flow. The gas needs to change the direction of the liquid flow, which causes liquid accumulation and initially a thicker liquid film at the inlet. Subsequently, the liquid flow is spread out as it accelerates.

- The local pressure is lower downstream in the tubing, causing a slightly higher gas velocity as compared to the point of injection. This induces locally a higher interfacial friction, which effectively reduces the film height.

- The wetting characteristics of the tubing are strongly dependent on the location of the pipe. During the initial experiments, the wetting conditions of the pipe were not yet ideal. Newly fabricated PMMA tubes have a low initial surface roughness, resulting in dry spots at a combination of lower liquid throughputs and high superficial gas velocities (u_{sg} > 20 m/s). When one or more sensors are located at a dry spot, the averaged local film thickness was also reduced. After several experiments, the surface roughness of the pipes increased improving the wetting conditions.

- At higher liquid throughputs, some liquid entrainment in the gas flow can be present due to the thicker film. The liquid entrainment is not included in the local measurement with the film sensors, but is included in the global hold-up fraction measurement.

- At higher superficial gas velocities, the wave length of the ripple waves is decreased. When the length of the ripple waves is no longer large compared to the distance between the sensors, the film height sensors tend to underpredict the mean film height. This was also shown in figure 4.4. A possible underestimation of up to 30% between global and local liquid hold-up measurements was already reported by Hewitt and Hall-Taylor [20], due to the presence of ripple waves.

The deviation is very large for the lower gas velocities (u_{sg} < 14 m/s). A possible reason for this is the large amount of gas enclosed as bubbles in the liquid film, which reduces the conductance and thus the retrieved signal. For these velocities it is presumed that the sensors do not return a reliable signal.

The ratio between the local and the global hold-up fraction, shown in figure 5.1b, together with the above mentioned arguments indicate that the film sensors give a good estimation of the local film height.

Equal liquid injection
The measurement results for the pressure drop and liquid hold-up fraction for equal liquid injection along the inner and the outer pipe (f_{in} =0.5) can be found in figure 5.2 and figure 5.3, respectively. Figure 5.2 indicates that for u_{sg} lower than 6 m/s, all the TPCs are converging to the same pressure drop. For these u_{sg}, the flow is predominantly in the churn flow regime. In this case, the hydrostatic forces are dominant as the gas velocity is too low to fully drag the liquid upward. As a result, liquid will accumulate in the system. Therefore, the amount of liquid in the set-up for the different superficial liquid velocities should be comparable. This can be verified by consulting the global liquid hold-up results in figure 5.3. The global hold-up values, represented by the circles, completely overlap for the low superficial gas velocities.
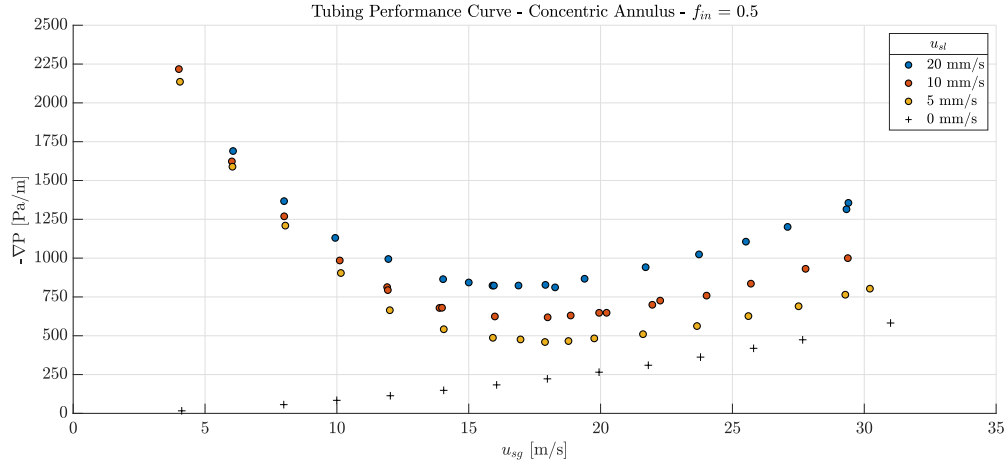
Figure 5.2: Tubing performance curves for different u_{sl} with equal liquid injection for the inner and outer pipes ($f_{in} = 0.5$) in the concentric annulus.
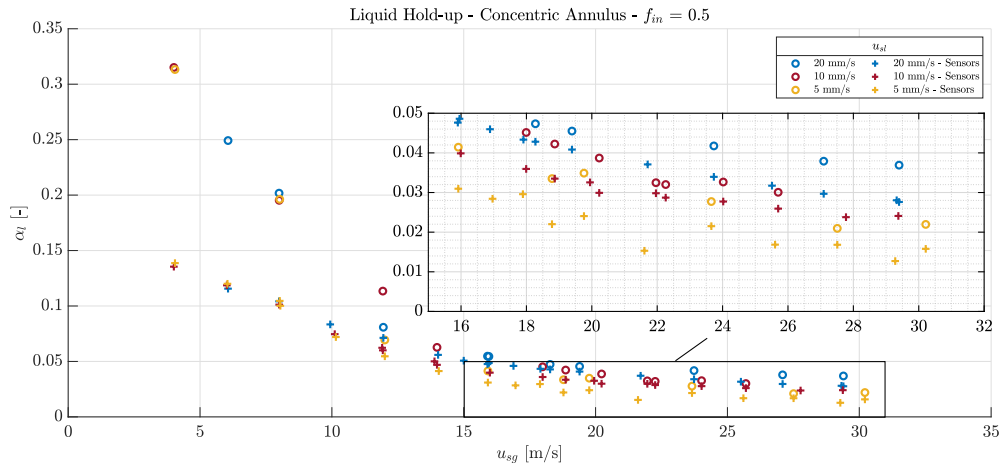
Figure 5.3: Liquid hold-up fractions for different u_{sl}, with equal liquid injection for the inner and outer pipe ($f_{in} = 0.5$) in a concentric annulus. The global liquid hold-up fractions, $\alpha_{l,gl}$, are represented by the circles and the local liquid hold-up fractions, $\alpha_{l,lo}$, measured using the sensors, are represented by the crosses.

When increasing the superficial gas velocity, the pressure drop for the different curves, is increasingly deviating until a certain minimum pressure drop is reached, see figure 5.2. For all liquid throughputs this minimum pressure drop corresponds with roughly a superficial gas velocity equal to 17.5 m/s. At this point the hydrostatic pressure drop is in equilibrium with the frictional pressure drop. In figure 5.3 it can be seen, that this minimum is characterised by a gradient change for the global liquid hold-up, from a u_{sg} of 17.5 m/s.

For gas throughputs higher than the pressure drop minimum, the frictional pressure drop is dominant. The trend of the curve is similar to the single phase pressure drop, represented by the black crosses in figure 5.2. The slope of the pressure drop related to the superficial gas velocity is mainly due to the larger liquid hold-up in the system. A larger hold-up fraction corresponds to a thicker and wavy liquid film interface and subsequently also to a higher interfacial stress. A more extensive study will be conducted in section 5.4. In figure 5.3, it can be seen that the local and global hold-up fractions curves show a similar trend for an increased superficial gas velocity, but the absolute val-

ues are slightly lower as discussed in the previous section.

When the TPCs for the different liquid throughputs in figure 5.2 are compared with the results reported by Kurian [28], a structural higher pressure drop of 20% for the annular regime in the latter study is found. The possible reason for this deviation, is the used annulus geometry. Kurian [28] used an annulus with a hydraulic diameter of 20 mm, whereas for the current study a hydraulic diameter of 24 mm is used. The pressure drop for the annular regime, scales inversely with the gap size in the annulus ($\nabla_z P \sim 1/D_h$), which explains the higher pressure drop in the results provided by Kurian [28]. The global hold-up fractions are found to be similar to the the results presented in the current study.

Liquid injection on single pipe wall
This section discusses the results for the distribution of the injected liquid only on the inner ($f_{in} = 1$) or on the outer pipe wall ($f_{in} = 0$). For the global liquid hold-up measurements only the u_{sl} 10 mm/s and 5 mm/s are conducted.
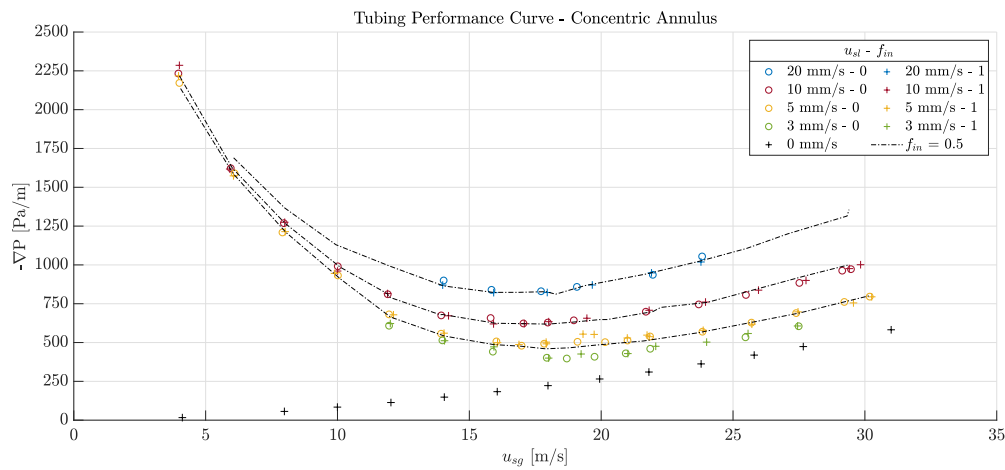
Figure 5.4: Tubing performance curves for different u_{sl} with liquid injection either on the inner or the outer pipe wall. The equal injection results are represented by the black curves.
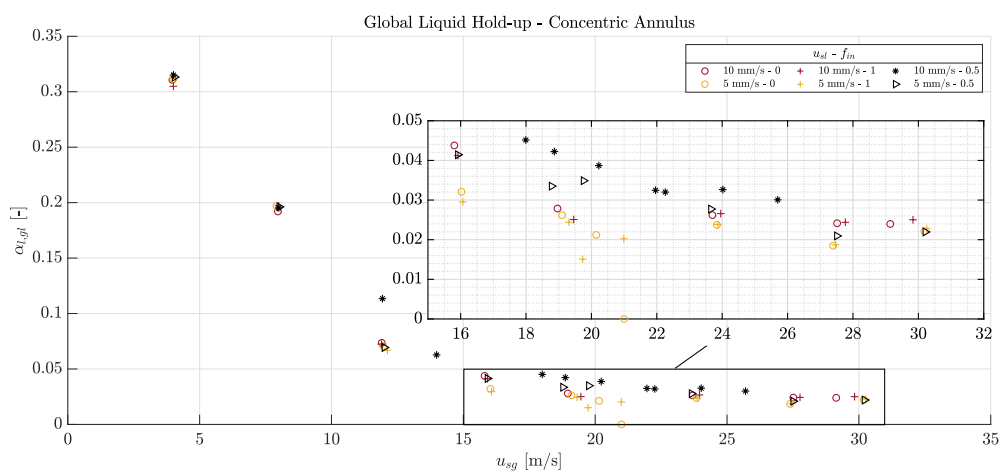
Figure 5.5: Global liquid hold-up for different u_{sl}, with liquid injection either on the inner or the outer pipe wall.

The results for the pressure drop can be found in figure 5.4 and the global and local liquid hold-up fractions can be found in figure 5.5 and figure 5.6, respectively. Based upon these pressure drop results, it can be concluded that the TPCs of the different throughputs are not affected by the way of liquid injection. When the results are compared with the equal liquid injection, represented by the black dashed line in figure 5.4, the same conclusion can be drawn. The liquid hold-up for $f_{in} = 1$ and $f_{in} = 0$ are also highly comparable for the global as well as for the local hold-up measurements, see figure 5.5 and figure 5.5. However, when both the liquid hold-up fractions are compared with the results of the equal injection, represented by the black symbols in both figure 5.5 and figure 5.6, it can be seen that the liquid hold-up fractions are slightly lower. Since the pressure drop is comparable for the equal pipe and single pipe injection methods, see figure 5.4, a larger interfacial friction is expected for the single wall injection cases. This hypothesis is validated by a more detailed study on the gas-liquid interface, which is described in section 5.4.
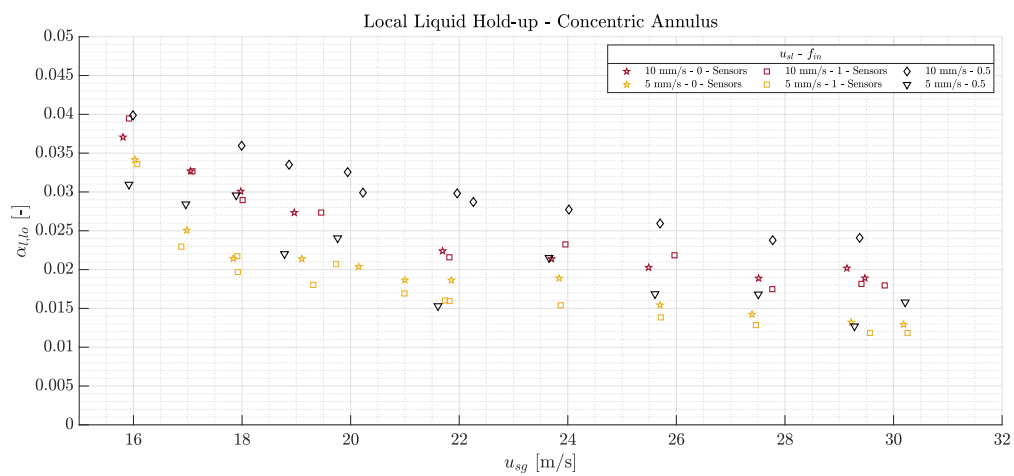
Figure 5.6: Local liquid hold-up for different u_{sl}, with liquid injection either on the inner or the outer pipe wall.

At the point where the pressure drop is at its minimum (u_{sg} of 19 m/s), a jump in the pressure drop is observed for the case where all liquid is injected on the inner pipe wall ($f_{in} = 1$) for u_{sl} is 5 mm/s, see figure 5.4. Nevertheless, the difference between the global liquid hold-up fraction is negligible as indicated by the yellow circle and cross at u_{sg} 19 m/s, in figure 5.5. Also in the accompanying curve for the local liquid hold-up fraction in figure 5.6, no outliers are observed.

Figure 5.7 shows the flow visualisation for different u_{sl} at a u_{sg} of 20 m/s. For u_{sg} is 3 mm/s, the outer pipe is considered to be dry. When increasing u_{sl} more liquid will stick at the outer pipe in the form of droplets. Eventually, at a u_{sl} of 20 mm/s, the outer pipe is fully wetted. A possible explanation for the jump in the pressure drop in the 5 mm/s curve at a u_{sg} value of 19 m/s can be the additional roughness due to the droplets. The amount of droplets does not affect the 10 mm/s and 20 mm/s curves because the overall pressure drop is higher and thus the result is less sensitive to the additional roughness.

The results for the single pipe injection provided by Kurian [28] show a different behaviour for the pressure drop. While in the current study, a comparable pressure drop is found for equal pipe and single pipe injection, the results of Kurian [28] show a slightly lower pressure drop of about 10% for single pipe injection. The results provided by the current study and Kurian [28] show comparable results for the global hold-up.
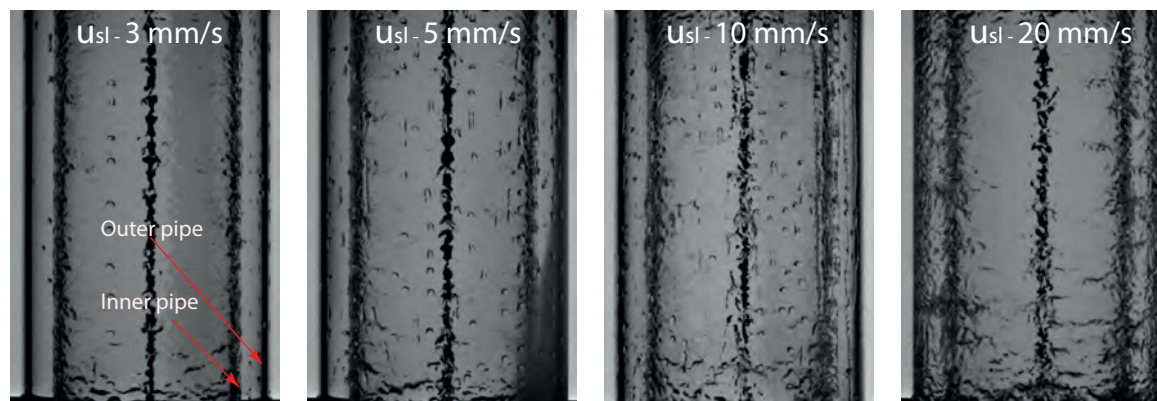
Figure 5.7: Flow visualisation for $u_{sg} = 20$ m/s, $f_{in} = 1$ and different superficial liquid velocities.

5.2. Film height fraction

In Chapter 2, it was mentioned that there is still a lack of empirical data on the liquid films along the inner and outer pipe. Therefore, in many models, an equally thick film is assumed. This section involves an assessment whether this assumption is justifiable. Furthermore, this section tries, as matter of exploration to obtain more knowledge on the liquid hold-up fraction and its dependence on the gas and liquid throughput.

In the set-up, the liquid hold-up fraction can be determined in two ways. The first method is using the conductance probes on the inner and outer pipe. In figure 5.9a, the film height fraction for equal and single wall injection, based on the cross sectional area occupied by the liquid, A_l, can be found. Because the film heights are much smaller compared to the diameter, the cross sectional area can be linearized; a cross sectional area fraction of 0.45 corresponds to an equal film height at the inner and outer pipe, see the dashed line in figure 5.9a. Considering the cross sectional area instead of the film height fraction, these results can be better compared with the fraction of the volumetric throughputs, which is obtained using the next method.

For the second method, the inner and outer films are separated at the outlet and the liquid collected at separate scales. When the flow is developed, the weight increase on both scales is measured for 30 seconds. From this measurement the global volume flow on the inner pipe, $\dot{V}_{l,i}$, and on the outer pipe, $\dot{V}_{l,o}$, can be determined. The results are shown in figure 5.9b. The results in figures 5.9a and 5.9b will more thoroughly discussed later in this section.

The results obtained by the two measurements methods are not directly comparable, as the determined volume flow from the separator is, among others, a function of the liquid film velocity. When assuming a similar liquid film velocity on the inner and outer wall, both curves can still be qualitatively discussed.

Set-up validation

First, the characteristics of the separator are validated. In figure 5.7, the visual representation for different u_{sl} at a u_{sg} of 20 m/s can be found when all the liquid is injected at the inner pipe. The far left photograph shows a complete dry outer pipe at a u_{sl} of 3 mm/s. Therefore, it is allowed to assume that all the liquid stays at inner pipe.

In figure 5.8, the results for the volume flow at a u_{sl} of 3 mm/s and increasing u_{sg} are represented. At low gas rates, all the liquid will exit the annulus from the outer pipe. This is not expected, since the flow is nearly in the churn regime, which makes the flow rather chaotic. The unexpected behaviour is probably caused by the dimensions of the splitter, see figure 3.3. The film collector for the outer film is reached in a much earlier stage compared to the collector for the inner pipe. When the flow has a low velocity, the flow will probably have the tendency to leave the annulus at the nearest possible exit where the pressure is low.

When the gas rate is increased, the velocity of the liquid is increased and subsequently more liquid will reach the inner film collector. At a u_{sg} of 16 m/s, the volume flow is nearly equal. This is the point where the separator is fully operational. At a u_{sg} equal to 26 m/s, the complete flow is collected at the inner film collector. When the volumetric flow rate is calculated for the u_{sg} equal to 26 m/s case in figure 5.8, it corresponds to the u_{sl} of 3 mm/s.
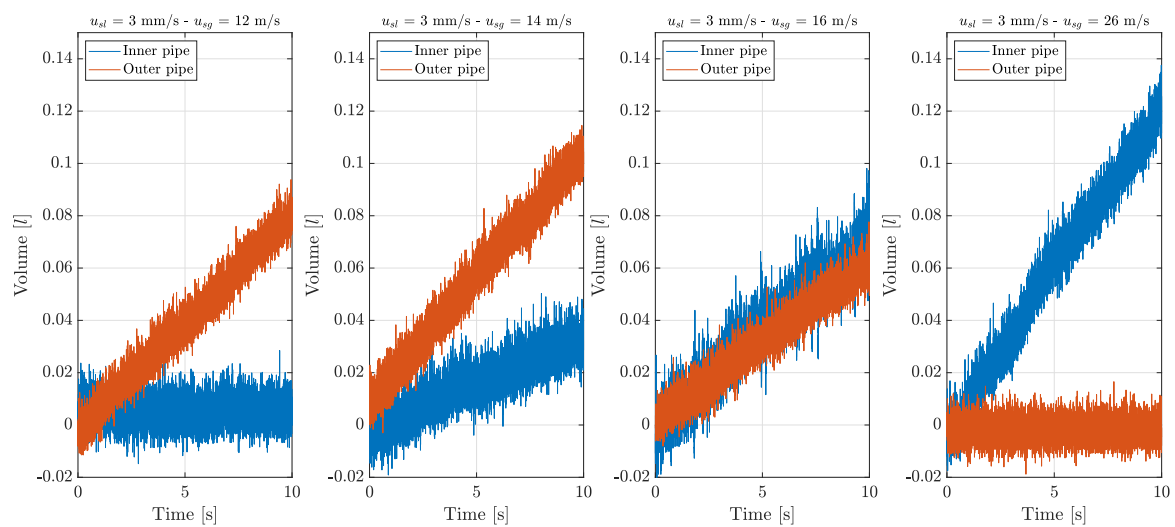
Figure 5.8: Volume throughput development for different u_{sg}. All results are taken for a u_{sl} equal to 3 mm/s.

Equal liquid injection

The filled dots and rectangles in figures 5.9a and 5.9b represent the film height ratio and the volume throughput ratio, respectively, for equal liquid injection. It seems that for superficial gas velocities between 12 - 14 m/s, the liquid height is slightly thicker at the outer pipe based on the results obtained with the local measurement. This can only be claimed when the amount of gas enclosed in the churn flow regime is assumed to be equal at the inner and outer pipe. For larger velocities, a redistribution takes place. For the volumetric throughput ratio in figure 5.9b, the results for lower gas velocities ($u_{sg} < 16$) are not representative as just discussed.

At a u_{sl} of 5 mm/s and gas velocities larger than 15 m/s, the equilibrium quickly shifts towards the inner pipe. For the local film height ratio a large scatter between 0.5 and 0.7 can be seen. This is probably due to dry spots at the outer pipe created when operating at high superficial gas velocities. When the dry spots are located exactly at one of the film height sensors, it lowers the average measured film height for that pipe. These dry spots were also visually observed.

When the superficial liquid velocity is increased to 10 mm/s, less dry spots are observed and a better trend can be distinguished. For the higher gas velocities, the film height seems to be slightly larger at
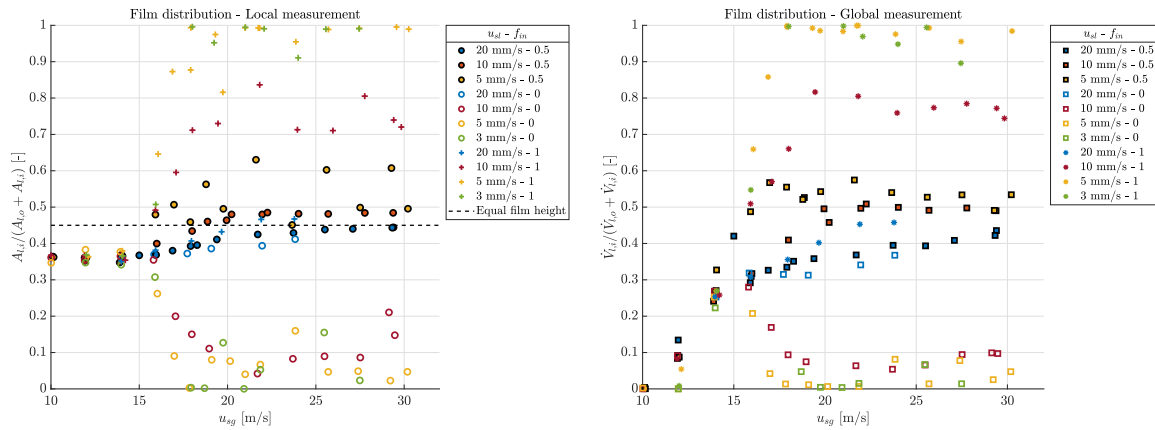
(a) Film height ratio, based on the cross sectional area occupied with liquid at the inner pipe and outer pipe. Results are obtained with the film height sensors. The black dashed line corresponds to an equal film height.The value for equal film height is put at 0.45, since the diameter ratio is included in the calculation of the area.

(b) Global liquid volume ratio between inner and outer pipe, measured using the separator at the outlet.

Figure 5.9: Result for the ratio of the film heights and the global liquid volumes at the inner and outer pipe.

the inner pipe. These observations are similar to the observations by Arai et al. [5]. However, the volumetric flow ratio, in figure 5.9b, is equal at these gas velocities, which would mean that the velocity of the film at the inner pipe is lower than the film velocity of the outer pipe. The results indicate a characteristic trend, nevertheless, the difference is in the order of the accuracy of the measurement method.

At a u_{sl} of 20 mm/s, most liquid transport will be along the outer pipe, which can be seen in figure 5.9b. The film height at the outer pipe is slightly larger and slowly increases to an equal film height. As discussed a thicker film is accompanied by larger waves. It is assumed that from these thicker waves it is easier for the gas to atomize droplets, which have a higher probability to deposit on the outer wall [11]. This process is increased at the inlet, where the thick film needs to be accelerated and possibly induces partial liquid dispersion.

Liquid injection on single pipe wall
In both figures 5.9a and 5.9b, it can be seen that for superficial gas velocities larger than 16 m/s and lower liquid throughputs (u_{sl} equal to 3 mm/s and 5 mm/s), the liquid tends to stay on the pipe at which it is applied. This is also confirmed using the visual observation in figure 5.7.

When the superficial liquid velocity is increased to 10 mm/s, a higher gas throughput is needed to keep the film on the pipe on which it is injected. However, still some liquid is able to transfer to the other pipe. Two possible causes can be formulated:

- Thicker films are present due to the higher liquid throughput, see figure 5.5, which have a wavier interface. From this wavy interface it is easier to atomize droplets. These droplets can subsequently deposit on the other pipe. It is assumed that this effect mainly occurs when the liquid film is accelerating at the inlet.

- The thicker films are more affected by the eccentricity rods, which keep the inner pipe in position. Along these rods liquid can be transported towards the other pipe.

When the liquid is applied on the inner pipe, the liquid film and volume ratio is 80% for the inner pipe at a u_{sl} of 10 mm/s and superficial gas velocities larger than 20 m/s. On the contrary, when all the liquid is applied on the outer pipe, the film height and volumetric fraction on the outer pipe is 90%. This can again indicate that the liquid redistribution is easier from the inner pipe towards the outer pipe than vice versa.

Earlier in this Chapter, it was stated that the hold-up for single pipe liquid injection is slightly lower compared to the equal liquid injection, see figure 5.5. The above mentioned results might be able to provide an explanation. For example, for a u_{sl} equal to 5 mm/s and single wall injection, the film height fraction and the volumetric fraction confirm that nearly all the liquid is transported at either the inner or outer wall for high superficial gas velocities. When a velocity profile of the liquid film such as shown in figure 2.3 is considered, a slightly thicker liquid film on one pipe is able to transport more liquid compared to the case when this liquid film is equally divided over two pipes. For both equal and single wall liquid injection, the same amount of liquid needs to be transported upward. This means that the film heights in the equal injection case need to be larger and therefore the hold-up is larger.

At a superficial liquid velocity of 20 mm/s and single wall inflow, the film height is much larger compared to the 10 mm/s and 5 mm/s film. This thicker film is again accompanied with a wavy interface on the inner or outer pipe. From this wavy interface it is easier for the gas to atomize droplets from the film. This explains why nearly all liquid which is injected on either the inner pipe or outer pipe, tends to redistribute until a stable flow on both pipes is achieved.

In the section 5.1, it was stated that the local film height sensors can provide a good indication of the film height. When the local film height ratio is compared with the global liquid volume ratio, it can be seen that for all cases the same trend is observed, which strengthens the above mentioned statement.

5.3. Onset of liquid loading

In Chapter 2 different relations for the liquid loading and the corresponding gas velocity were given. In this section, the measured onset of liquid loading will be discussed and compared with the relations. The onset of liquid loading is related to the flow reversal of the liquid. The installed capacitance sensor, below the liquid inlet of the outer pipe, returns an amplified signal when liquid is flowing in between the electrodes of the sensors. When the flow is developed, the returned signal is measured for 30 seconds and is subsequently averaged.

Figure 5.10 shows the results for equal and separate liquid injection, at different superficial liquid velocities. A value of 1 corresponds with a total wetted area in between the electrodes and thus indicates flow reversal.

In figure 5.10 it can be seen that when the u_{sg} is decreased below 17 m/s the curves start to deviate when compared to the higher u_{sg} values. This means that the sensor is partially wetted. Generally, the deviation is higher for higher liquid throughputs. An explanation can be that there is a larger amount of droplet entrainment for the higher u_{sl} values, which causes a partially larger wetted area compared to the lower u_{sl} values. However, the fact that the signal is higher does not necessarily mean full flow reversal. When the gas velocity is further decreased from 14 m/s to 12 m/s, the process of flow reversal starts. No proper distinction can be made on whether this point is a function of either the single wall or the equal liquid injection method on the liquid throughput.
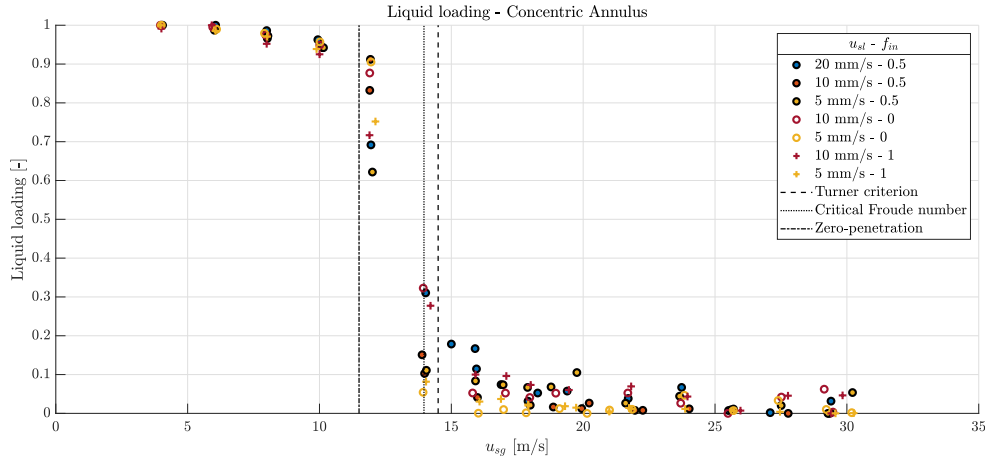
Figure 5.10: Onset of liquid loading for equal and separate injection at different u_{sl}.

Figure 5.10 also includes the onset of liquid loading according the Turner criterion (equation 2.13), the critical Froude number (equation 2.14) and the zero-penetration relation (equation 2.16). It can be seen that the critical Froude number is the most accurate approach to predict the onset of liquid loading for all cases.

5.4. Disturbance waves

In many models, the same interfacial friction factor is used for the gas core and the liquid film at the inner or outer liquid film. As discussed, the interfacial friction is dominated by large waves on the liquid film. In this Chapter, it was occasionally stated that thicker films are also accompanied with a larger frictional factor and therefore larger waves. In this section, a study is conducted on the energy contained by these waves, which is assumed to be a dominant measure for the interfacial friction between the gas and liquid. This is done in order to find whether the above mentioned statements are justified.

Azzopardi [6] concluded that converting the film height signal into a energy spectrum, is the most objective approach to find the disturbance waves. Namely, it is assumed that disturbance waves have a much higher energy at much lower frequencies compared to ripple waves.
The two-sided energy spectrum can be found as follows

$$S_{xx}(f) = |\hat{\delta_n}^2(f)| \qquad\qquad \hat{\delta_n}(f) = \int_{\infty}^{-\infty} e^{-2\pi i f t} \cdot \delta_n(t) dt \qquad (5.1)$$

where S_{xx} is the energy spectrum as a function of the frequency. For reasons of convenience, the two-sided energy spectrum is often multiplied by two in order to be construct a one-sided energy spectrum and so preserve the energy.

The results for three different superficial gas velocities and a u_{sl} value of 10 mm/s, can be found in figure 5.11. It can be seen that for higher gas velocities, the the overall film height decreases and the structures of the interface become more regular. The accompanying energy spectrum shows the frequency and the energy out of which the interface is built up. It is assumed that the disturbance waves correspond to the energy peak in the energy spectrum [5, 39]. To remove the high energy and non fluctuating base height of the film, the power spectrum is studied from 3 Hz.

From figure 5.11 it can be concluded that for most cases the film height and disturbance properties at sensor 1 are more dominant. This was also visually observed for lower liquid velocities, where the dry-out mostly occurred at sensor 5, 4, and 3.

The mean energy for every u_{sg} value is found by averaging the maximum power of the five sensors. As can be seen, the energy of the waves decreases and the corresponding frequency of the energy peak increase with an increasing superficial gas velocity. This analysis is done for all the retrieved film height data in order to find the interfacial properties of each case. The results will be discussed in the next section.
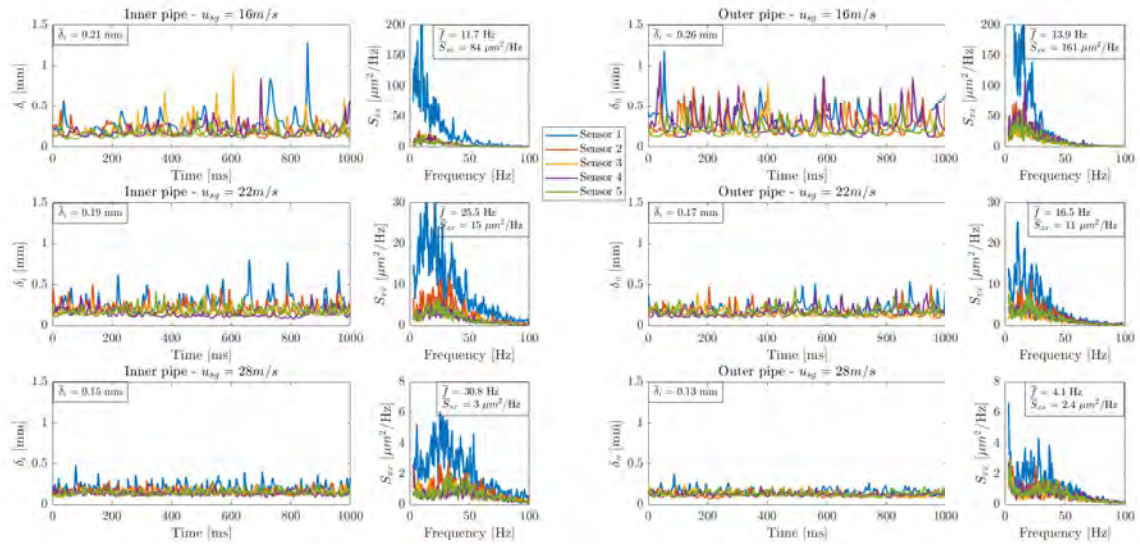
Figure 5.11: Film heights and the corresponding energy spectrum retrieved from the film height sensors. All results are for a superficial liquid velocity of 10 mm/s.

Disturbance wave energy spectra
In figure 5.12a the results are shown for equal liquid injection. When the liquid is applied equally on both pipes, it can be seen that a higher film thickness accompany higher energy waves. The superficial gas velocity has a decreasing effect on the energy. When the results for the outer and the inner sensors are compared, it can be seen that the measured wave energy is comparable. This subsequently indicates that the interfacial properties of both inner and outer films are more or less equal.

In figure 5.12b the results are shown for the single wall liquid injection. Note that only the results of the pipe, on which the liquid is injected, are represented. It is again observed that the energy for the same liquid throughput injected on the inner or outer pipe is of the same order of magnitude. When the results are compared with the equal injection curves, represented in figure 5.12a, it can be seen that the energy is 3-5 times higher for a u_{sl} equal to 5 mm/s and 10 mm/s.

As discussed, the energy of the disturbance waves are associated with the interfacial friction. These results imply that the interfacial friction for the liquid film, which is applied on one pipe, is slightly higher compared to a film which is injected equally on inner and outer pipe. This holds for the u_{sl} equal to 5 mm/s and 10 mm/s. This analysis is a possible explanation for the added interfacial stress for the case of single pipe liquid injection, which was discussed in section 5.1.
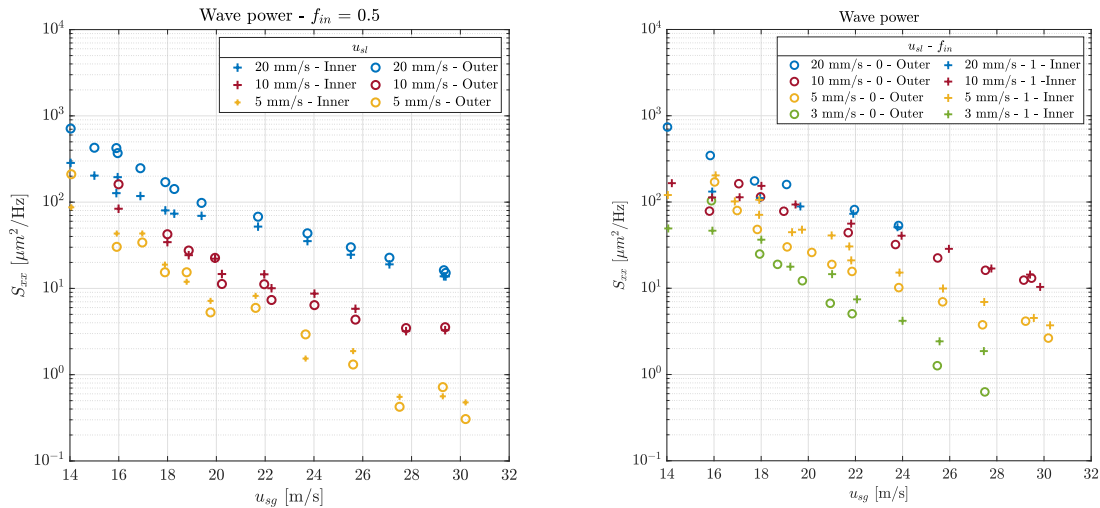
(a) Wave energy of the disturbance waves at the inner and outer pipe for equal liquid injection.

(b) Maximum energy of the disturbance waves at the inner and outer pipe for single pipe injection liquid injection. Only the sensor results are shown for the pipe on which the liquid is applied.

Figure 5.12: Result for the film height and volume throughput fraction between inner and outer pipe.

For the u_{sl} equal to 20 mm/s and single pipe injection, it was discussed that all the liquid will fully redistribute over both pipes, even when the liquid is injected on a single pipe wall, see figures 5.9a and 5.9b. Therefore, it is assumed that this also causes the comparable wave energy results for single wall injection and equal liquid injection, see figures 5.12b and 5.12a.

5.5. Film height sensor assessment

In section 5.1 a few reasons were given for the difference between the global and the local hold-up fraction. One reason comprehends the liquid film development. In this section an example calculation of the liquid film development effects will be given.

Film height development

When the liquid is injected through the 2 mm injection holes its direction needs to be changed and subsequently accelerated by the gas flow. In this section an example calculation will be presented based on educated guesses to estimate the effects of the film height development.

Suppose the annulus is exposed to a superficial gas and liquid velocity of 24 m/s and 5 mm/s respectively, where all the liquid is applied on the inner wall ($f_{in} = 1$). According to the local film measurement, this will result in a film of 197 μm. When it is assumed that all the liquid is present on the inner pipe, this case will result in a film thickness of 310 μm according the global hold-up measurement. It is assumed that 60 injection holes, with a diameter of 2 mm are used, which results in an injection velocity of 100 mm/s. A reaction time of 25 ms is assumed, where the direction of the radially injected liquid is changed into an axial flow direction. This results in an initial film height, δ_{in}, of 2.8 mm, see figure 5.13. A development length, z_{del}, of 2 m is assumed, where the initial film height linearly reaches its full developed height, δ_{del}.
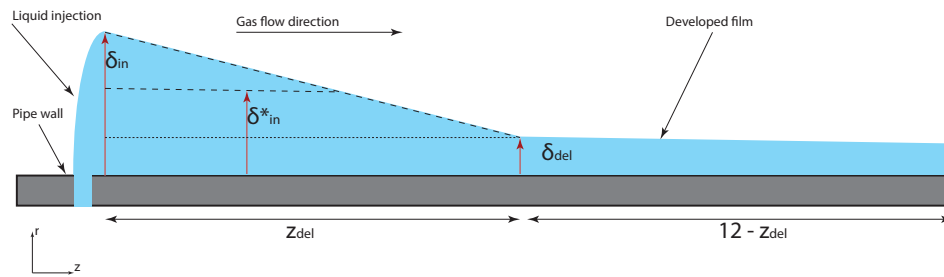
Figure 5.13: Calculation example for the development of the liquid film.

The total volume measured with the global hold-up fraction measurement was 1.19 l. When this volume is subdivided in the mean developing volume, using δ_{in}^*, and the developed volume, using δ_{del}, it results in a developed liquid film height of 220 μm. This calculated film height is 29% lower compared to the case where the development of the liquid film was not taken into account when using the global measured volume. Compared to the value measured with the film height sensor, this result is 15% higher.

It should be emphasized that the assumed values are educated guesses and this example is only meant to give an impression of the film height development and its effects on the difference between global and local measured film heights. It is recommended to conduct an additional CFD simulation to obtain a more accurate estimation.

6

Eccentric annulus

The aim of this chapter is to obtain more knowledge on how the flow characteristics, such as the pressure drop and liquid hold-up, are influenced by the eccentricity. For these experiments, the same annulus geometry is used as in Chapter 5 with four different eccentricities: $e = 0.5$, $e = 0.75$, $e = 0.9$ and $e = 1$. Each case is subjected to a superficial liquid velocity of: 5 mm/s, 10 mm/s and 20 mm/s. The injected liquid is equally divided between the inner and outer pipes. The results will again be subdivided into four different subjects:

- Pressure drop and the accompanying liquid hold-up.

- The effect of liquid bridging.

- The film height distribution along the circumference of the inner and outer pipe. In this section the film height assessment for the eccentric annulus is also included.

In the eccentric annulus geometry a few new terms will be introduced which are explained in figure 6.1. The orientations of the used film height sensors can be found in figure 4.8.
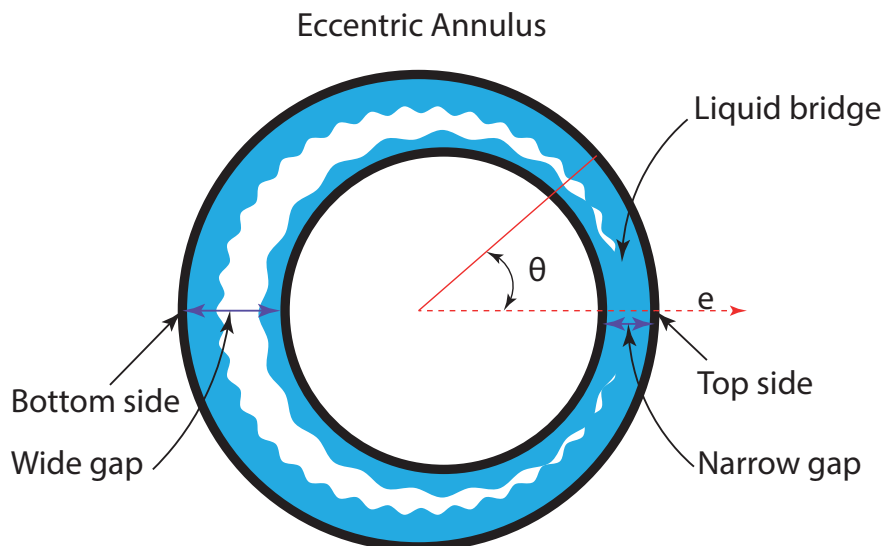
Figure 6.1: Terminology for the eccentric annulus.

6.1. Pressure drop

In this section all the pressure drop and global liquid hold-up fraction results will be discussed for an eccentric annulus.

Single phase pressure drop

Before an analysis is done on the the pressure drop for a multiphase system, it is interesting to determine how the eccentricity is affecting the pressure drop for single phase flow.

In figure 6.2, the pressure drop results for different eccentricities are shown. In these experiments, only air is used as the working fluid.
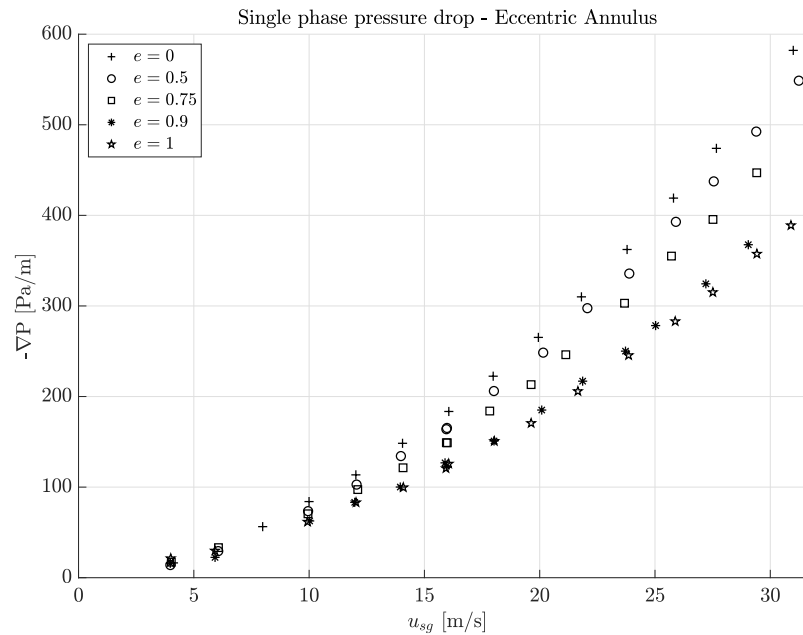
Figure 6.2: Single phase pressure drop for an eccentric annulus. The working fluid is air.

It is observed that the eccentricity has a decreasing effect on the pressure drop. The pressure drop is about 30% lower for a fully eccentric geometry, compared to the concentric case. This behaviour was also reported by Caetano et al. [10] and Nouri et al. [33].

Because of the eccentricity, the considered geometry can no longer be approached as axisymmetric. This causes that the wall shear stress and the accompanying velocity profile are no longer a function of solely the radial position, but also of the azimuthal position. This causes overall a lower pressure drop. However, this fluid problem is hard to analytically solve and this will not be a part of the scope in the current project. For the further discussion in the following sections it is convenient to realize that eccentricity has the tendency to reduce the pressure drop compared to a fully concentric annulus.

Multiphase pressure drop

In this section the results for the pressure drop and global liquid hold-up fraction will be discussed for the known air-water mixture. For reasons of convenience, only the results with u_{sl} equal to 10 mm/s are shown in this section. The results for the other liquid throughputs can be found in Appendix C.
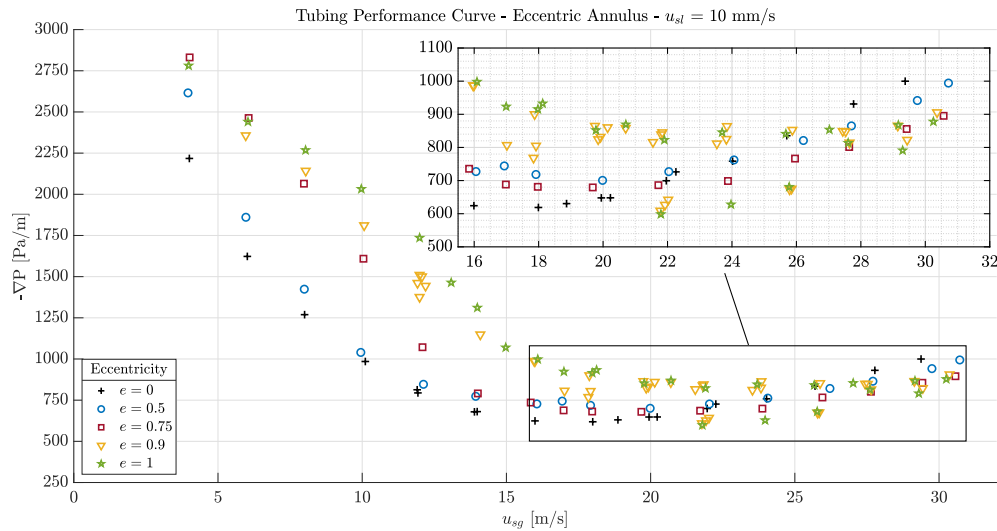
Figure 6.3: Tubing performance curves for eccentricities $e = 0$, $e = 0.5$, $e = 0.75$, $e = 0.9$ and $e = 1$. All results are for a $u_{sl} =$ 10 mm/s, equally divided over the two pipes.

In figure 6.3, it can be seen that for an eccentricity of 0.5, the pressure drop curve shows a similar trend compared to the fully concentric case. This holds also for the global liquid hold-up fraction, which can be seen in figure 6.4. The pressure drop for the annulus with $e = 0.5$ shows a slightly higher pressure drop between a u_{sg} equal to 6 m/s and 24 m/s compared to the fully concentric case, see figure 6.3. This is caused by a slightly larger liquid hold-up fraction for an eccentricity of 0.5, see figure 6.4. The larger hold-up is presumably the result of a lower gas velocity at the narrow gap, which results in more liquid accumulation. When the superficial gas velocity is further increased, it can be seen in figure 6.3 that the TPC for $e = 0.5$ intersects the full concentric TPC at a superficial gas velocity of 24 m/s. At this superficial gas velocity, the liquid hold-up fraction for $e = 0.5$ is higher compared to the concentric case. The reason why the extra liquid hold-up is not contributing to a higher pressure drop is likely to be the increase in eccentricity. The eccentricity tends to decrease the frictional pressure drop, as discussed in the previous section.

Eccentricities 0.9 and 1 show similar results for the pressure drop and for the liquid hold-up fraction, see figure 6.3 and 6.4. The pressure drop at superficial gas velocities lower than 20 m/s is much higher compared to the concentric case and is accompanied by higher liquid hold-ups, see figure 6.4. This higher liquid hold-up fraction is mainly caused by a phenomenon called liquid bridging.

In the narrow gap, the gas velocity is locally lower compared to the gas velocity in the wide gap. This causes that the liquid is accumulating in the narrow gap, which results in a thicker liquid film. Because the narrow gap size for $e = 0.9$ is relatively low, it is likely that the two liquid films locally merge which results in a liquid bridge, see figure 6.1. For an eccentricity of 1, this is continuously the case. When the liquid bridge is formed, the contact area between the gas flow and the liquid bridge is reduced. The interfacial stress applied on the liquid by the gas in order to transport the liquid upward is therefore also reduced. This causes a flow reversal of the liquid film in the liquid bridge. Since all the reversed liquid eventually has to be transported upward it induces a larger liquid hold-up fraction and thus also a larger pressure drop. In the higher superficial gas velocity range (u_{sg} between 20 m/s - 30 m/s) for the eccentricities 0.9 and 1, a scatter can be seen in the pressure drop, see figure 6.3.
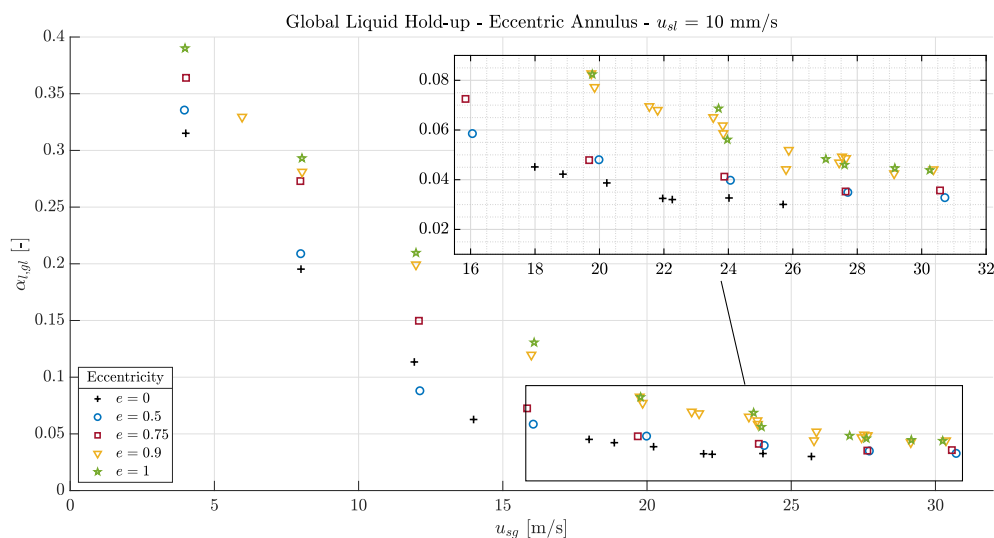
Figure 6.4: Global liquid hold-up fraction for eccentricities $e = 0$, $e = 0.5$, $e = 0.75$, $e = 0.9$ and $e = 1$. All results are for a u_{sl}= 10 mm/s, equally divided over the two pipes.

It is found, that this is caused by the development of the liquid bridge. When the liquid bridge is not yet developed, the flow reversal process has not yet started, which causes a lower liquid hold-up and thus a lower pressure drop. Therefore, the higher pressure drop results for $e = 0.9$ and $e = 1$ in figure 6.3 can be considered as the fully developed flow results. It is expected that this behaviour would also be visible for the liquid hold-up fraction. However, less data points are retrieved at these superficial gas velocities, which is the reason why no scattering is observed in figure 6.4.

At lower gas velocities, the liquid bridge is developed in an earlier stage due to more chaotic behaviour of the flow, which induces more mixing. Therefore, the scattering is not observed at lower superficial gas velocities. The onset and importance of the liquid bridge development will be more thoroughly discussed in section 6.2. It can be seen that the benefits of a reduced pressure drop for higher superficial gas velocities in an eccentric case for $e = 0.9$ and $e = 1$ are compensated by the liquid flow reversal in the liquid bridge.

The pressure drop results for an eccentricity of 0.75, in figure 6.3, are a combination of the three above mentioned eccentricity cases. For lower superficial gas velocities ($u_{sg} < 12$ m/s) a liquid bridge is constantly present and thus the pressure drops and liquid hold-up fractions are comparable for an eccentricity of 0.9 and 1. At a u_{sg} between 12 m/s - 16 m/s, a transition takes place, where the formed liquid bridge is (partially) removed. Therefore, at superficial gas velocities larger than 16 m/s, the pressure drop and liquid hold-up show the same trend as was observed for $e = 0$ and $e = 0.5$. For u_{sg} equal to 22 m/s, the TPC intersects the concentric TPC, which is the point where the lower pressure drop induced by the eccentricity becomes dominant.

When the different TPCs and global hold-up curves, for different eccentricities at a u_{sl} of 10 mm/s, are compared to the curves for a u_{sl} of 5 mm/s (figures D.3 and C.2) and 20 mm/s (figures C.3 and C.4), a few differences can be noted. For the low superficial gas velocities ($u_{sg} < 6$ m/s), the pressure drops are for all cases comparable, which is due to the total accumulation of liquid in the system. Therefore, the liquid hold-up fractions are also comparable. This observation is similar to the observation from the previous chapter for increasing liquid throughputs. When the gas velocity is increased, it can be seen that the pressure drop is relatively higher for higher liquid throughputs. This

holds for all eccentricities and is caused by the larger liquid hold-up in the system. Furthermore, it seems that the process of constant liquid bridging is starting at a higher u_{sl} values at an eccentricity of 0.75 and higher liquid throughputs. Lastly, it also be seen that the benefits of a lower pressure drop due to the increase of eccentricity are more clearly present for the higher liquid throughputs.

Kurian [28] reported similar trends for the pressure drop. However, the pressure drop values showed again a deviation of 20-30% for the higher superficial gas velocities ($u_{sg} > 20$ m/s). As discussed in the previous section, this is probably due to the larger equivalent gap size used in the present study. For the liquid hold-up fraction, similar results are found.

6.2. Liquid bridging

In the previous section, it became clear that the liquid bridge has a strong effect on the pressure drop. Furthermore, it was stated that the scattered results for an eccentricity equal to 0.9 and 1 were caused by a partially developed liquid bridge. This section will first discuss the liquid bridge development and its effect on the pressure drop. Secondly, a phenomenon called local flooding, associated with flow reversal in the liquid bridge, will be discussed.

Development of the liquid bridge

In order to proof the hypothesis that partially developed liquid bridges causes a lower pressure drop, an experiment needs to be conducted which covers the complete development of the liquid bridge. This is done by exposing the annulus with an eccentricity of 0.9 to a flow with a u_{sg} value of 24 m/s and a u_{sl} value of 10 mm/s. The pressure is continuously logged by the fifth pressure sensor (see figure 3.4), until the liquid bridge is developed. During this process, a camera at the same location as the pressure sensor is taking photographs with a frequency of 0.8 Hz for a visual validation. In figure 6.5 the pressure development are shown together with the annotations for the corresponding visual observations. These visual observations are shown in figure 6.6.
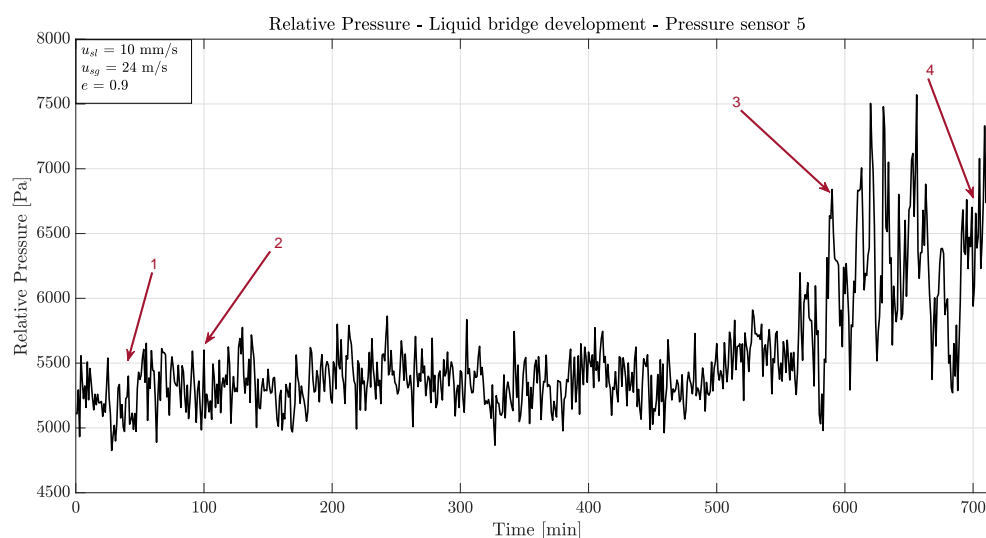
Figure 6.5: Relative pressure at the fifth sensor for the eccentric annulus ($e = 0.9$) for a u_{sl} equal to 10 mm/s and a superficial gas velocity of 24 m/s. The annotations correspond to the photographs, shown in figure 6.6.

In figure 6.5, it is clear that two different pressure regions can be distinguished. Between 0 and 550 s, the pressure is rather constant with relatively low pressure fluctuations. In the first two visual observations in figure 6.6, it is observed that this pressure region corresponds to a thin liquid bridge.

After 550 s the pressure rises rapidly and a transition starts. At this transition not only the pressure is increased, but also the variation in the pressure is increased. When consulting the visual observations, see photo 3 and 4 in figure 6.6, the liquid bridges look evenly spread in tangential direction and is much wider compared to the previous stage. This sudden change in increased pressure and width of the liquid bridge is associated with the development of the liquid bridge. The lower pressure region is linked to the undeveloped stage of the liquid bridge.

It was already assumed that the developed bridge, partially flowing downward, increases the liquid hold-up. Due to the increased liquid hold-up, the films become thicker and wavier, which subsequently causes a larger variation in pressure. Based upon this analysis, it is assumed that the undeveloped liquid bridge is the cause of the scattered pressure drop results in figure 6.3 for higher gas velocities.
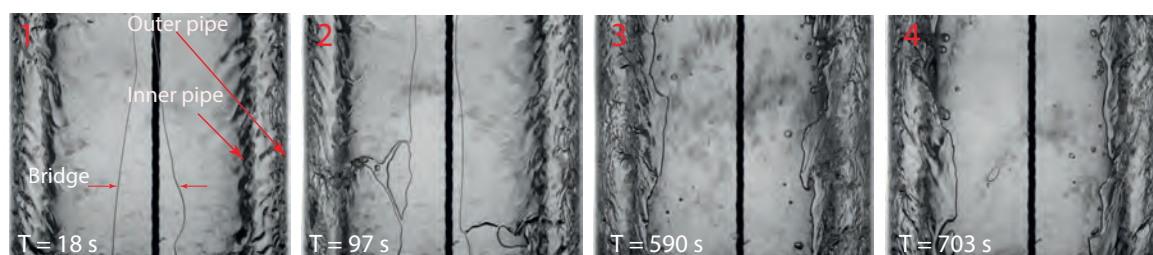
Figure 6.6: Top view photographs corresponding to the annotations in figure 6.5.

Local flooding

In section 6.1 it was stated that the liquid bridge is causing flow reversal. This is validated by analysing the results from the capacitance sensor, located below the liquid injection for the outer pipe. When flow reversal in the liquid bridge occurs, an amplified signal from the capacitance sensor will be returned. Figure 6.7 shows the results for a u_{sl} of 10 mm/s and different eccentricities. A value of 1 corresponds with a wetted area in between the electrodes and thus indicates flow reversal.

It should be noted that the fact that an amplified signal from the capacitance sensor is returned does not necessarily mean the onset of liquid loading. The liquid bridge formed causes partial flow reversal in the narrow gap, which is not equal to full liquid loading. Therefore, this phenomenon is often referred to as local flooding.

At an eccentricity of 0.5, the onset of flow reversal seems to start at a u_{sg} equal to 17 m/s, which is slightly higher than the value for the full concentric case. It is expected that this is caused by liquid accumulation in the narrow gap due to the locally lower gas velocity. This results in an earlier stage of flow reversal, compared to the full concentric case. At an eccentricity of 0.75, the signal is gradually increasing for decreasing gas velocities from 30 m/s. This suggest that for decreasing gas velocities, more liquid pockets are flowing downward. For eccentricities 0.9 and 1, constant flow reversal takes place, due to the constantly present liquid bridge.

6.3. Film height distribution

In Chapter 2, a brief introduction was given on the modeling of multiphase flow in an eccentric annulus. It was concluded that, in order to close the model, a relation needs to be formulated for the circumferential film height distribution as a function of the eccentricity.
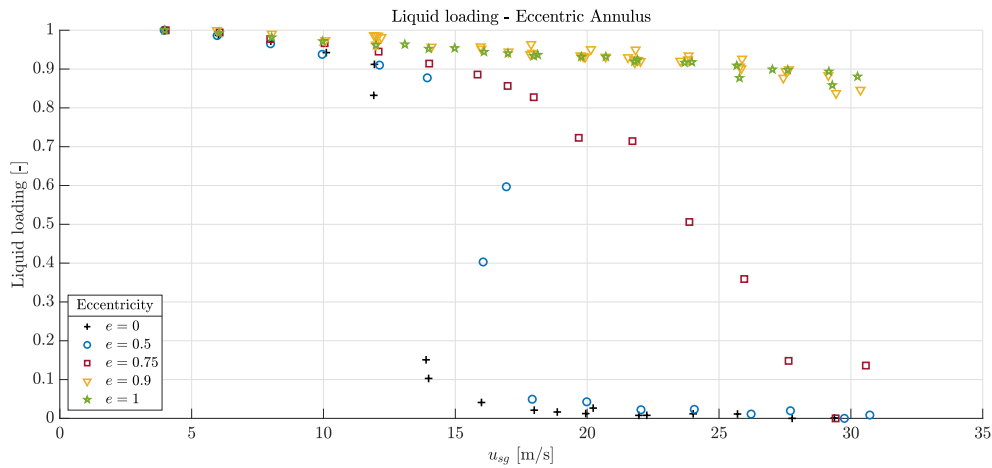
Figure 6.7: Dimensionless capacitance signal. A value of 1 corresponds to a fully wetted perimeter between the electrodes and 0 corresponds to a dry perimeter. The results shown are for different eccentricities and a u_{sl} of 10 mm/s.

This section will try to find out how the circumferential film height behaves, based on the results taken from the film height sensors in each pipe. First, the validation of the film height sensors is discussed. Secondly, a study is done on the effect of the eccentricity on the film height ratio between both pipes. Lastly, the results for the circumferential film height distribution will be discussed.

Film height sensor validation
In the previous chapter, t was stated that the sensors cannot provide reliable measurements for gas velocities below a u_{sg} of 16 m/s for the concentric case. When making the annulus eccentric, liquid bridging is a new phenomenon, which can possibly affect the measured result from the film height sensors. In this section, these effects of liquid bridging on the retrieved sensor signals will be discussed. It is expected that sensor 1 and 2 will be affected the most, since these sensors are located in the narrow gap.

In figure 6.8, the film heights measured at the inner pipe are shown for sensor 1 ($\theta = 0°$), 2 ($\theta = 45°$) and 3 ($\theta = 90°$) at different eccentricities, a u_{sl} of 10 mm/s and a u_{sg} of 22 m/s. Sensors 4 and 5 are not included in this analysis since they are located in the wide gap.

At an eccentricity of 0.5, the signals for the three different sensors show a predictable response, which can be compared to the concentric results in figure 5.11. In the previous section it was concluded that occasional liquid bridging occurs when the eccentricity is increased to 0.75. When consulting the results at $e = 0.75$ in figure 6.8, it is observed that the occasional liquid bridging indeed affects the signal at sensors 1 and 2. The high peak of sensor 2 can be explained by the passage of a disturbance wave. However, at the points annotated with the black arrows a deviating signal response is found. Here, the signal has a much higher frequency, with a much lower amplitude. Therefore this signal response behaves differently compared to the expected response of sensor 3.

At eccentricities 0.9 and 1, this result becomes even more visible, see figure 6.8. For these eccentricities it is known that there is constant liquid bridging. Therefore the returned film height should be equal to the size of the narrow gap. In the case of an eccentricity of 0.9, the size of the narrow gap at sensor 1 is equal to 1.2 mm. Instead of 1.2 mm, a film height of 0.25 mm is measured by sensor 1.
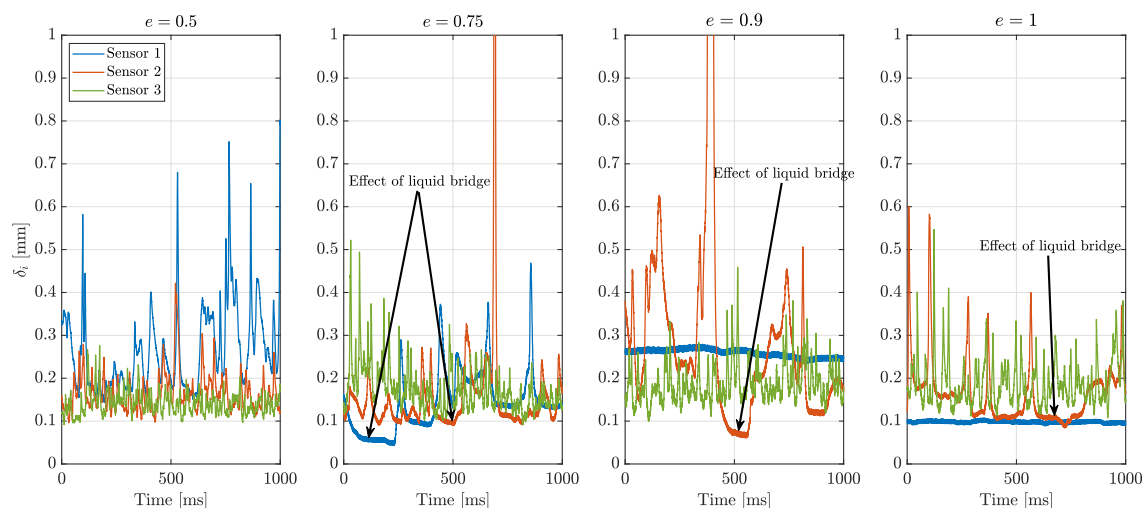
Figure 6.8: Film heights measured with sensors 1, 2 and 3 of the inner pipe for different eccentricities, with u_{sg}= 22 m/s and u_{sl}= 10 mm/s. For the eccentricities 0.9 and 1, the results correspond to a fully developed liquid bridge.

When the results are compared to the results for the outer pipe, for different u_{sg} and u_{sl}, the same effects are observed. It is assumed that liquid bridging at eccentricities of 1, 0.9 and even 0.75 locally change the electrical characteristics. This change in characteristics is because the signal for the sensors close to the liquid bridge, is no longer dominated by the conductance of the liquid. Capacitive or inductive responses are believed to be now locally dominant in the system. However, the real physical reason is not yet fully understood. Therefore, for the upcoming analysis in the next sections, the results from sensors 1 and 2 for eccentricities 0.75, 0.9 and 1 are not omitted. However, sensors 3, 4 and 5 still provide reliable results for both pipes.

Film height ratio

In this section, the effect of the eccentricity on the film height ratio between the inner and other pipe will be studied. This is done in a similar way as in the analysis in section 5.2, where the film heights of the inner and the outer pipe are compared by means of the mean cross sectional area occupied by the liquid. In the previous section, it became clear that for $e = 0.75$, $e = 0.9$ and $e = 1$ only sensors 3-5 give a reliable result. This means that for the comparison of the film height ratio, the contribution of the thick liquid bridge in the narrow gap with the mean film height will not be included.

In figure 6.9, the results for the film height ratio are shown in relation to the the eccentricity, for a u_{sg} of 16 m/s, 22 m/s and 28 m/s and different u_{sl}. It is observed that for a superficial gas velocity equal to 16 m/s, the film height is larger at the outer pipe. No redistribution effects are being observed when the eccentricity is increased. When the superficial gas velocity is increased to 22 m/s, a gradual shift occurs from the outer pipe to the inner pipe. This was already observed for the concentric annulus case. In the same concentric case it was observed that this shift towards the inner pipe is relatively less for higher liquid throughputs, which is possibly due to droplet atomization. This still seems to hold when the eccentricity is increased.

When the superficial gas velocity is increased to 28 m/s, a clear relation can be seen between the liquid redistribution from the inner pipe towards the outer pipe and the increase in eccentricity. For all the considered liquid throughputs, an increase in eccentricity causes a redistribution of the liq-

uid towards the outer pipe. It is assumed that the increased eccentricity induces a slow liquid film or even a liquid bridge with flow reversal in the narrow gap. The velocity difference between the large liquid film or bridge becomes therefore rather high, which causes a wavy interface. From this interface it is easier for the gas to atomise droplets, which are more likely to deposit on the outer pipe, which was discussed in the previous chapter.
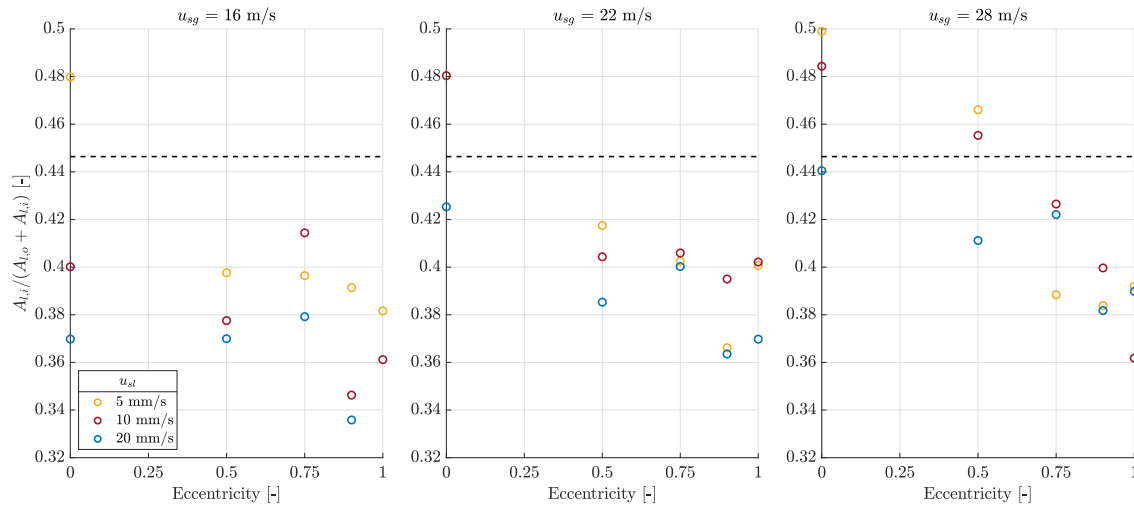
Figure 6.9: Film height ratio based on the cross sectional area occupied by liquid, for the inner and outer pipe. The black dashed line corresponds to an equal film height at the inner and outer pipe. The value for equal film height is put at 0.45, since the diameter ratio is included in the calculation of the area.

Circumferential distribution

In this section the effect of eccentricity on the circumferential distribution of the film height at both pipes will be discussed. As mentioned in Chapter 4, five sensors are present in the half-circumference of each pipe, see figure 4.2. Figure 6.11 shows the measured film height as a function of the tangential position, θ, for all considered eccentricities at the inner and outer pipe. Each two neighbouring graphs represent the distribution for the inner and the outer pipe at a specific superficial gas and liquid velocity. The columns from the left to the right represent a u_{sg} of 16 m/s, 22 m/s and 28 m/s, respectively. The rows from the top to the bottom represent conditions with u_{sl} of 5 mm/s, 10 mm/s and 20 mm/s, respectively. The results of sensor 1 and 2 for the eccentricities of 0.75, 0.9 and 1 are excluded from the analysis as discussed in the previous sections.

At a superficial gas velocity of 16 m/s, it can be seen that for all eccentricities and liquid throughputs, the film height is relatively higher at the outer pipe compared the inner pipe. This is in agreement with the observations in the previous section. For the eccentricities 0 and 0.5 an evenly distributed film is distinguished, which is represented by a straight line for the inner and outer pipe in figure 6.11 at a u_{sg} equal to 16 m/s. At an eccentricity equal to 0.75 a slight decreasing trend is observed for both pipes, at all liquid throughputs at the tangential positions 90°, 135° and 180°. It is assumed that frequent liquid bridging occurs at this eccentricity, which would induce a thicker liquid film at 0°. Therefore the hypothesis is that the decreasing trend is also present between the tangential positions of 0° and 90°. At an eccentricity equal to 0.9 and 1, a different behaviour is observed for the circumferential distribution. For the superficial liquid velocity equal to 10 mm/s and 20 mm/s, a thicker film is measured in the wide gap at the outer pipe.
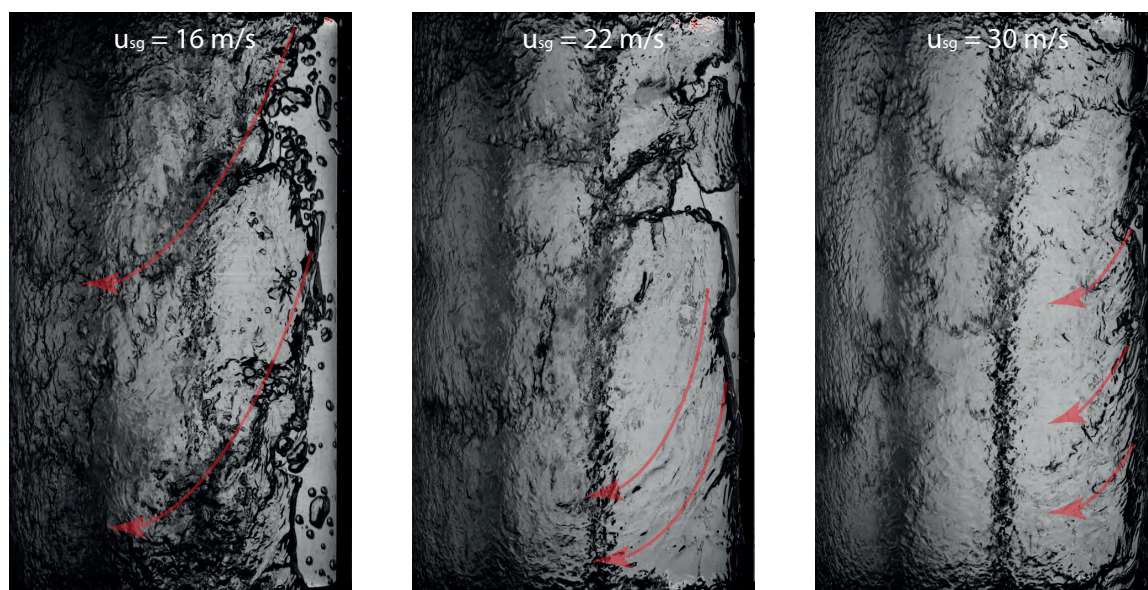
Figure 6.10: Side view photographs at a u_{sl} value of 20 mm/s and an eccentricity of 0.9. The red red arrows indicate the direction of the flow from the narrow gap towards the wide gap.

It seems that the liquid in the narrow gap is first transported to the wide gap via the outer pipe. In the first photograph of figure 6.10. Subsequently this liquid either accumulates or larger disturbance waves are present in the wider gap between 135° and 180°, before the liquid is transported upward and thus a thicker liquid film is measured. Presumably, this liquid accumulation in the wider gap does not occur at a superficial liquid velocity equal to 5 mm/s, simply because less liquid needs to be transported upward.

When the superficial gas velocity is increased to 22 m/s, the overall thickness of the liquid film at the inner and outer pipe is reduced compared to the thickness for u_{sg} equal to 16 m/s case, for all eccentricities and liquid throughputs. For the fully concentric case at superficial liquid velocity of 5 mm/s, liquid dry-out is present on the outer pipe at 90°, 135° and 180° and at the inner pipe at 180°. Furthermore, at the higher liquid throughputs again an evenly distributed liquid film height is observed. At an eccentricity of 0.5, a decreasing trend in the film height distribution from the narrow gap to the wider gap becomes more clearly visible for both pipes. It is assumed that the difference between the real gas velocities in the narrow and the wide gap, for a superficial gas velocity of 22 m/s, is larger compared to the 16 m/s case. Therefore, this larger difference in the gas velocity causes a larger difference in film height along the circumference. Furthermore, it seems that the increase in liquid throughput has a suppressing effect on this decreasing film height trend, especially for the inner pipe. For the eccentricities 0.75, 0.9 and 1 similar trends are observed between the superficial gas velocities of 22 m/s and 16 m/s. However, the liquid accumulation in the wider gap at the outer pipe starts for the superficial gas velocity of 22 m/s at a higher liquid throughput. Apparently, this superficial gas velocity is able to immediately transport the liquid upward for a superficial liquid velocity of 10 mm/s. In the middle photograph of figure 6.10, it can also be observed that the liquid in the narrow gap is firstly flowing downward until the liquid reaches the wide gap for a u_{sl} value of 20 mm/s.

At a superficial gas velocity of 28 m/s, the overall results show similar results for all the cases compared to the case with u_{sg} equal to 22 m/s. At $e = 0.9$ and $e = 1$, no liquid accumulation in the wider gap at the outer pipe is observed, for all liquid throughputs. This is in line with the hypothesis that the liquid accumulation at the wider gap for increased superficial gas velocity occurs at higher liquid throughputs. In the right photograph of figure 6.10 it can be seen that for the higher u_{sg} values and a u_{sl} value of 20 mm/s the tangential length at which flow reversal takes place is much smaller compared to the case where u_{sg} is equal to 22 m/s. This suggests that no liquid is able to accumulate at the wider gap. It would have interesting to study the circumferential liquid distribution at a superficial liquid velocity of 30 mm/s to see if indeed the film height in the wider gap increases at the outer pipe.

Although the data for the eccentricities 0.75, 0.9 and 1 for the tangential positions from 0° - 90° are not provided by the film height sensor, a good quantitative estimation of the missing distribution can still be made. During all the experiments, a camera recorded the top view of the annulus at 50 Hz for a duration of 14 s. Similar photographs are found in figure 6.6. From these recordings, it is possible to obtain the time-averaged liquid bridge width, which can be used to estimate the film height at the tangential positions from 0° - 90° of figure 6.11.

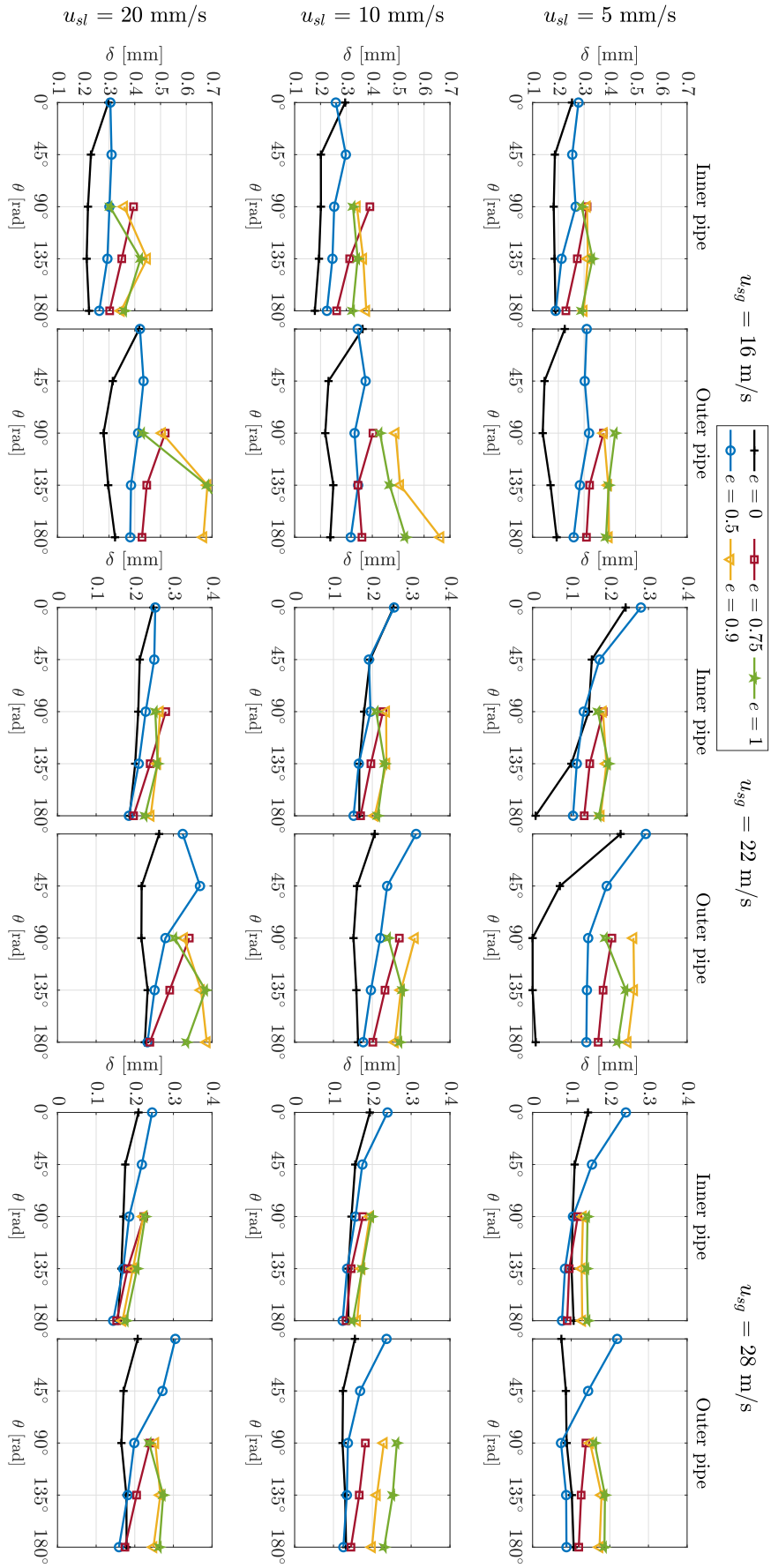Figure 6.11: Measured distribution along the half-circumference for all eccentricities at a u_{sg} equal to 16 m/s, 22 m/s and 28 m/s. The two neighbouring graphs show the distribution for the inner and the outer pipe, respectively. The results are shown for u_{sl} equal to 5 mm/s, 10 mm/s and 20 mm/s, which is varied in the three different rows. The accompanying mean film heights at every case can be found in table C.1.

7

Conclusion

In this thesis the flow characteristics of co-current vertical upward flow with an air-water mixture have been studied in a newly designed and in-house built mid-scale annulus flow facility. The current literature on this subject lacks essential experimental data. The aim of this study was to obtain and characterize experimental data to enable the construction of a reliable predictive model for annular flow in a vertical annulus. The obtained data predominantly included the pressure drop, the liquid hold-up, the film height ratio between the inner and the outer pipe, the flow characteristics of the air-water interface and the effect of eccentricity of the inner pipe on the circumferential film height distribution. The annulus set-up had a height of 12 m, consisting of an outer pipe with an internal diameter of 124 mm and an inner pipe with an outer diameter of 100 mm. This corresponds to a hydraulic diameter of 24 mm for the concentric configuration.

Local film height sensors
In order to measure representative film heights, flush mounted conductivity sensors were designed and built. Prior to the implementation in the annulus, the sensor's working principles and performances were thoroughly investigated and its accuracy was validated by multiple development tests, both under static and dynamic conditions. The film height sensor tests under dynamic test conditions showed reproducible results in a single pipe experiment with values that are 10-25% lower as compared to the film heights derived from the total liquid holdup as measured with the quick closing valves. The presence of small ripple waves on the liquid film, which may have a relatively smaller wave period compared to the distance between the probes can be one of the reasons for the lower values [20].

Based on these results five sensors were mounted in the half circumference of each pipe in order to find the film height distribution along the respective circumferences. The film sensors were first validated by comparing the results of the global hold-up measurements with the hold-up based on the averaged measured film height at each pipe, for which a 10-25% lower result for the sensors was found. One explanation, which was just mentioned above, is the presence of small ripple waves on the liquid film. Besides this reason, three other explanations were formulated to explain the difference. Firstly, the inclusion of the development length and liquid entrainment in the global hold-up measurement. Secondly, the occasional occurrence of dry spots at lower values of the superficial velocity and third, the higher gas velocity at the axial location closely to the top of the flow loop where the film sensors were located. When the film height ratio between the inner pipe and outer pipe as measured with the film height sensors was compared with the results of the liquid film separator at the outlet, similar results for the film height ratio and volume throughput ratio were found in all cases.

Liquid bridging in the eccentric annulus case is expected to change the electrical properties locally, causing the first two sensors in the narrow gap to become unreliable. The above mentioned results and arguments to support the conclusion that the film height sensors generate a realistic estimation of the local film height for the annular flow regime. At superficial gas velocities lower than 14 m/s the film height sensors are not able to accurately measure the liquid film due to gas enclosure in the liquid film.

Concentric annulus configuration

In the full concentric annulus configuration the effect of the liquid injection method was studied on the pressure drop, the liquid hold-up fraction, the onset of liquid loading and on the film height ratio. Three cases were experimentally investigated. In the first case the total liquid throughput at the inlet was equally divided between the inner and the outer pipe. In the second and third case all liquid was either applied on the inner pipe or on the outer pipe.

For the equal injection case, it was found that for lower values of the superficial gas velocity a slightly thicker liquid film is present the on the outer pipe wall than on the inner pipe wall, which is probably due to the atomization of droplets. Droplets are more likely to be deposited on the outer wall than on the inner wall, because of the larger surface area. When the superficial gas velocity is increased, the film heights on both pipes become equally thick. Video observations suggest that for lower liquid throughputs (denoted by the superficial liquid velocity u_{sl}) and larger gas throughputs (denoted by the superficial gas velocity u_{sg}), the film height at the inner pipe increases as compared to the film at the outer pipe.

For the single wall injection cases at lower u_{sl} and higher u_{sg} values, it was found that the liquid film tends to remain at the pipe wall at which it was injected. When the liquid throughput is increased, a redistribution takes place; it was observed that redistribution is easier from the inner pipe to the outer pipe than vice versa. The pressure drop was not affected by the method of liquid injection. However, the liquid hold-up was found to be 15-20% lower (as based on the local and global film height measurement). To follow up on these findings, a study was undertaken on the characteristics of the disturbance waves on the air-water interfaces. This was done by determining the mean energy spectrum for the films at both pipes. The disturbance wave energy of the films formed with single wall injection was found to be 3-5 times larger compared to the films formed with equal liquid injection at the same gas and liquid throughput. This explains the similar pressure drop for single wall and equal injection, while the hold-up fraction for single wall injection is lower.

Finally, the onset of liquid loading was investigated. It was observed that the critical superficial gas velocity at which the liquid loading process starts is equal to 14 m/s for all cases and is thus neither influenced by the method of liquid injection nor by the liquid throughput.

Eccentric annulus configuration

In the eccentric annulus configuration the effect of eccentricity on the pressure drop, the global liquid hold-up fraction and on the circumferential film height distribution were investigated. Single phase experiments, using air as the working fluid, showed that the pressure drop is reduced by 30% in the fully eccentric case in comparision to the concentric case. for two phase flow with air-water, it was observed that the pressure drop for a superficial gas velocity between 6 m/s and 24 m/s is slightly higher at an eccentricity (e) of 0.5 as compared to the fully concentric case. The larger pressure drop is presumably due to a larger liquid hold-up fraction at an eccentricity of 0.5, caused by the lower local gas velocity in the narrow gap. The lower gas velocity gives an increased liquid ac-

cumulation. When the eccentricity is increased to 0.9 or 1, much higher pressure drops and liquid hold-up fractions are observed. For these eccentricities, the accumulation in the narrow gap becomes so dominant that the film at the inner pipe locally merges with the film at the outer pipe resulting in liquid bridging. Due to gravity, the liquid bridge causes flow reversal in the narrow gap, which subsequently results in a larger liquid hold-up fraction as compared to the $e = 0$ and $e = 0.5$ cases. At an eccentricity of 0.75 and low superficial gas velocities (u_{sg} <12 m/s) a constant liquid bridge is formed where the pressure drop is comparable to the $e = 0.9$ and $e = 1$ cases. At higher u_{sg} values the results follow the same trend as in the case with $e = 0.5$. However, the liquid hold-up fraction is slightly larger. All eccentricities give a lower pressure drop as compared to the full concentric case at higher gas velocities. This behaviour is similar as observed in the single phase case. The film height ratio is not affected by the eccentricity at low gas velocities. When the superficial gas velocity is increased the eccentricity causes a redistribution of the liquid from the inner pipe to the outer pipe.

Finally the circumferential film height distribution was studied. At higher gas velocities (u_{sg} > 22 m/s) a clearly decreasing film height trend was observed from the narrow gap towards the wide gap for $e = 0.5$. It was concluded that the increase in liquid throughput has a suppressing effect on this decreasing film height trend. Furthermore, liquid accumulation was observed at the outer pipe in the wide gap for $e = 0.9$ and $e = 1$ and at higher liquid throughputs. This observation is probably due to the liquid the rapid liquid migration from the narrow gap to the wide gap where it subsequently accumulates. The complete circumferential distribution for the annulus with an $e = 0.75$, $e = 0.9$ and $e = 1$ could not be obtained at the narrow gap due to the electronic impact of the liquid bridge on the film sensors. An additional analysis of the image recordings is recommended to quantify the width of the liquid bridge, and to obtain a better understanding of the circumferential film height distribution at these eccentricities.

7.1. Recommendations

The study presented in this thesis has provided a new efficient and multifunctional experimental research set-up that was demonstrated to give valuable insights on the flow characteristics of annular flow in a vertical annulus. Some recommendations for follow up work, which includes additional analysis of the current experimental data as well as the continuation of experiments in order to obtain new data and insights, are as follows:

- For all the conducted experiments side view videos of the flow were recorded. From these videos the liquid velocity at the wide and narrow gap can be determined by cross-correlating the subsequent frames. Preliminary studies already showed promising results for *e.g.* the gas velocity at which flow reversal in the narrow gap is no longer occurring at higher eccentricities.

- From the top view recordings the time-averaged liquid bridge width can be obtained for $e = 0.75$, $e = 0.9$ and $e = 1$, enabling the estimation of the film height at tangential positions ranging from 0° - 90°. These time-averaged results will provide a relation between the tangential position and the film height along the circumference.

- The retrieved film height data will support the determination of the characteristics of the disturbance waves at the top side and at the bottom side of both pipes for $e = 0.5$.

- The liquid film development at the liquid injection location can be determined by conducting a CFD simulation. The results from such a simulation, which provides a better understanding of the difference between the global and the local liquid hold-up fractions.

- The position of the local film height measurements can be moved further upstream in order to investigate the local liquid hold-up fraction near the liquid injection location. These results

can subsequently be compared with the current results for the same liquid and gas through-puts in order to find any liquid film development effects.

- Other electronically conducting working fluids may be used to find the impact of the density, the viscosity, and the surface tension on the *e.g.* redistribution and disturbance wave characteristics.

The used film sensors provide a realistic indication of the local film height. Additional development of its functionality and accuracy can lead to further improvements. Some suggestions are listed below:

- The used analog signal cables are relatively long. This affects the measurement range of the used sensors. It is recommended to locate the data acquisition of the retrieved signal from the sensors as close as possible to the sensors. With respect to the data acquisition circuit the analog signal needs to be converted into a digital signal. Such a digital signal will have an increased ruggedness with respect to external electronic noise and will thus enable the use of longer cables.

- The sensors should be made electronically non-floating, which can be realised by implementing a point where the fluid is grounded. This will make the system less vulnerable to unwanted electrical changes, which will probably solve the measurement problems observed with liquid bridging.

- A reference sensor with an imposed film height can be placed at the outlet. By doing so the signal will include temperature and evaporation effects. This reference value can be used to concurrently calibrate the other sensors.

- A sensor mesh can be implemented to get a better spacial resolution of the film height distribution along the circumference. Furthermore, the sensors can be implemented at multiple axial positions to find the velocity of disturbance waves. In Appendix A it was tried to implement such a sensor, but capacitive coupling generating unreliable results was experienced. Based on this finding it is recommended to use shorter cables and to 'print' the sensors with the accompanying ground plane on a flexible PCB. This flexible PCB can subsequently be installed in the annulus research set-up.

Bibliography

[1] International Energy Agency. *Gas 2018*. ORGN FOR ECONOMIC, 2018. ISBN 926430133X.

[2] W. Ambrosini, P. Andreussi, and B.J. Azzopardi. A physically based correlation for drop size in annular flow. *International Journal of Multiphase Flow*, 17(4):497–507, 1991. doi: 10.1016/0301-9322(91)90045-5.

[3] P.S. Andersen and J. Würtz. Adiabatic steam-water annular flow in an annular geometry. *International Journal of Multiphase Flow*, 7(2):235–239, 1981. doi: 10.1016/0301-9322(81)90008-2.

[4] P. Andreussi, E. Pitton, P. Ciandri, D. Picciaia, A. Vignali, M. Margarone, and A. Scozzari. Measurement of liquid film distribution in near-horizontal pipes with an array of wire probes. *Flow Measurement and Instrumentation*, 47:71–82, 2016. doi: 10.1016/j.flowmeasinst.2015.12.007.

[5] Takahiro Arai, Masahiro Furuya, Taizo Kanai, and Kenetsu Shirakawa. Concurrent upward liquid slug dynamics on both surfaces of annular channel acquired with liquid film sensor. *Experimental Thermal and Fluid Science*, 60:337–345, 2015. doi: 10.1016/j.expthermflusci.2014.05.018.

[6] B.J. Azzopardi. Disturbance wave frequencies, velocities and spacing in vertical annular two-phase flow. *Nuclear Engineering and Design*, 92(2):121–133, 1986. doi: 10.1016/0029-5493(86)90240-2.

[7] R.J. Belt. *On the liquid film in inclined annular flow*. PhD thesis, Delft University of Technology, 2007.

[8] R.J. Belt, J.M.C. Van't Westende, and L.M. Portela. Prediction of the interfacial shear-stress in vertical annular flow. *International Journal of Multiphase Flow*, 35(7):689–697, 2009. doi: 10.1016/j.ijmultiphaseflow.2008.12.003.

[9] C. Berna, A. Escrivá, J.L. Muñoz-Cobo, and L.E. Herranz. Review of droplet entrainment in annular flow: Interfacial waves and onset of entrainment. *Progress in Nuclear Energy*, 74:14–43, 2014. doi: 10.1016/j.pnucene.2014.01.018.

[10] E. F. Caetano, O. Shoham, and J. P. Brill. Upward vertical two-phase flow through an annulus—part i: Single-phase friction factor, taylor bubble rise velocity, and flow pattern prediction. *Journal of Energy Resources Technology*, 114(1):1, 1992. doi: 10.1115/1.2905917.

[11] E. F. Caetano, O. Shoham, and J. P. Brill. Upward vertical two-phase flow through an annulus—part II: Modeling bubble, slug, and annular flow. *Journal of Energy Resources Technology*, 114(1):14, 1992. doi: 10.1115/1.2905916.

[12] L. Cheng, G. Ribatski, and J. R. Thome. Two-phase flow patterns and flow-pattern maps: Fundamentals and applications. *Applied Mechanics Reviews*, 61(5), 2008. doi: 10.1115/1.2955990.

[13] Andrea Cioncolini and John R. Thome. Prediction of the entrained liquid fraction in vertical annular gas–liquid two-phase flow. *International Journal of Multiphase Flow*, 36(4):293–302, 2010. doi: 10.1016/j.ijmultiphaseflow.2009.11.011.

[14] M W E Coney. The theory and application of conductance probes for the measurement of liquid film thickness in two-phase flow. *Journal of Physics E: Scientific Instruments*, 6(9):903–911, 1973. doi: 10.1088/0022-3735/6/9/030.

[15] M. Damsohn and H.-M. Prasser. High-speed liquid film sensor for two-phase flows with high spatial resolution based on electrical conductance. *Flow Measurement and Instrumentation*, 20(1):1–14, 2009. doi: 10.1016/j.flowmeasinst.2008.06.006.

[16] G. Das, P. K. Das, N. K. Purohit, and A. K. Mitra. Flow pattern transition during gas liquid up-flow through vertical concentric annuli—part i: Experimental investigations. *Journal of Fluids Engineering*, 121(4):895, 1999. doi: 10.1115/1.2823552.

[17] Larry B. Fore and Abraham E. Dukler. Droplet deposition and momentum transfer in annular flow. *AIChE Journal*, 41(9):2040–2046, 1995. doi: 10.1002/aic.690410904.

[18] L.B Fore, S.G Beus, and R.C Bauer. Interfacial friction in gas–liquid annular flow: analogies to full and transition roughness. *International Journal of Multiphase Flow*, 26(11):1755 – 1769, 2000. ISSN 0301-9322. doi: https://doi.org/10.1016/S0301-9322(99)00114-7. URL http://www.sciencedirect.com/science/article/pii/S0301932299001147.

[19] F. Fu and J.F. Klausner. A separated flow model for predicting two-phase pressure drop and evaporative heat transfer for vertical annular flow. *International Journal of Heat and Fluid Flow*, 18(6):541–549, 1997. doi: 10.1016/s0142-727x(97)00001-5.

[20] G.F. Hewitt and N.S. Hall-Taylor. *Annular two-phase flow*. Pergamon Press, 1970.

[21] Takashi Hibiki and Kaichiro Mishima. Flow regime transition criteria for upward two-phase flow in vertical narrow rectangular channels. *Nuclear Engineering and Design*, 203(2-3):117–131, 2001. doi: 10.1016/s0029-5493(00)00306-x.

[22] M. Ishii and M. A. Grolmes. Inception criteria for droplet entrainment in two-phase concurrent film flow. *AIChE Journal*, 21(2):308–318, 1975. doi: 10.1002/aic.690210212.

[23] P. Ju, Y. Liu, C.S. Brooks, and M. Ishii. Prediction of interfacial shear stress of vertical upward adiabatic annular flow in pipes. *International Journal of Heat and Mass Transfer*, 133:500–509, 2019. doi: 10.1016/j.ijheatmasstransfer.2018.12.057.

[24] J. Enrique Julia and Takashi Hibiki. Flow regime transition criteria for two-phase flow in a vertical annulus. *International Journal of Heat and Fluid Flow*, 32(5):993–1004, 2011. doi: 10.1016/j.ijheatfluidflow.2011.06.001.

[25] J. Enrique Julia, Basar Ozar, Jae-Jun Jeong, Takashi Hibiki, and Mamoru Ishii. Flow regime development analysis in adiabatic upward two-phase flow in a vertical annulus. *International Journal of Heat and Fluid Flow*, 32(1):164–175, 2011. doi: 10.1016/j.ijheatfluidflow.2010.09.003.

[26] V.C. Kelessidis and A.E. Dukler. Modeling flow pattern transitions for upward gas-liquid flow in vertical concentric and eccentric annuli. *International Journal of Multiphase Flow*, 15(2):173–191, 1989. doi: 10.1016/0301-9322(89)90069-4.

[27] J.E. Koskie, I. Mudawar, and W.G. Tiederman. Parallel-wire probes for measurement of thick liquid films. *International Journal of Multiphase Flow*, 15(4):521–530, 1989. doi: 10.1016/0301-9322(89)90051-7.

[28] Jesil Kurian. Experiments and modelling of gas-liquid flow in a vertical annulus. Master's thesis, Delft University of Technology, the Netherlands, 2018.

[29] J.F. Lea and H.V. Nickens. *Gas Well Deliquification*. Gulf Professional Publishing, 2008. ISBN 9780080484198.

[30] Kyu Lee, Jong Kim, Goon Park, and Hyoung Cho. Feasibility test of a liquid film thickness sensor on a flexible printed circuit board using a three-electrode conductance method. *Sensors*, 17 (12):42, 2016. doi: 10.3390/s17010042.

[31] Fang-Yu Liang, Marta Ryvak, Sara Sayeed, and Nick Zhao. The role of natural gas as a primary fuel in the near future, including comparisons of acquisition, transmission and waste handling costs of as with competitive alternatives. *Chemistry Central Journal*, 6(Suppl 1):S4, 2012. doi: 10.1186/1752-153x-6-s1-s4.

[32] C.J. Martin. *Annular two phase flow*. PhD thesis, University of Oxford, 1983.

[33] J. M. Nouri, H. Umur, and J. H. Whitelaw. Flow of newtonian and non-newtonian fluids in concentric and eccentric annuli. *Journal of Fluid Mechanics*, 253(-1):617, 1993. doi: 10.1017/s0022112093001922.

[34] Erika V. Pagan and Paulo J. Waltrich. A simplified model to predict transient liquid loading in gas wells. *Journal of Natural Gas Science and Engineering*, 35:372–381, 2016. doi: 10.1016/j.jngse.2016.08.059.

[35] L. Pan, H. He, P. Ju, T. Hibiki, and M. Ishii. The influences of gas–liquid interfacial properties on interfacial shear stress for vertical annular flow. *International Journal of Heat and Mass Transfer*, 89:1172–1183, 2015. doi: 10.1016/j.ijheatmasstransfer.2015.06.022.

[36] H.-M Prasser, A Böttger, and J Zschau. A new electrode-mesh tomograph for gas–liquid flows. *Flow Measurement and Instrumentation*, 9(2):111–119, 1998. doi: 10.1016/s0955-5986(98)00015-6.

[37] O.L. Pushkina and Y.L. Sorokin. Breakdown of liquid film motion in vertical tubes. *Heat Transfer Soviet Res.*, 1(5):56–64, 1969.

[38] Horst J. Richter. Flooding in tubes and annuli. *International Journal of Multiphase Flow*, 7(6): 647–658, 1981. doi: 10.1016/0301-9322(81)90036-7.

[39] Pravin Sawant, Mamoru Ishii, Tatsuya Hazuku, Tomoji Takamasa, and Michitsugu Mori. Properties of disturbance waves in vertical annular two-phase flow. *Nuclear Engineering and Design*, 238(12):3528–3541, 2008. doi: 10.1016/j.nucengdes.2008.06.013.

[40] Pravin Sawant, Mamoru Ishii, and Michitsugu Mori. Prediction of amount of entrained droplets in vertical annular two-phase flow. *International Journal of Heat and Fluid Flow*, 30 (4):715–728, 2009. doi: 10.1016/j.ijheatfluidflow.2009.03.003.

[41] J.G. Speight. *Handbook of Natural Gas Analysis*. John Wiley & Sons, 2018. ISBN 9781119240280.

[42] G. Su, J. Gou, K. Fukuda, and D. Jia. A theoretical model of annular upward flow in a vertical annulus gap. *Journal of Nuclear Science and Technology*, 40(1):1–11, 2003. doi: 10.1080/18811248.2003.9715326.

[43] N. Hall Taylor, G.F. Hewitt, and P.M.C. Lacey. The motion and frequency of large disturbance waves in annular two-phase flow of air-water mixtures. *Chemical Engineering Science*, 18(8): 537–552, 1963. doi: 10.1016/0009-2509(63)85014-9.

[44] N.S. Hall Taylor and R.M. Nedderman. The coalescence of disturbance waves in annular two phase flow. *Chemical Engineering Science*, 23(6):551–564, 1968. doi: 10.1016/0009-2509(68) 89003-7.

[45] Cristiano Bigonha Tibiriçá, Francisco Júlio do Nascimento, and Gherhardt Ribatski. Film thickness measurement techniques applied to micro-scale two-phase flow systems. *Experimental Thermal and Fluid Science*, 34(4):463–473, 2010. doi: 10.1016/j.expthermflusci.2009.03.009.

[46] R.G. Turner, M.G. Hubbard, and A.E. Dukler. Analysis and prediction of minimum flow rate for the continuous removal of liquids from gas wells. *Journal of Petroleum Technology*, 21(11): 1475–1482, 1969. doi: 10.2118/2198-pa.

[47] A.T. van Nimwegen, L.M. Portela, and R.A.W.M. Henkes. Modelling of upwards gas-liquid annular and churn flow with surfactants in vertical pipes. *International Journal of Multiphase Flow*, 105:1–14, 2018. doi: 10.1016/j.ijmultiphaseflow.2017.09.012.

[48] J.M.C. van 't Westende, H.K. Kemp, R.J. Belt, L.M. Portela, R.F. Mudde, and R.V.A. Oliemans. On the role of droplets in cocurrent annular and churn-annular pipe flow. *International Journal of Multiphase Flow*, 33(6):595–615, 2007. doi: 10.1016/j.ijmultiphaseflow.2006.12.006.

[49] G.B. Wallis. *One-dimensional two-phase flow*. McGraw-Hill, New York, 1969.

[50] Zhaolin Wang, Kamiel S. Gabriel, and Devon L. Manz. The influences of wave height on the interfacial friction in annular gas–liquid flow under normal and microgravity conditions. *International Journal of Multiphase Flow*, 30(10):1193–1211, 2004. doi: 10.1016/j.ijmultiphaseflow. 2004.06.003.

[51] B. Yin, X. Li, B. Sun, and H. Zhang. Hydraulic model of steady state multiphase flow in wellbore annuli. *Petroleum Exploration and Development*, 41(3):399–407, 2014. doi: 10.1016/ s1876-3804(14)60046-x.

A

Film sensor development

This Appendix will give in-depth insight on the development of the film sensor towards its final state. Three development tests were necessary to fully understand the signal response and the effects of the important geometrical parameters. These development tests will be discussed in the first three sections of this Appendix. The last section will cover the attempt to implement the sensor mesh, which was briefly discussed in section 4.1.

A.1. Development stage 1

The first development stage was done to find whether a reliable and reproducible signal response could be extracted by varying the film height. Furthermore, this development stage was used to validate the electrical circuit showed in figure 4.5, to find the frequency response, and to find the water concentration effects. The set-up shown in figure A.1 was used. This set-up has a fixed probe distance d_p of 3 mm and the cylindrical probes have a diameter, d_w of 2 mm. The film height is imposed by a glass plate on four spacers with a specific length. Normal tap water at 19 °C was used as liquid.
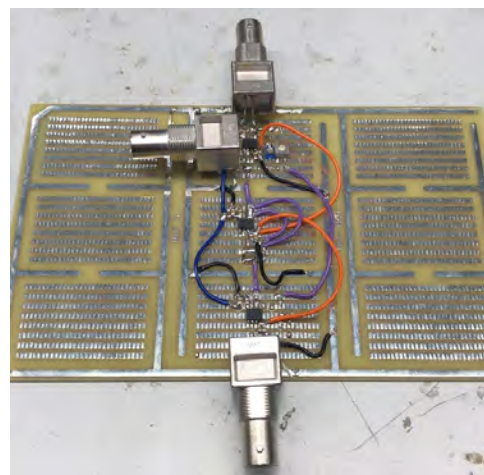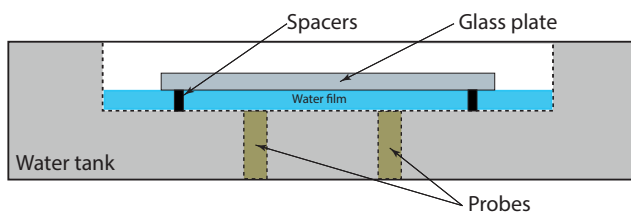

Figure A.1: Left, the cross-section of the test set-up for the first development stage. Right, a picture of the first version of the electrical circuit. This circuit has only one input option.

Frequency response

First, the frequency response was determined. A peak-to-peak voltage of 1 V was used to excite the transmitter. For the first experiment, a feedback resistance of 200 kΩ in combination with a 12 pF capacitance was implemented in the electrical circuit. This will result in a cut-off frequency of 66 kHz (see equation 4.5), which is rather low when considering a minimal excitation frequency of 100 kHz. The results of the first experiment are shown in figure A.2a. As can be seen in figure A.2a, the amplification of the signal is decreasing for frequencies above 20 kHz, which is the result of the combination of the R_z and C_z values. When frequencies of more than 100 kHz are desired, the result shown in figure A.2a is not promising due to the fact that the system is not dominated by resistance. Furthermore, the amplification factor of the system for lower frequencies is between 8 and 15 which means that the resistance of the film is highly overestimated. For the film height resistance of 0.2 mm, an amplification factor of 7.5 can be found, which means that the film has a resistance of 26 kΩ.

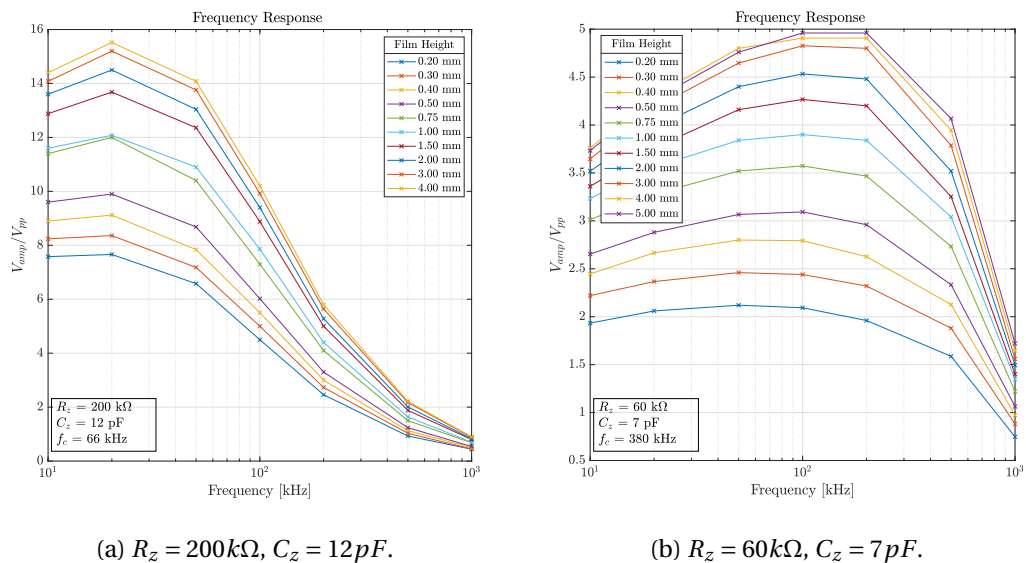(a) $R_z = 200 k\Omega$, $C_z = 12 pF$.   (b) $R_z = 60 k\Omega$, $C_z = 7 pF$.

Figure A.2: Frequency responses for different film heights. Probe dimensions: $d_p = 3$ mm and $d_w = 2$ mm.

To improve the electrical system, the values of R_z and C_z were replaced by a 60 kΩ resistor and a 7 pF capacitor, respectively. This combination of feedback values has a cut-off frequency of 380 kHz. The result are shown in figure A.2b. As can be seen, the amplification of the signal is lower compared to the results in figure A.2a, due to the lower value of R_z, see equation 4.4. However, the amplification starts to decrease beyond a frequency 200 kHz which means that the amplification is purely driven by resistance. Furthermore, as expected, the 26 kΩ film resistance at 0.2 mm is amplified with a factor 2.

Concentration effects

The next test was to find the water concentration effects due to the expected evaporation. The evaporation will increase the concentration of electrolytes in the water, resulting in a higher conductivity. First, a normal film height response of tap water was made at a frequency of 200 kHz and a peak-to-peak voltage of 1 V was used, see figure A.3. The result is as expected, with a linear part at lower film heights and with a flatting behaviour from 1.5 mm, towards a saturation point at around 3.4 V. Then a sample was drawn from a 12 m single pipe set-up, which was also used by van Nimwegen et al. [47], at a u_{sg} of 28 m/s. At this velocity, it is expected that some evaporation occurs.
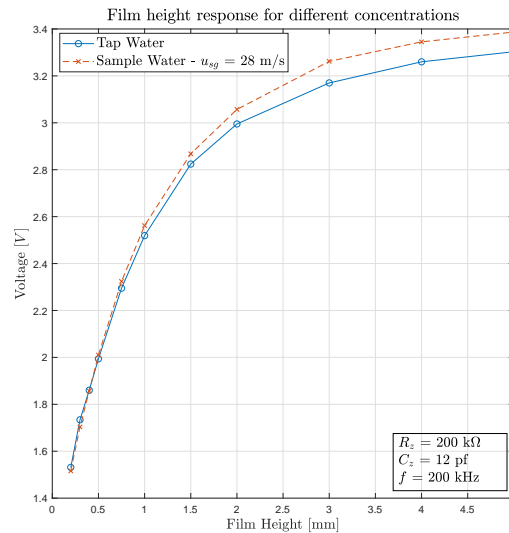
Figure A.3: Signal response for normal tap water and a tap water sample drawn from a set-up used by van Nimwegen et al. [47] at a u_{sg} of 28 m/s.

The sample was tested at the same temperature as the tap water measurement, to prevent any temperature effects. The result is also shown in figure A.3 and is partly overlapping with the result of normal tap water for the linear part. At higher film heights, the sample has a 3% higher signal than tap water. From this result it is concluded that the concentration effects are not dominantly present.

Reproducibility

The tap water experiments as shown in figure A.3 were repeated three times in order to find the reproducibility. It was found that the standard deviation of the signals at the measured film heights does not exceed 3%.

A.2. Development stage 2

The first development stage showed that the electrical system worked properly and that the film height could be measured repeatedly with an acceptable precision. However, the previous development stage was under static conditions. Therefore, it was chosen to find the measurement accuracy under dynamic conditions, using the same electrical circuit as was shown in A.1. In figure A.4, the existing single pipe flow loop for co-current upward flow, used by van Nimwegen et al. [47], can be seen. This set-up was used to conduct the second development stage. The advantage was that the results of the sensors could be validated by the result of the hold-up valves. Furthermore, the temperature effects on the signal were investigated.

The 12 m long vertical flow loop has a diameter of 50 mm and is built out of 1 m segments. A 1 m segment was replaced by a 70 cm segment connected to a 30 cm segment in which the probes are installed. This segment has a diameter of 51.24 mm. Two sets of cylindrical probes are installed with a distance, d_p, of 2 mm and 3 mm, respectively, and they were measured separately. This is done to find the effect of the probe distance on the measurement range. All the probes have a diameter of 2 mm. The sensors are calibrated for 7 film heights, using existing calibration cylinders. These cylinders were taken from another set-up and were not tailor made for the pipe segment.
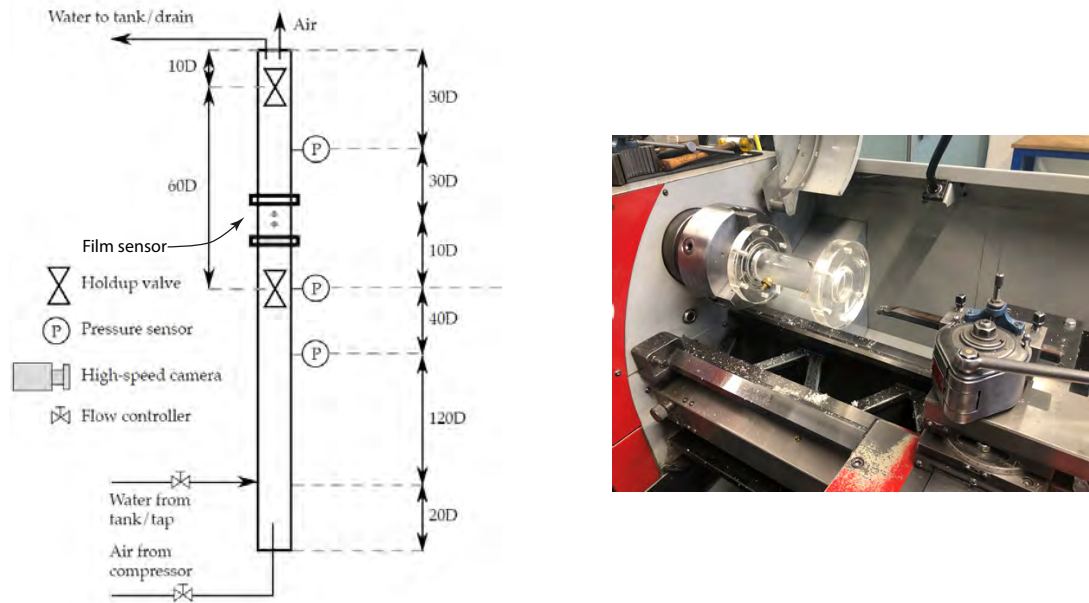
Figure A.4: Left, the flow loop used by van Nimwegen et al. [47] with the location of the test section. Right, a picture of the test section in the turning machine, a part of the production process.
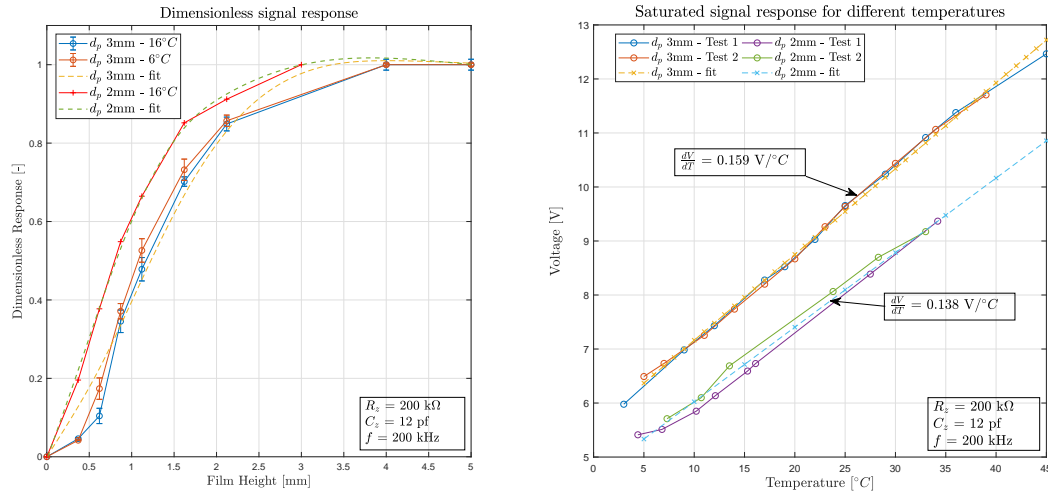
Temperature effects

In the first development stage, the temperature effects were not studied. The manufactured set-up in this development stage is more convenient to conduct a temperature study. The sensor with a d_p of 3 mm was calibrated at conditions of 16 °C and 6 °C, respectively, to find how the dimensionless calibration curve is affected. The dimensionless calibration curve is found by dividing all data points on the curve by the saturated signal.

Figure A.5a shows the results of the calibration. First of all, the result of the sensor with a d_p of 3 mm is studied for the two different temperatures. It can be concluded that the temperature does not affect the dimensionless calibration curve. Secondly, in figure A.5a it can be seen that the probe distance d_p indeed affects the measurement range. 80% of the saturation signal for a sensor with d_p equal to 3 mm is reached for 2 mm thick film. For a sensor with a d_p equal to 2 mm this saturation level is reached for a 1.5 mm thick film. At the film heights below 0.75 mm the sensor with d_p is 3 mm shows some inconsistencies, which were probably due to the poor alignment of the cylinders during the calibration. This was taken into account for the third development stage.

Figure A.5b shows the saturated signal at different temperatures for the two different sensors. It can be seen that the signal linearly depends on the temperature. The slopes represent the sensitivity to a temperature change for the saturation signal, which can be used for the temperature correction. When finding the film height for a given signal for example, the temperature was used. The temperature was measured close to the sensor in the flow loop. Using this temperature and the linear dependence of the temperature, the saturation signal could be found for the given temperature. Next, the dimensionless response in figure A.5a was used to find the film height for the given voltage.

Sensor validation

The two sensors were used independently in the flow loop shown in figure A.4. Both sensors were exposed twice to a u_{sl} of 10 mm/s and once to a u_{sl} of 30 mm/s.

(a) Dimensionless calibration curves and fits for sensors with d_p is 3 mm and d_p is 2 mm.

(b) Saturation signal at different temperatures for sensors with d_p is 3 mm and d_p is 2 mm.

Figure A.5: The temperature effect in the calibration curves for both probe geometries.
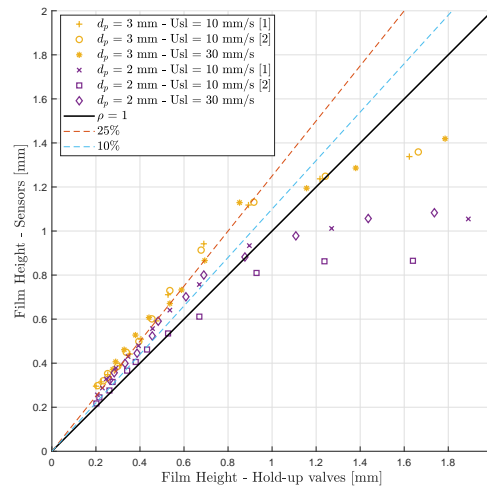

Figure A.6: Film height measured with the sensors against the film height measured with the hold-up valves.

At every superficial liquid velocity, the u_{sg} was varied from 4 m/s in steps of 2 m/s until 34 m/s. The results were compared to the hold-up measurements using the valves in figure A.4.

As can be seen in figure A.6, the film heights below 0.8 mm are measured with an overprediction about 15%. This result was not expected, due to the limited spatial resolution and the slight averaging behaviour of the conductivity probes as explained in section 4.2. The presented results are probably due to the larger diameter of the segment, in which the probes are implemented. Because of this, a sharp transition between the 30 cm segment and the subsequent segment was realised and therefore some accumulation of the liquid film was concluded to be the cause of this result.

For thicker films (>1 mm), the sensors are fully underpredicting the film height compared to the hold-up valves. These film heights were only measured with the hold-up valves in the churn flow

regime. In the churn flow regime, a reasonable amount of the gas can be entrained in the film. This gas presence in the liquid film affects the measurement as the resistance of the liquid will increase. When the two sensors are compared, the sensor with $d_p = 2$ mm is performing slightly better for the smaller film compared to the sensor with $d_p = 3$ mm . On the contrary, the measurement range for the sensors with $d_p = 2$ mm is less than the sensor with $d_p = 3$ mm. This behaviour was expected, see section 4.2. Although the results were interesting, they did not meet the expectation. This was probably due to the geometrical bias and it was therefore decided that a third development stage was necessary.

A.3. Development stage 3

The results of the previous development stage did not meet the expectation. Therefore the third development stage had three improvements:

1. Remove the geometrical bias by implementing the new sensors in a 1 m segment, directly taken from the set-up.

2. Improve the calibration routine by producing new calibration cylinders, which are completely based on the dimensions of the considered pipe segment.

3. The electrical circuit in figure A.4 was replaced by the self-designed PCB which is shown in figure 4.5.

Four different combinations of sensor dimensions were used to further study the dependence of the performance on the probe distance, see table A.1:

Table A.1: Specification of the film sensors implemented in the annulus set-up. Each sensor was implemented 90° from each other.

	Sensor 1	Sensor 2	Sensor 3	Sensor 4
d_p [mm]	1	2	8	28
d_w [mm]	1	2	2	2
R_z [kΩ]	75	75	130	160
C_z [pF]	3.3	3.3	3.3	3.3

All sensors were connected to the new PCB, which has four analog inputs.

The calibration was done using twelve new in-house made calibration cylinders. The results can be seen in figure A.7a. The calibration plot shows that the different sensors have a different measurement range. Furthermore, the linear part of the calibration curves are much smoother compared to the calibration in the previous development stage, see figure A.5a. This is probably due to the new calibration cylinders. However, one aspect draws the attention when this result is compared to the previous development stages. Every calibration curve, except for sensor 4, has a peak. This peak is highly undesirable, since it limits the measurement range. The maximum measurable film height in this case is the height at which the signal is at its maximum. The reason for this response is the fact that all the sensors are connected to the new constructed PCB, while calibrating. Every input on the PCB is connected to the receivers of the sensors, which creates a low potential. When a sensor is calibrated, the signal keeps increasing for increasing film heights, until it 'sees' the receiver of another sensor. This causes that for certain heights the signal is caught by another sensor and therefore loses its strength. This creates a peak. This phenomenon is called cross-talking.
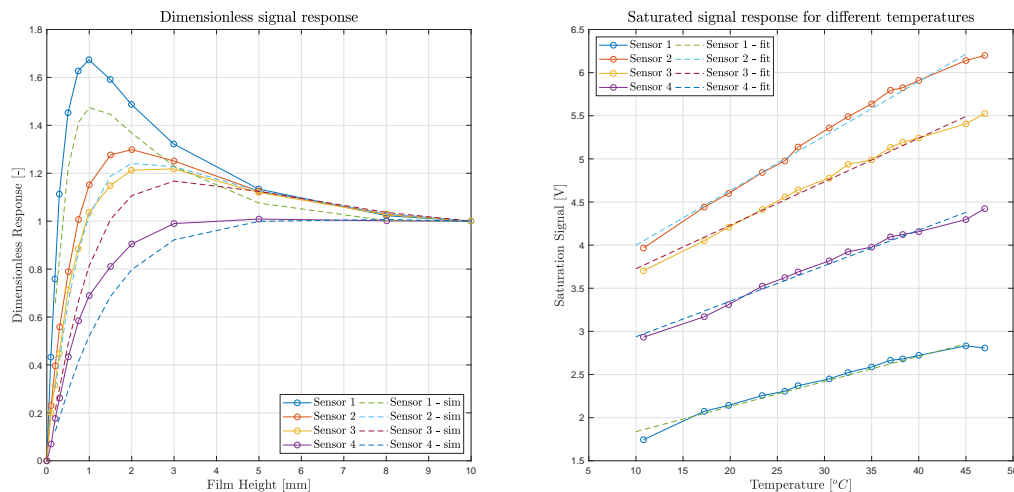
(a) Dimensionless film height response for the 4 sensors. The dashed lines represent the simulation results from COMSOL.

(b) Saturation signal at different temperatures for the the 4 sensors.

Figure A.7: Temperature effect in the calibration curves for the four sensors.

A COMSOL simulation was conducted in order to confirm this response. The simulation domain consisted of the four sensors, and the domains had similar dimensions and boundary conditions as described in section 4.4. The results are shown in figure A.7a and are quite similar to the real response. Furthermore, the sensors are subjected to another calibration routine where the sensors, which are not calibrated, are fully disconnected to the electrical system. These calibration results are shown in figure A.8a and show no peaks. This response in combination with the simulation proves the hypothesis of cross-talking.

These sensors are also subjected to a temperature calibration, see figure A.7b. Again, a linear behaviour can be seen, which can easily be implemented in the conversion of the voltage level. The sensors were implemented in same set-up as described in the previous development stage. The excitation voltage was again a peak-to-peak voltage of 1 V with a frequency of 200 kHz. The sample frequency used for the data acquisition was 5 kHz. The sensors were only subjected to a superficial liquid velocity of 10 mm/s and superficial gas velocities which represent the annular flow regime (>16 m/s). The result for the in-situ test can be found in figure A.8b.

In this figure the results are shown for both the configuration with the single connection, in which only the considered sensor is connected to the electrical circuit, and the configuration for which all sensors are connected to the electrical circuit. Overall, the results are underestimating, which is more in line with the expectation compared to the second development stage. Furthermore, the results are slightly underperforming. As expected, the results for the configuration in which all sensors are connected to the electrical circuit show for smaller films a good approximation of the film thickness. However, for thicker films, the results start to deviate because the cross-talking becomes more dominant. The results for the single connected sensor provide more reliable results. Sensor 1 with the best spatial resolution shows the best results when compared to the hold-up valves. As expected, sensor 4 with the least spatial resolution performs the worst. For sensor 2 and 3 there is a similar behaviour, which is surprising concerning the large difference in probe distance. It was expected that the results of sensor 3 would be less than sensor 2 because of the spatial resolution.
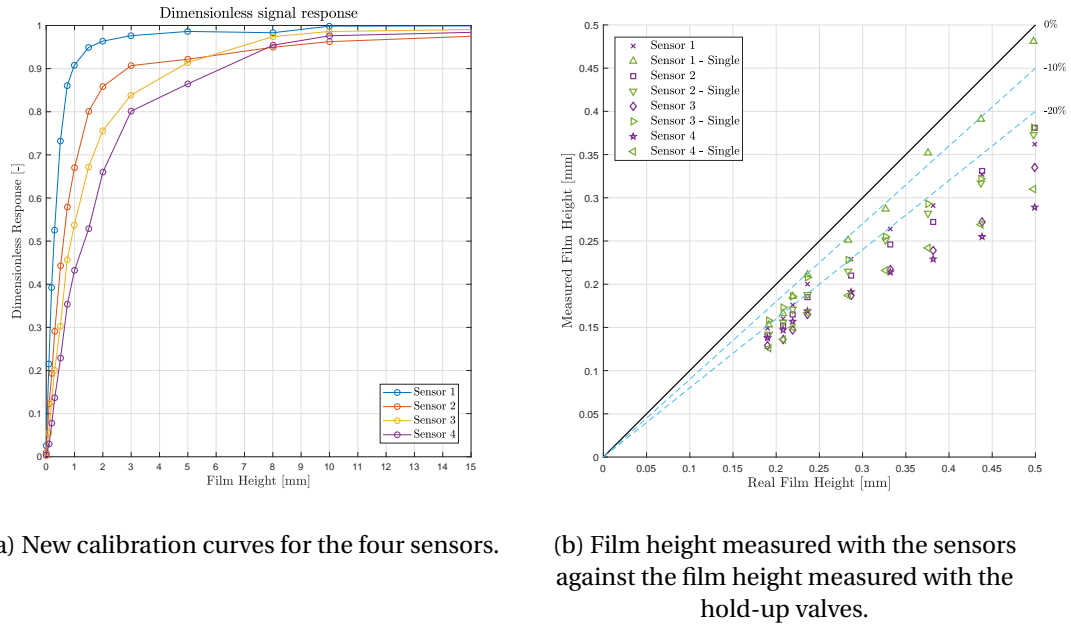
(a) New calibration curves for the four sensors.

(b) Film height measured with the sensors against the film height measured with the hold-up valves.

Figure A.8: The new calibration curves and the results of the in-situ test.

From this development stage it was learnt that cross-talking should definitely be taken into account. Furthermore, it can be seen that the spatial resolution does not have a linear relation with the probe distance.

A.4. Sensor mesh

With the knowledge of the previous development stages an attempt was done to develop a sensor mesh. In section 4.1 a brief background was given on these sensor meshes. The power of this technique is that the amount of wiring can be tremendously reduced and, as a result, more sensors can be implemented, which increases the spacial resolution. Arai et al. [5] implemented this technique in a concentric annulus and this study was taken as foundation for the sensor grid development.

In figure A.9 the sensor orientation of a 4x4 sensor mesh is represented. This sensor mesh is equipped with 4 transmitter lines and 4 receiver lines, resulting in 16 sensors. In case of figure A.9, transmitter line 2 is excited, which means that all the transmitters in this line are excited. The accompanying receivers have a separate receiving line. The next step is to switch off switch 2 and switch on switch 3, to acquire the film height at the next line.

Sensor implementation

It was chosen to implement 12 sensors at two axial positions for both the inner and outer pipe, see figure A.10. A symmetry line was assumed at the eccentricity axis. At one side 9 sensors are implemented for the special resolution. At the other side of the symmetry line three sensors are implemented to validate the assumption of the half-symmetry. Two axial positions are used in order to find the velocity of the disturbance waves, by cross-correlation. The distance between the two axial positions is 35 mm and is based on the study conducted by Sawant et al. [39]. The transmitters are connected in series for each axial position, which means that both axial positions can be excited independently. The receivers at each azimuthal position are connected in series as well, creating 12 receiver lines for each pipe and completing the sensor mesh.
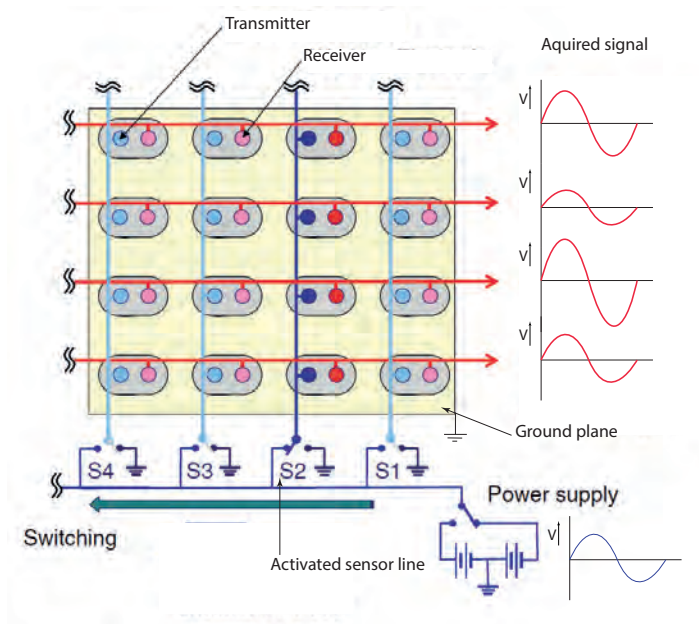
Figure A.9: Sensor mesh top-view with four transmitter lines and four receiver lines. Adapted image from Arai et al. [5].

In the previous section it was discussed how the probe thickness influences the spacial resolution and that there is no linear relation between spacial resolution and probe thickness. Therefore, a probe thickness, d_w, of 2.5 mm and a probe distance, d_p, of 3 mm is chosen. These dimensions are also based on the study conducted by Sawant et al. [39], and they are assumed to be a good trade-off between signal strength and spacial resolution.
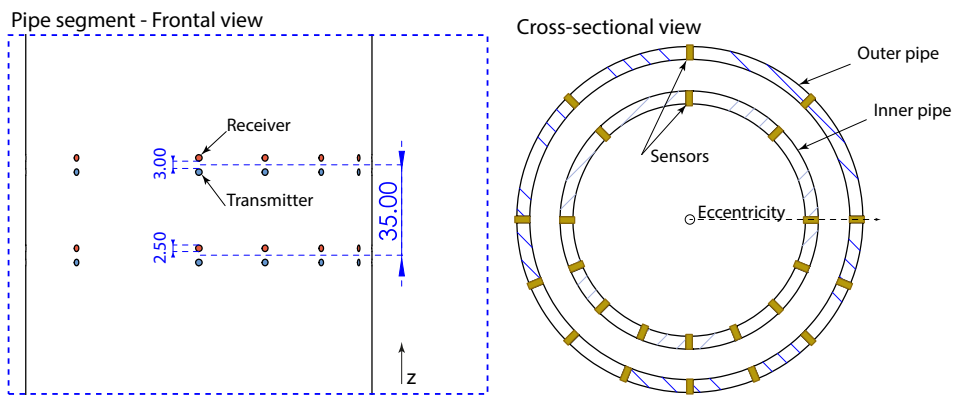
Figure A.10: The sensor implementation for the sensor mesh. Twelve sensors are implemented at two axial positions for inner and outer pipe. The dimensions are in millimeters.

Transmitter switch

To be able to implement the sensor mesh, a signal switching circuit needs to be designed. This switch needs to be capable of switching the input signal, V_{pp}, with the desired speed, between the two transmitter lines for the two axial positions and both pipes.
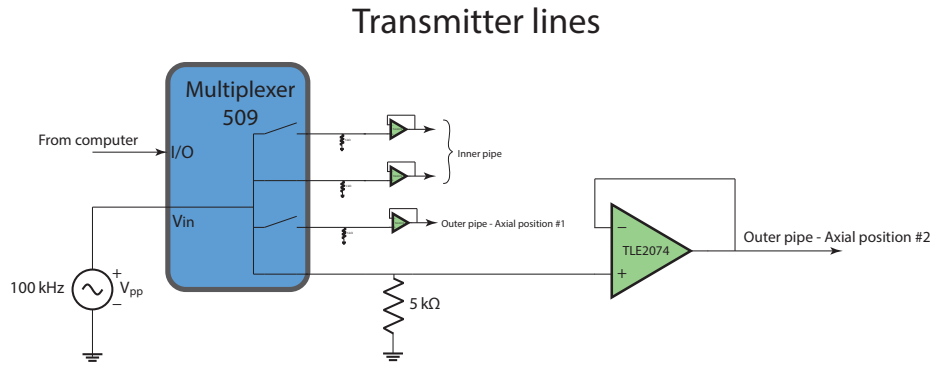
Figure A.11: Switching circuits for the four transmitter lines: two axial positions in two pipes. One line has an exploded view for convenience.

In figure A.11, the switch circuit can be found. A dual-supply mulitplexer, MUX509, is used, which is capable of switching the AC-signal between four channels with a transition time of 92 ns. Usually, there is a small leakage current when a channel is disconnected, which induces a small signal The resistor. The resistor parallel to the ground makes sure that the signal is kept at 0 V when a transistor line is switched off. The operational amplifier serves as a unity follower, which separates the switching circuit from the probes. Using this approach, the probes cannot influence the switching circuit and vice versa. The circuit and its components were tested in the simulation software TINA-TI, and was after approval converted into a PCB, see figure A.12a and A.12b.
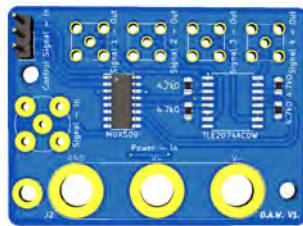
(a) Transmitter PCB design.

(b) Transmitter PCB result.

Figure A.12: Transmitter PCB design and final result.

Cross-talking

From section A.3 it was concluded that cross-talking cannot be neglected. This is also reported in the literature where a sensor mesh is used [5, 7, 15, 30, 36]. The solution is to implement a thin conducting layer between the sensors, which is connected to the ground. This layer 'catches' the signal that is traveling from one sensor to the other. In figure A.9 this is the yellow highlighted area, which is usually called the ground plane. Damsohn and Prasser [15] conducted a thorough study on sensor meshes and concluded that the shape of the ground plane has a large influence on the calibration curve as well as the strength of the returned signal.

Due to the leakage of signal, a peak is still expected in the calibration curve. A manual optimization was conducted using COMSOL in order to find the best ground plane shape. The 'convergence' requirements were the strength of the signal, the height of the peak in the calibration curve and the measurement range. 28 different geometries were studied. In figure A.13 the best result can be seen.

The 2 mm separation of the ground plane, between the two probes has a great influence on the characteristics. When this spacing is decreased, the peak will be lower. However, the area highlighted with the red circle is affected and can show convex shape. This was also reported by Damsohn and Prasser [15]. The 2.25 mm radius around the probes only increases or decreases the signal strength.
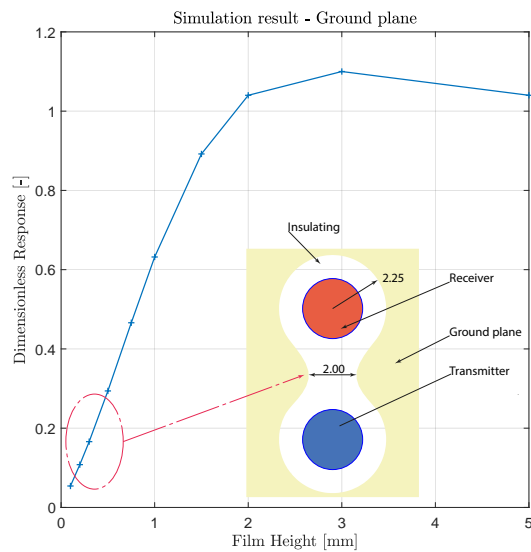

Figure A.13: Best shape of the ground plane with the characteristics. This result was found by comparing 28 different geometries, which were simulated in COMSOL.

Ground plane implementation

The previous sections discussed firstly the importance of a ground plane to prevent cross-talking and secondly the optimal shape for the dimensions of the probes. The ground plane implementation was done using copper deposition via electrolysis, see figure A.14.
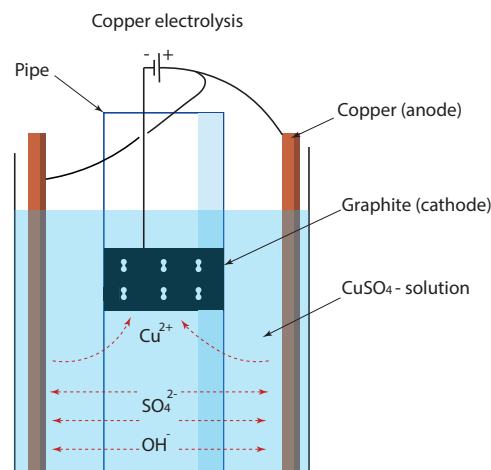
Figure A.14: Graphical representation of the electrolysis with the concerning chemical reaction.

The electrolysis consisted out of three important parts:

1. *The electrolyte.* 10wt% copper(II) sulfate was dissolved in demineralized water.

2. *The anode.* The anode consists out of four copper rods in the far ends of the reactor vessel. These rods are evenly distributed in the circumference of the reactor vessel.

3. *The cathode.* A small layer of graphite served as cathode and was applied on the concerning PMMA pipe. A sticker sheet was laser cut in the shape of the insulting part of the ground plane (see figure A.13) and was applied on the probes in order to prevent deposition of graphite.

A 3 V DC potential was applied between the cathode and anode, which induces the transfer of copper ions in the electrolyte to eventually deposit on the negatively charged graphite. Using the electrolysis process, it was able to deposit a well conducting copper plane of approximately 50 μm thick, see figure A.15 .

Stickers   Inner pipe   Outer pipe   Copper plane
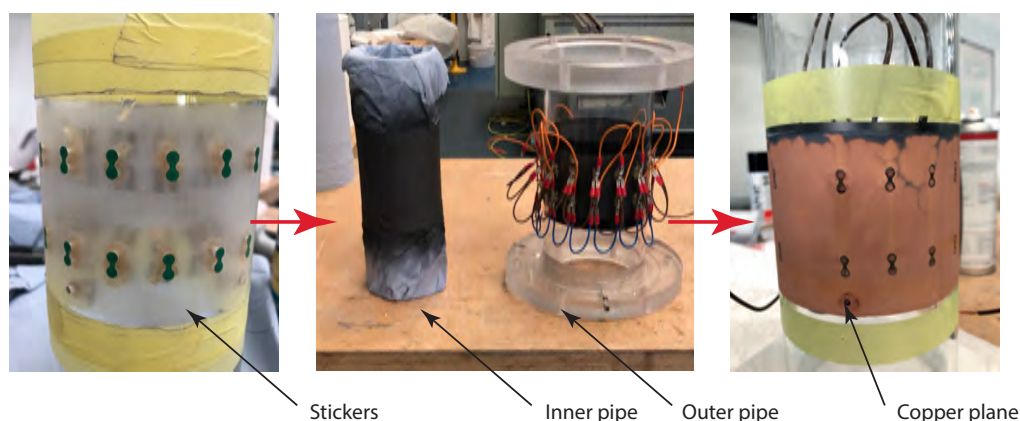
Figure A.15: Copper deposition process of the inner pipe.

Results

After the previous steps, the two pipes were calibrated. Unfortunately, during the calibration process two major deficits showed up. The first inconvenient factor was that 2000 ppm of salt had to be added to the water to get a workable signal out of the sensors. During the real experiments this is undesirable because for every test an accurate solution has to be made. Furthermore, the added salt can deposit on the tubing wall, which can affect the tubing roughness. Secondly, it was observed that there was a large capacitive coupling between the sensors. This can be seen in figure A.16a, where 8 sensors were simultaneously calibrated. During the calibration, one sensor is jammed by putting a non-conducting material in front of the sensor. It can be observed that the jamming is also affecting the signal of the other sensors.

After this observation, a bode-plot was made in order to confirm this hypothesis, see figure A.16b. From the bode plot it was found that for very low frequencies (<20 kHz), the behaviour is dominated by conductance. For higher frequencies capacitance effects become more dominant which proofs the hypothesis. The simulations have shown that this system could work in theory. Unfortunately due to time constraints, a solution for the capacitive coupling could not be implemented in order to make theory reality. A few recommendations on this topic can be found in Chapter 7.
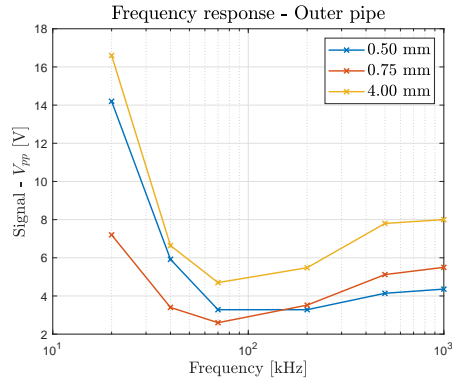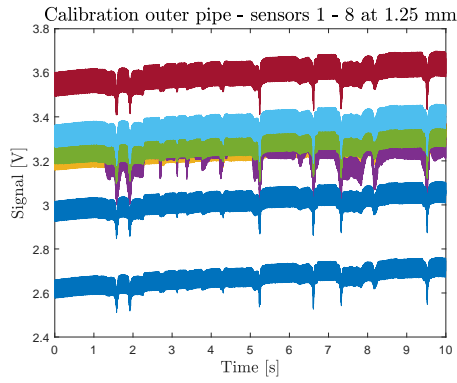
(a) Capacitive coupling between the sensors. (b) Frequency response for different calibration film heights for one sensor in the outer pipe.

Figure A.16: Proof of capacitive coupling.

Eventually, it was chosen to independently excite 5 sensors at one axial position for each pipe, which is similar to the third development stage. The implementation can be found in the Chapter 4.

B

COMSOL simulations

During the cause of this thesis, multiple simulations were conducted in order to determine the characteristics of different sensor geometries. The AC/DC module in COMSOL multiphysics was used to solve the electrical field for the desired domain. In section 4.4, it was discussed that the geometry has three different domains:

- The wall of the tube. The tube of the annulus is made out of PMMA, which is a bad conductor. It is assumed that the bad conductivity properties induce relatively low gradients in this domain. Therefore, the grid size of this domain is chosen to be relatively large compared to the other two domains.

- The probes. The probes are made out of brass, which is a good conductor. Furthermore, the size of the probes is rather small compared to the other domains. Therefore, a dense grid is desired.

- The liquid film. The liquid film has a relatively low conductivity. However the desired grid size in radial direction, need to be very dense, because the liquid film is very thin.

Based on this preliminary study, three different grids are constructed, a coarse, medium and fine grid, in order to find the influence of the grid size on the returned result. For the geometry the outer pipe was used including the ground plane. An impression of the considered geometry can be found in figure 4.9. In table B.1, the specifications of the different grids are summarized.

Table B.1: Grid properties for the sensitivity study.

Domain	Coarse grid			Medium grid			Fine grid		
	No. cells in radial direction	Mesh size [mm] [min max]	No. elements	No. cells in radial direction	Mesh size [mm] [min max]	No. elements	No. cells in radial direction	Mesh size [mm] [min max]	No. elements
PMMA	-	[2.0 9.7]	$16 \cdot 10^3$	-	[1.4 7.7]	$18 \cdot 10^3$	-	[0.5 4.1]	$25 \cdot 10^3$
Probes	-	[0.04 0.3]	$14 \cdot 10^3$	-	[0.04 0.15]	$94 \cdot 10^3$	-	[0.04 0.1]	$322 \cdot 10^3$
Liquid film	10	'swept'	$26 \cdot 10^3$	20	'swept'	$66 \cdot 10^3$	25	'swept'	$122 \cdot 10^3$

The used grids were subjected to a series of simulations for 12 different film heights. In figure B.1, the results for the different grids can be found. It is observed that the results for the linear part of the probe characteristics is comparable for the different grids. However, when the film height is further increased, the coarse grid starts to deviate. It is assumed that the lower number of cells in the radial direction is the cause of this behaviour. When the results for the medium and fine grids are compared for these film heights, it can be seen that the results are very similar. It is assumed that the medium grid is dense enough to find the probe characteristics and is therefore be used in all simulations, covered in this thesis.
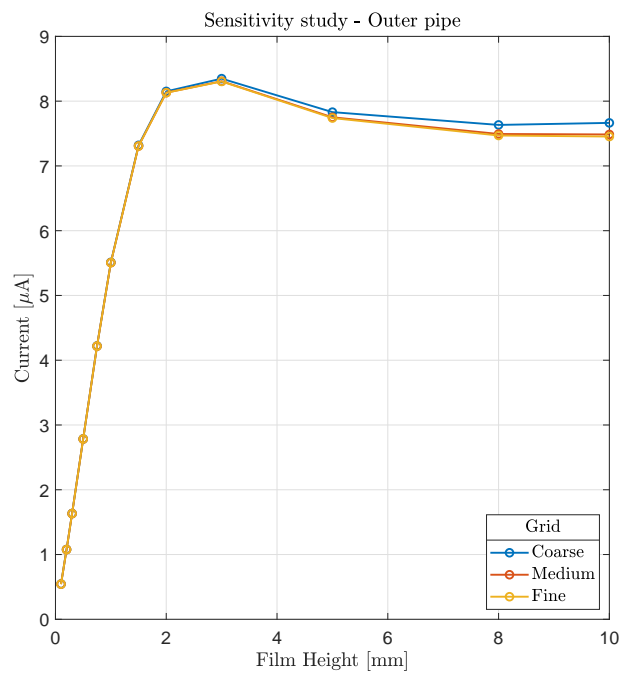
Figure B.1: Sensitivity study of the outer pipe geometry. For the study three different grids were subjected to a simulation sequel consisting of 12 different film heights.
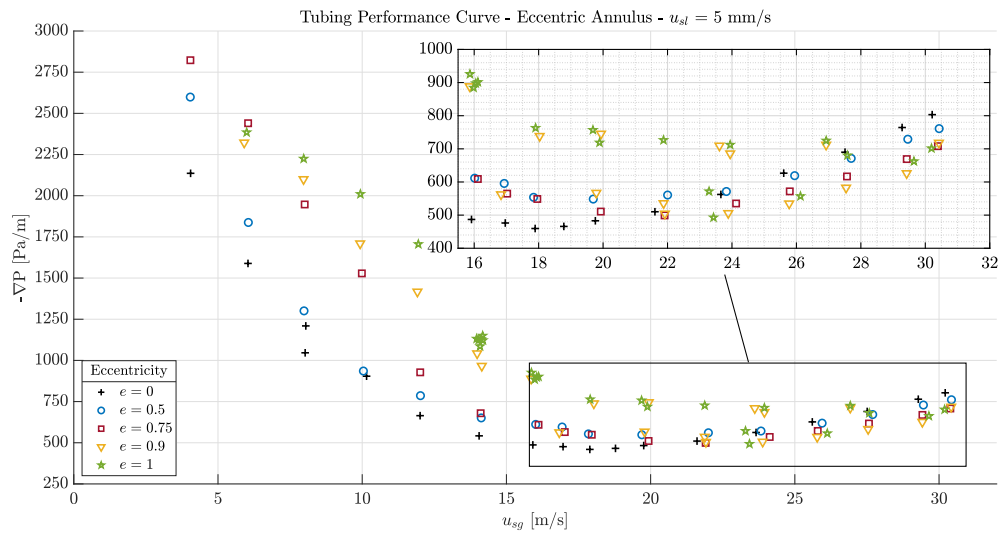
C

Additional data

Figure C.1: Tubing performance curves for different u_{sg}, different eccentricities and a u_{sl} equal to 5 mm/s with equal liquid injection for the inner and outer pipes ($f_{in} = 0.5$).
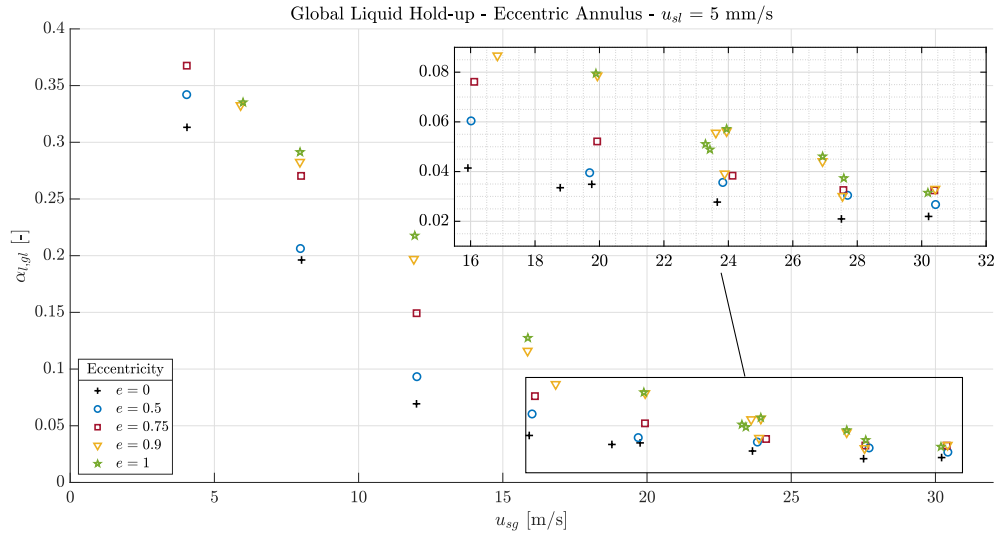
Figure C.2: Liquid hold-up for different u_{sg}, different eccentricities and a u_{sl} equal to 5 mm/s, with equal liquid injection for the inner and outer pipe (f_{in} = 0.5). The global liquid hold-up, $\alpha_{l,gl}$, is represented by the circles and the local liquid hold-up, $\alpha_{l,lo}$, measured using the sensors, is represented by the crosses.
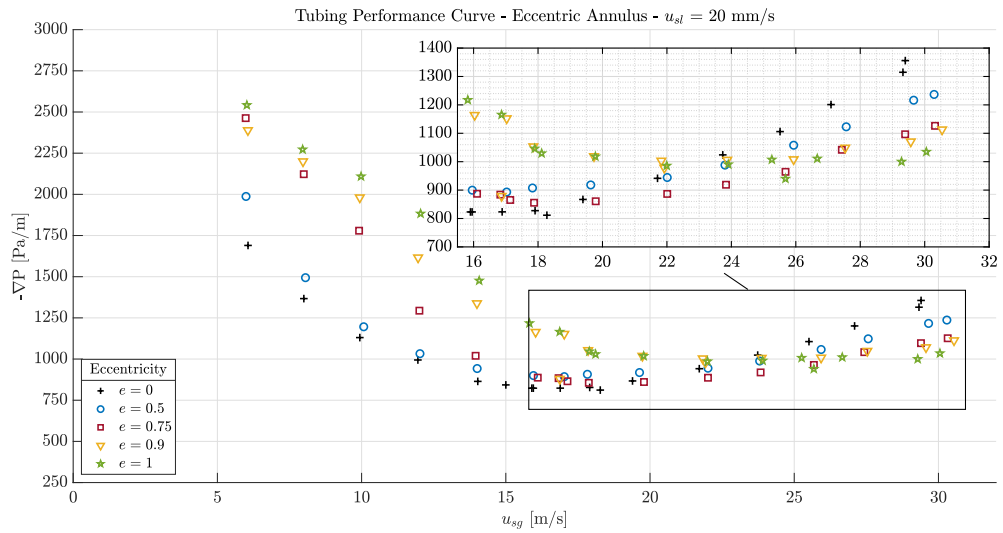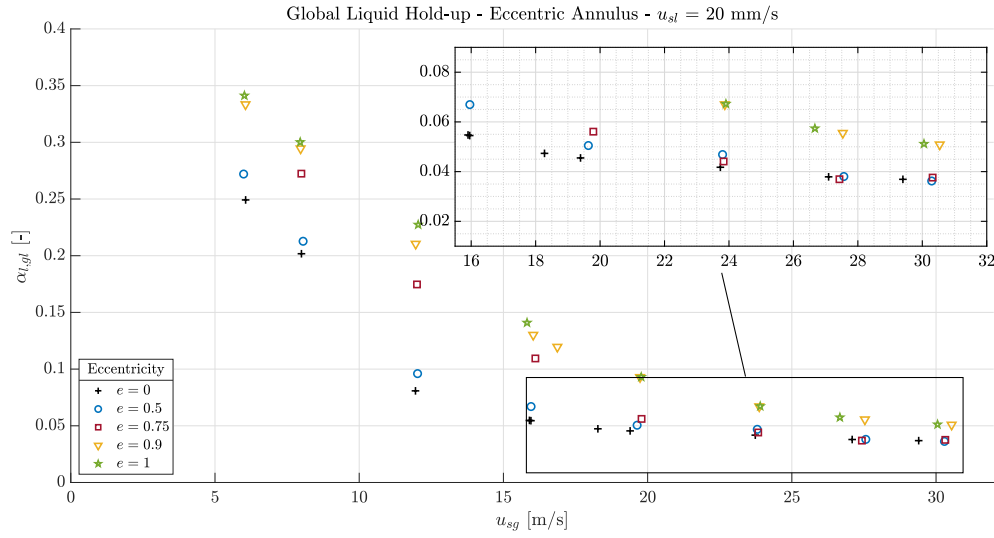

Figure C.3: Tubing performance curves for different u_{sg}, different eccentricities and a u_{sl} equal to 20 mm/s with equal liquid injection for the inner and outer pipes (f_{in} = 0.5).

Figure C.4: Liquid hold-up for different u_{sg}, different eccentricities and a u_{sl} equal to 20 mm/s, with equal liquid injection for the inner and outer pipe ($f_{in} = 0.5$). The global liquid hold-up, $\alpha_{l,gl}$, is represented by the circles and the local liquid hold-up, $\alpha_{l,lo}$, measured using the sensors, is represented by the crosses.

Table C.1: The mean film thickness, corresponding the figure 6.11, for different flow rates and eccentricities.

u_{sl}	e	$u_{sg} = 16$ m/s		$u_{sg} = 22$ m/s		$u_{sg} = 28$ m/s	
		$\overline{\delta_i}$ [μm]	$\overline{\delta_o}$ [μm]	$\overline{\delta_i}$ [μm]	$\overline{\delta_o}$ [μm]	$\overline{\delta_i}$ [μm]	$\overline{\delta_o}$ [μm]
	0	199	175	130	61	113	91
	0.5	240	295	161	182	132	122
5 mm/s	0.75	279	320	159	180	117	141
	0.9	299	431	215	194	179	235
	1	255	315	163	175	133	134
	0	214	260	192	168	155	133
	0.5	256	342	192	229	166	161
10 mm/s	0.75	310	347	187	226	156	168
	0.9	417	592	251	299	196	196
	1	406	555	194	218	161	208
	0	236	326	212	232	175	180
	0.5	295	407	225	291	193	223
20 mm/s	0.75	373	432	230	279	190	210
	0.9	443	655	299	373	253	296
	1	422	586	241	299	189	218

D

Set-up impressions

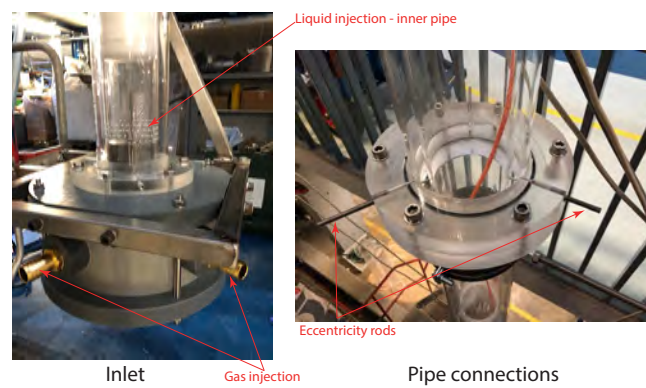This Appendix shows some additional photographs of the set-up and the electrical circuit used.

Figure D.1: Final result of the inlet (left) and the pipe connections (right).

Figure D.2: Left, a top view picture where the set-up is under construction. Right, a side view of the complete set-up.
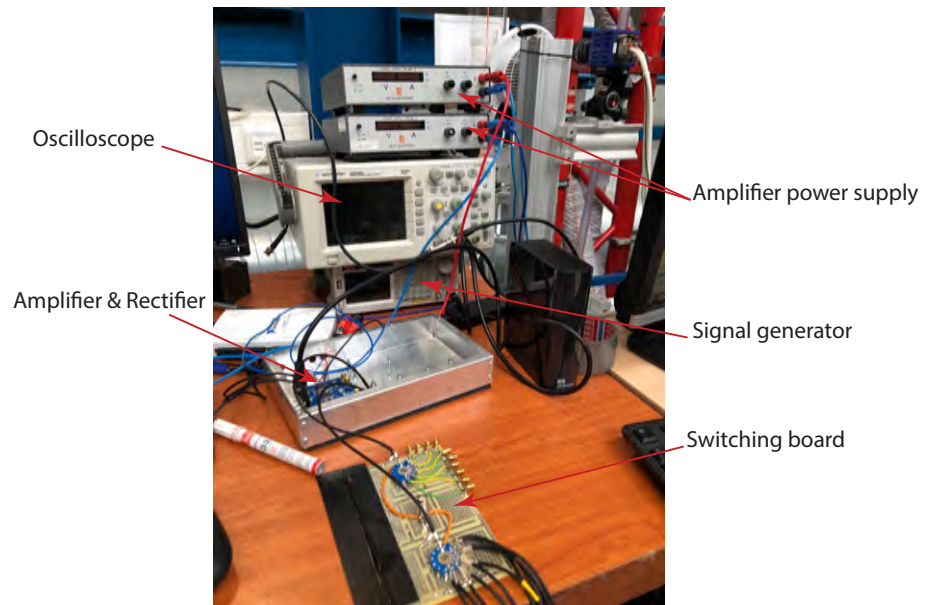
Figure D.3: Circuit used for the signal generation and processing for the used film height sensors.